




Crossmark

PAPER

RECEIVED  
dd Month yyyy  
REVISED  
dd Month yyyy

# Impact of the equation of state on core collapse supernovae I: the low- $T/|W|$ instability

Marco Cusinato<sup>1</sup>, Martin Obergaulinger<sup>1,2</sup> and Miguel Ángel Aloy<sup>1,2</sup><sup>1</sup>Departament d'Astronomia i Astrofísica, Universitat de València, Av. Vincent Andrés Estellés, 19, 46100 Burjassot, Spain<sup>2</sup>Observatori Astronòmic, Universitat de València, 46980 Paterna, Spain**E-mail:** marco.cusinato@uv.es, miguel.a.aloy@uv.es**Keywords:** Supernovae — Gravitational waves — MHD — Instabilities — EOS

## Abstract

Rapidly rotating core-collapse supernovae are promising sources of multimessenger emission, as non-axisymmetric dynamics in the newly formed proto-neutron star can leave characteristic imprints on both gravitational waves and neutrinos. We present three-dimensional neutrino-magnetohydrodynamics simulations of the collapse of a rapidly rotating  $35 M_{\odot}$  progenitor, performed with five different finite-temperature nuclear equations of state, to investigate how dense-matter physics affects the development of the low- $T/|W|$  instability and its associated multimessenger signatures.

We find that the low- $T/|W|$  instability develops in all equation of state models considered, indicating that its occurrence is robust for this rapidly rotating progenitor. However, its onset time, dominant azimuthal structure, lifetime, and characteristic multimessenger frequencies vary among models, reflecting differences in the evolving proto-neutron star structure and rotation profile. The instability produces large-scale spiral modes that generate quasi-periodic gravitational wave emission and modulate the neutrino luminosities, especially along directions close to the equatorial plane.

The dominant gravitational wave frequency associated with the instability correlates with the effective stiffness and compactness of the proto-neutron star: models with more compact/stiffer configurations emit at higher frequencies. This suggests that, in rapidly rotating core-collapse supernovae, the frequency of the low- $T/|W|$  instability-driven gravitational wave signal may provide a diagnostic of the dense-matter equation of state, complementary to the information carried by the neutrino signal.

## 1 Introduction

Core collapse supernovae (CCSNe) are among the most promising targets of multimessenger astrophysics. Gravitational waves (GWs) and neutrinos, emitted from deep within the collapsing core, provide direct insight into the earliest phases of the dynamics and energetics of the system [1, 2, 3, 4, 5]. In contrast, electromagnetic observations, originating at later times from the outer layers of the star, offer complementary constraints on the progenitor and on the properties of the ejecta [6, 7, 8]. Likewise, the observation of supernova remnants offers the possibility of probing the circumstellar medium and nucleosynthesis products [9], and can probably be connected to the progenitor type and explosion mechanism [10]. The GWs from Galactic events are expected to lie within the sensitivity of current ground-based detectors, such as Advanced Laser Interferometer Gravitational Wave Observatory (LIGO) [11], Virgo [12], and Kamioka Gravitational Wave Detector (KAGRA) [13], while extragalactic explosions may become observable with future facilities, including Cosmic Explorer (CE) [14] and Einstein Telescope (ET) [15]. Large underground neutrino experiments, such as Super-Kamiokande (SK) [16], Hyper-Kamiokande (HK) [17], Jiangmen Underground Neutrino Observatory (JUNO) [18], Deep Underground Neutrino Experiment (DUNE) [19], IceCube [20, 21], and KM3NeT [22], are expected not only to replicate the historic detection of the 25 neutrinos from SN 1987A [23, 24, 25], but to record thousands of events for a typical galactic CCSN, with detectable signals also possible from supernovae in nearby satellite galaxies [26].

Massive stars ( $M_{\text{ZAMS}} \gtrsim 8 M_{\odot}$ ) undergo nuclear fusion of progressively heavier elements, until they form an iron core primarily supported by the pressure of relativistic degenerate electrons. When

the core surpasses the Chandrasekhar mass, it collapses to a proto-neutron star (PNS) [27, 28, 29, 30]. The sudden stiffening of the equation of state (EOS) launches a shock-wave that initially stalls due to photodissociation of iron-group nuclei. The majority of successful explosions are thought to be powered by the hydrodynamically aided neutrino-driven mechanism [31, 32, 33], in which a combination of energy deposition by neutrinos behind the stalled shock and hydrodynamic instabilities such as convection and the standing accretion shock instability (SASI) revives the shock and powers the explosion. In more extreme cases, particularly in rapidly rotating and magnetized progenitors, the explosion may instead be powered by magnetorotational processes [34, 35, 36, 37]. Conversely, if the shock fails to revive, the PNS may collapse into a black hole (BH) [38, 39, 40, 29, 41]. In the last decade, these scenarios have been investigated by two-dimensional (2D) and three-dimensional (3D) simulations [35, 42, 43, 44].

Crucial to the evolution of the CCSN is the EOS of matter at supranuclear densities, which impacts the PNS contraction, its thermal and compositional evolution, and the associated neutrino emission. The stiffness of the EOS determines the radius, compactness, and maximum mass of the PNS, thus influencing the likelihood of BH formation and the timescale over which it may occur [45, 46, 47]. In recent years, several studies have investigated the impact of the EOS on the explodability of the massive stars [33, 48, 49] and on the GW emission using both 2D and 3D [50, 3, 4, 51, 5]. Such studies are motivated by and necessary due to the considerable theoretical and experimental uncertainties in the properties of matter at supranuclear densities. Experiments in terrestrial laboratories typically probe conditions that differ from those in CCSN cores, and the complexity of the strong interaction makes theoretical calculations difficult. Hence, a large number of models for the nuclear EOS have been proposed. Many of them are routinely used in numerical simulations of compact astrophysical objects and stellar explosions. The fact that the results of these models significantly depend on the chosen EOS allows us to use them for putting additional constraints on the partly unknown parameters of nuclear-matter physics.

The GWs emitted by CCSNe are inherently stochastic, reflecting the wide range of physical mechanisms that contribute to their generation. In the early post-bounce phase, prompt convection excites oscillations with characteristic frequencies of a few hundred Hertz [50, 52, 53, 54, 55, 45], while convection within the PNS excites  $g$ -modes that can reach frequencies of order  $\gtrsim 1$  kHz [56, 57]. On longer timescales, post-shock convection [58] and SASI [59, 60, 61, 2, 62, 63, 64] can develop, producing lower-frequency emission around  $\sim 100$  Hz. Rotation further modifies the GW signal: moderate rotation can enhance the excitation of the PNS  $f$ -mode [65], while rapidly rotating cores may develop non-axisymmetric instabilities.

In particular, differentially rotating PNSs can become unstable to the low- $T/|W|$  instability (LTWI), a shear-driven non-axisymmetric instability associated with the presence of strong differential rotation and an internal corotation point at which the frequency of one of the characteristic oscillation modes of the PNS matches the local angular frequency of rotation [66, 67, 68, 69, 70, 71, 72]. Unlike the classical dynamical bar-mode instability, which requires a ratio between rotational and gravitational energy of  $T/|W| \gtrsim 0.27$ , the LTWI can develop at substantially lower rotational energies, with typical thresholds of  $T/|W| \sim 0.04$ – $0.06$ , which can be reached in rapidly rotating CCSNe. Strong differential rotation can lower this threshold even further [73, 69, 74, 75, 72]. The instability leads to the growth of low-order spiral modes ( $m = 1, 2$ ), generating long-lasting narrow-band GW emission whose frequency is set by the rotational dynamics of the PNS. Because the development of the LTWI depends sensitively on the rotational profile, compactness, and internal structure of the PNS, it is expected to be influenced by the nuclear EOS through its influence on the contraction and differential rotation of the remnant.

In this study, we aim to characterise the impact of the nuclear EOS on the multimessenger emission from CCSNe, focusing on the GW and neutrino signals produced during the shock-stall phase in rapidly rotating cores. We carry out a series of 3D neutrino-magnetohydrodynamics simulations of the core collapse of a single, rapidly rotating progenitor star with a zero-age main-sequence mass of  $35 M_{\odot}$ . Several previous studies of CCSN have used the same stellar model as a progenitor [e.g., 40, 36, 72], studying how variations of the magnetic field in the core at the moment of collapse affect the dynamics, the compact remnant, and the multimessenger signal. Among these previous works, we highlight the purely hydrodynamic model presented by [72] in which the LTWI led to the development of spiral modes and left an imprint in the GW and neutrino emission. The present study is an extension of that one and analyses the results of five models of the same star with different nuclear EOSs. We explore systematic differences in the dynamics, GW signal, and neutrino emission between EOSs differing in terms of the underlying input physics (Skyrme and relativistic mean field (RMF)-type approaches) and parameters such as their stiffness at supranuclear densities.

The remainder of this paper is organized as follows. Section 2 outlines the numerical methods,

progenitor model, and nuclear EOSs employed in our CCSN simulations. In Section 3, we present the main results of our study. Section 4 discusses the implications of the EOS for multimessenger detectability, and in Section 5 we summarise our conclusions.

## 2 Methods

### 2.1 Numerical setup and progenitor model

The 3D CCSN simulations presented in this work were performed with the **Aenus-ALCAR** code [76, 77, 78, 79, 36, 80]. This code solves the equations of special-relativistic magnetohydrodynamics coupled to a spectral two-moment neutrino transport scheme. Specifically, it evolves the zeroth (energy density) and first (momentum density) moments of the Boltzmann equation, closed by the maximum-entropy Eddington factor [81], for electron neutrinos,  $\nu_e$ , electron antineutrinos,  $\bar{\nu}_e$ , and heavy-lepton neutrinos,  $\nu_x = (\nu_\mu, \bar{\nu}_\mu, \nu_\tau, \bar{\nu}_\tau)$ .

The set of neutrino–matter interactions includes: emission and absorption of electron neutrinos by protons and neutrons; nucleonic absorption, emission, and scattering with weak-magnetism and recoil corrections; emission and absorption of electron neutrinos by heavy nuclei; coherent elastic scattering of all neutrino species off heavy nuclei; inelastic scattering of neutrinos off electrons and positrons; pair processes (electron–positron annihilation); and nucleonic bremsstrahlung. The contribution of gravity is included in the neutrino transport equations following the  $\mathcal{O}(v/c)$ -plus formulation of [82]. The nuclear composition is assumed to follow nuclear statistical equilibrium (NSE) at high densities and temperatures, while at lower densities the transition to non-NSE regimes is handled using the flashing scheme of [83].

All simulations follow the evolution of a stellar model 350C, a Wolf–Rayet star with a zero-age main-sequence mass of  $M_{\text{ZAMS}} = 35 M_\odot$  and subsolar metallicity ( $Z = 0.1 Z_\odot$ ). This stellar model was originally evolved by [84] as a prototype collapsar progenitor. However, subsequent studies (e.g., [39, 40]) have shown that, in the context of CCSNe, this model does not lead to prompt BH formation, and if BH forms at all, it does so only on timescales longer than  $\mathcal{O}(1 \text{ s})$ . Moreover, a purely hydrodynamical simulation of this progenitor was shown to develop the LTWI after core collapse [72]. Owing to its rapidly rotating core and its known tendency to sustain non-axisymmetric activity after bounce, 350C provides a suitable setup for studying the influence of the EOS on the development of the LTWI.

The simulations are evolved with the original rotation profile, but the progenitor magnetic field is replaced at the pre-supernova stage by a weak dipolar field. Modifying the magnetic field predicted by the stellar-evolution model is not fully self-consistent with the progenitor evolution. However, the magnetic fields in pre-supernova models are inferred from local hydrostatic properties rather than obtained from self-consistent MHD stellar-evolution calculations, and are typically available only in radiative stellar layers [85, 80, 86]. The latter point is particularly important here, because it makes the magnetic-field structure provided by the pre-collapse stellar model spatially incomplete and lacking a physically well-defined global topology.

For this reason, replacing the original magnetic-field profile by an analytically prescribed field is a physically motivated choice: it provides a regular magnetic configuration satisfying the solenoidal constraint, while also allowing us to reduce the initial field strength (see below). The field geometry is defined by the vector potential  $\mathbf{A}$  [87]:

$$(A^r, A^\theta, A^\phi) = \frac{R_0^3 r}{2(r^3 + R_0^3)} (B_{\text{tor}} \cos \theta, 0, B_{\text{pol}} \sin \theta), \quad (1)$$

where  $B_{\text{tor}} = B_{\text{pol}} = 10^6 \text{ G}$  are the initial toroidal and poloidal magnetic field components, and  $R_0 = 10^8 \text{ cm}$  is the characteristic length scale. The magnetic field strength of the pre-supernova progenitor is deliberately reduced because [88] found no significant evidence for the development of the LTWI in model 350C when using its original magnetic-field configuration, whereas [72] did find the instability in the same progenitor assuming a vanishing magnetic field. While a strictly null magnetic field would suppress magnetic effects during the post-bounce evolution, adopting a weak seed field allows them to develop without making them dynamically important during the first 250 ms of evolution.

The simulations are performed in axisymmetry until 5 ms before core bounce, after which they are mapped onto 3D grids. The spherical grid consists of  $n_\theta = 64$  zones in the  $\theta$ -direction and  $n_\phi = 128$  zones in the  $\phi$ -direction, covering the full solid angle with an angular resolution of  $2.8^\circ$  along each angular direction. In the radial direction the grid extends to  $4 \times 10^{10} \text{ cm}$ , and consists of two parts: a uniform grid from the centre to 16 km with a resolution of  $5 \times 10^4 \text{ cm}$ , and a logarithmically stretched one from 16 km to the end of the domain. Except for model LS, which uses  $n_r = 240$  zones, all models employ  $n_r = 320$  radial zones. However, this choice of  $n_r$  for model LS is not expected to have a

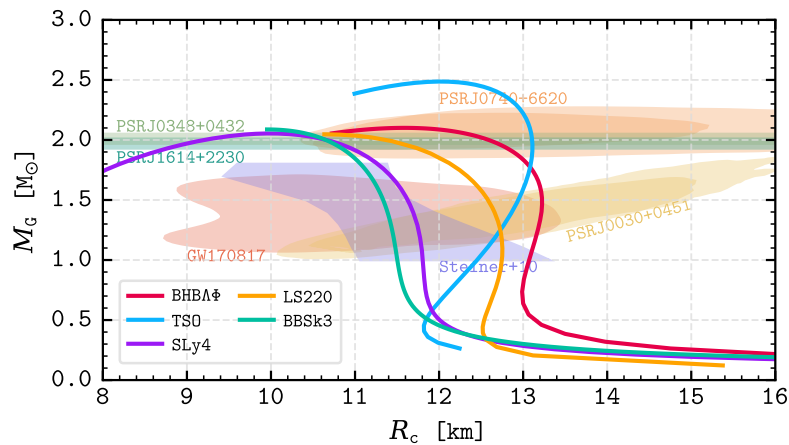


Figure 1. Gravitational mass-radius relations for cold, static, spherically symmetric, and non-rotating neutron stars (NSs) taken from CompOSE [89, 90] using the EOSs used in this work. The shaded regions represent astrophysical constraints at the 95% confidence level. The yellow and orange regions display constraints from NICER observations [91, 92, 93, 94]; the red region corresponds to the detection of the GW170817 event [95]; the purple region shows constraints from X-ray observations [96]; and the green regions indicate the maximum observed NS masses [97, 98].

significant impact on the results. The uniformly spaced inner part of the radial grid, where the PNS forms and evolves, is essentially the same as in the other models. The differences are confined mainly to the logarithmically stretched outer region of the domain, at radii that are not affected by the dynamics over the simulated time span.

The energy domain is discretized into  $n_\epsilon = 10$  bins extending from  $\epsilon_{\min} = 0$  MeV to  $\epsilon_{\max} = 240$  MeV. The bin widths increase approximately logarithmically with energy, so that the low-energy bins are narrower and the high-energy bins progressively broader.

## 2.2 Equation of state selection

The simulations employ two distinct EOSs: one for high (nuclear) densities and one for low densities. The high-density EOS is applied in regions with  $\rho > 10^6$  g/cm<sup>-3</sup> or where the temperature exceeds  $T > 0.5$  MeV.

The low-density EOS (H.-Th. Janka, private communication) assumes nonrelativistic, nondegenerate nucleons and nuclei; arbitrarily relativistic and arbitrarily degenerate electrons and positrons; and a thermal photon bath, with Coulomb-lattice corrections.

To describe matter at high densities, we employ five finite-temperature, composition-dependent EOSs: LS220 [99], SLy4 [100], BHBA $\phi$  [101], BBSk3 [102], and TSO [103]. The corresponding mass-radius relations for cold neutron stars in spherical symmetry are shown in Figure 1.

All these EOSs are broadly consistent with current astrophysical constraints, including those derived from NICER observations [91, 93, 92, 94] and GW detections [104, 105]. They can support NSs more massive than the heaviest observed so far [97, 98], and they agree with the constraints inferred from type-I X-ray bursters exhibiting photospheric radius expansion, as well as transient low-mass X-ray binaries [96]. Although LS220 does not satisfy all nuclear experimental constraints [106], it is retained here to facilitate comparison with previous studies [71, 70, 72].

Each EOS accounts for protons, neutrons, electrons, positrons, photons, and  $\alpha$  particles, as well as light nuclei (deuterium, tritium, and helium) and heavy nuclei in NSE. The BHBA $\phi$  model further includes  $\Lambda$  hyperons interacting through the  $\phi$  meson.

The LS220 and SLy4 EOSs are based on a nonrelativistic liquid-drop model with a Skyrme-type interaction. In particular, the LS220 model adopts a nuclear incompressibility modulus of  $K = 220$  MeV, which yields neutron star properties consistent with observational constraints.

The BHBA $\phi$  EOS adopts a RMF framework, where the field equations are solved in the Hartree approximation. Additionally, at high densities it includes the full baryon octet—particularly  $\Lambda$  hyperon—together with repulsive hyperon–hyperon interactions mediated by the  $\phi$  meson.

The BBSk3 EOS employs Brussels extended Skyrme interactions and was constructed within a Bayesian investigation of the dense-matter EOS to ensure consistency with modern astrophysical constraints and with chiral effective field theory calculations of pure neutron matter.

Finally, the TSO EOS follows the covariant density functional approach, including hypernuclear

EOS	$J$ [MeV]	$L_{\text{sym}}$ [MeV]	$Q_{\text{sat}}$ [MeV]	$m^*/m$	$B_1$	$B_2$ [MeV $^{-1}$ ]	$M_{\text{max}}^{\text{grav}}$ [ $M_{\odot}$ ]	$M_{\text{max}}^{\text{bar}}$ [ $M_{\odot}$ ]	$\rho_0$ [ $10^{14}$ g/cm $^3$ ]
SLy4	32.0	46.0	-365	0.70	0.994	0.0311	2.05	$\sim 2.33$	2.66
BHBA $\phi$	31.9	55.0	+169	0.56	1.031	0.0323	2.10	$\sim 2.40$	2.50
BBSk3	29.6	39.6	-453	0.461	1.621	0.0548	2.08	$\sim 2.38$	2.48
TSO	32.0	30.0	-400	0.57	1.871	0.0585	2.47	$\sim 2.80$	2.50
LS220	29.3	74.0	-411	1.000	0.396	0.0135	2.05	$\sim 2.38$	2.60

Table 1. Cold EOS indicators. Columns from left to right: EOS name; symmetry energy at saturation density ( $J$ ); slope of the symmetry energy at saturation density ( $L_{\text{sym}}$ ); skewness parameter ( $Q_{\text{sat}}$ ), taken or derived as follows: SLy4 from an explicit calculation using the Skyrme parameters of [107] and formulae from [108]; BBSk3 from [109]; LS220 from [90] (Table IV; note that the quantity listed there corresponds to  $Q_{\text{sat}}$  in our convention); BHBA $\phi$  is mapped to the DD2 interaction in [90]; TSO from [103], adopting the sign convention consistent with the standard definition of  $Q_{\text{sat}}$ ; effective nucleon mass; heuristic EOS parameters based on the symmetry-energy parameters, nucleon effective mass, and skewness parameter,  $B_1$  Equation 2 and  $B_2$  Equation 3; maximum gravitational mass ( $M_{\text{max}}^{\text{grav}}$ ), taken from the literature: SLy4 from [110, 90], LS220 from [111, 90], BHBA $\phi$  from [112], BBSk3 from [109], and TSO from [103]; maximum baryonic mass ( $M_{\text{max}}^{\text{bar}}$ ), estimated from typical Tolman-Oppenheimer-Volkoff (TOV) solutions assuming  $M^{\text{bar}} - M^{\text{grav}} \simeq 0.15\text{--}0.30 M_{\odot}$ , depending on the EOS stiffness; nuclear saturation density ( $\rho_0$ ).

degrees of freedom, with baryonic coupling constants tuned such that the symmetry energy slope and skewness parameters are  $L_{\text{sym}} = 30$  MeV and  $Q_{\text{sat}} = 400$  MeV, respectively.

In Table 1, we summarise a set of nuclear-matter and NS properties that provide insight into the behaviour of the different EOSs employed in this work. The parameters  $J$  and  $L_{\text{sym}}$  characterise the magnitude and density dependence of the nuclear symmetry energy at saturation, while  $Q_{\text{sat}}$  encodes the skewness of symmetric nuclear matter and thus constrains the high-density behaviour of the pressure. The effective nucleon mass  $m^*/m$  influences both the thermal properties of the EOS and the neutrino-matter interaction rates. In addition, we report the maximum gravitational and baryonic masses of cold neutron stars, which provide integral constraints on the overall stiffness of the EOS.

For later use, we introduce the combinations

$$B_1 = \frac{1}{m^*/m} \frac{J}{L_{\text{sym}}}, \quad (2)$$

$$B_2 = \frac{1}{m^*/m} \frac{1}{L_{\text{sym}}}, \quad (3)$$

These quantities are heuristic proxies rather than fundamental EOS parameters. They are designed to combine, in a compact way, the overall scale of the symmetry energy ( $J$ ), its density dependence ( $L_{\text{sym}}$ ), and the effective mass, which influences the thermal response and neutrino-matter interactions. Their role in this chapter is therefore purely comparative: they provide a convenient way to rank the adopted EOSs and to test whether broad trends in the simulations correlate with simple combinations of cold nuclear-matter properties. Any such correlation should, however, be interpreted as suggestive only, since the effective stiffness of the PNS during the evolution depends on the full hot and composition-dependent EOS.

During the CCSN evolution, the PNS continuously accretes mass and contracts, probing a wide range of densities and thermodynamic conditions. As a consequence, its effective stiffness is not a fixed property but evolves in time and cannot be uniquely characterised by nuclear-matter parameters defined at saturation density alone. To capture this behaviour, we adopt the tidal Love number  $\kappa_2$  as an effective diagnostic of the PNS stiffness, computed as in Hinderer, Lackey, Lang, and Read [113]. However, we stress that the procedure to compute  $\kappa_2$  formally applies to cold, static, and spherically symmetric neutron stars in hydrostatic equilibrium. In the CCSN context, the PNS is instead hot, accreting, and rotating. Therefore, the resulting  $\kappa_2$  should be regarded as an effective indicator of the PNS stiffness. In practice, we evaluate it using spherically averaged profiles, which allows us to track relative differences among EOSs during the evolution. Despite these limitations,  $\kappa_2$  provides a useful proxy for comparing the compressibility of the PNS across different models. Therefore, when we compare two EOSs we refer to one as *stiffer* (*softer*) than the other if the value of  $\kappa_2$  is smaller (larger). Here we use  $\kappa_2$  only as an effective structural proxy for comparing our hot, evolving PNS models. This usage should not be confused with the standard cold-NS literature, where EOS stiffness is more commonly discussed in terms of radius or tidal deformability  $\Lambda = \frac{2}{3}\kappa_2 C^{-5}$  at fixed mass (where  $C = GM^{\text{grav}}/(Rc^2)$  denotes the compactness of the star, with  $G$  and  $c$  the gravitational

constant and the speed of light in vacuum, respectively), rather than through a monotonic ranking of  $\kappa_2$  alone.

### 2.3 Gravitational wave extraction

The GWs signal is extracted with the standard quadrupole formula [114, 115],

$$h_{ij}(t, \mathcal{D}) = \frac{2G}{c^4 \mathcal{D}} \ddot{Q}_{ij}(t - \mathcal{D}/c), \quad (4)$$

where  $\mathcal{D}$  is the distance to the source,  $t$  is the time and  $Q_{ij}$  are the mass quadrupole moments. In spherical coordinates, the mass quadrupole moments are given by

$$Q_{lm} = \int \rho(r, \theta, \phi, t) r^2 Y_{lm}^*(\theta, \phi) dV, \quad (5)$$

where  $Y_{lm}^*$  are the spherical harmonics and  $\rho$  the density. By applying the continuity equation and performing a partial integration, the first time derivative of the quadrupole moment can be rewritten in terms of spatial derivatives. Rather than computing the contribution from the entire volume occupied by the emitting source, we first consider the contribution from a spherical shell bounded by an inner radius  $r_1$  and an outer radius  $r_2$ . The contribution from the whole source is then recovered straightforwardly by taking the limits  $r_1 \rightarrow r_{\min}$  and  $r_2 \rightarrow r_{\max}$ , where  $r_{\min}$  and  $r_{\max}$  denote the innermost and outermost radial boundaries of the source, respectively.

Applying the continuity equation and performing a partial integration, the first time derivative of the quadrupole moment associated with this shell can be written as

$$\dot{Q}_{lm} \Big|_{r_1}^{r_2} = \int_{r_1}^{r_2} dr r^2 \int d\Omega \rho \mathbf{v} \cdot \nabla (r^2 Y_{lm}^*(\theta, \phi)) - \left[ \int d\Omega \rho v_r r^4 Y_{lm}^*(\theta, \phi) \right]_{r_1}^{r_2}, \quad (6)$$

where  $\mathbf{v}$  is the fluid velocity,  $v_r$  its radial component, and

$$[F(r)]_{r_1}^{r_2} \equiv F(r_2) - F(r_1).$$

The first term in Equation (6) is the volume contribution, while the second term is the surface contribution arising from the radial boundaries of the shell.

This surface term is often irrelevant when the quadrupole moment is evaluated over the full computational domain and the boundary contribution vanishes. However, Zha [116] showed that—in 2D simulations—when decomposing the GW signal into contributions from subdomains of the simulation volume, neglecting this term leads to an incorrect spatial attribution of the emission. It must therefore be retained in the shell decomposition used here.

Finally, following Raynaud, Cerdá-Durán, and Guilet [117] the GW strain generated by a subdomain of the star can be expressed as

$$h(t, \mathcal{D}) \Big|_{r_1}^{r_2} = h_+ - ih_\times = \frac{1}{\mathcal{D}} \frac{G}{c^2} \frac{8\pi}{5} \sqrt{\frac{2}{3}} \sum_{m=-2}^{+2} \frac{\partial}{\partial t} (\dot{Q}_{2m}) \Big|_{r_1}^{r_2} {}_{-2}Y_{2m}(\Theta, \Phi), \quad (7)$$

where  $\Theta$  and  $\Phi$  are the angles associated with the location of the source in the sky, and  ${}_{-2}Y_{2m}$  are the spin-weighted spherical harmonics.

### 2.4 Ensemble Empirical Mode Decomposition

To decompose our set of GW signals into a finite number of simple oscillatory components, known as intrinsic mode functions (IMFs), we employ the ensemble empirical mode decomposition (EEMD) method [118, 119, 120], following the approach described in Cusinato, Obergaulinger, and Aloy [58]. This technique mitigates mode mixing by adding random Gaussian noise to the signal before each decomposition; the resulting IMFs are then averaged to obtain a noise-cancelled ensemble.

The decomposition of each GW signal in the post-bounce time interval  $t \in [-0.005 \text{ s}, 0.25 \text{ s}]$  is performed as follows:

- i. Filter the signal to remove frequencies above 3000 Hz;
- ii. Apply standard empirical mode decomposition (EMD) to extract the IMFs and the residual;
- iii. Subtract the residual from the filtered signal;
- iv. Perform EEMD, limiting the number of IMFs to ten, with parameters  $\sigma_0 = 1$  and  $n = 2 \times 10^6$ , where  $\sigma_0^2$  is the variance of the random Gaussian noise, and  $n$  the number of realizations of the signal plus Gaussian noise used to produce a noise-cancelled ensemble.

The EMD and EEMD calculations are carried out using the PyEMD package [121], employing the `akima` interpolation method [122] to determine the local extrema.

### 2.5 Criteria to identify the LTWI in our models

Since there is no analytic theory defining the exact conditions under which the LTWI develops, in this section, we show that our models, in addition to the low magnitude of  $T/|W|$ , satisfy several other diagnostics supporting the interpretation of the observed spiral patterns as manifestations of the LTWI.

**Pattern frequency** The instability exhibits an approximately constant pattern frequency during its active phase. This behaviour is characteristic of shear-type non-axisymmetric instabilities associated with a well-defined corotation point, in contrast to transient convective or stochastic spiral structures [68, 123]. The nearly time-independent frequency observed in our models is consistent with this interpretation (see Section 3.5). For a non-axisymmetric perturbation with azimuthal dependence  $\propto \cos(m\phi - \omega_{\text{mode}}t)$ , the quantity  $\omega_{\text{mode}}$  defines the mode angular frequency, while

$$\Omega_{\text{p}} = \frac{\omega_{\text{mode}}}{m} \quad (8)$$

is the corresponding pattern angular frequency, i.e., the angular rate at which the spiral structure rotates as a whole.

**Corotation region** A corotation radius,  $r_{\text{cor}}$ , exists inside the PNS, defined by the condition

$$\Omega_{\text{rot}}(r_{\text{cor}}) = \Omega_{\text{p}}. \quad (9)$$

The presence of such a corotation point is widely regarded as a necessary condition for the development of the LTWI, as shown in both idealized equilibrium models and CCSN simulations [66, 67, 68, 69]. As we shall see, in our models, the measured mode frequency lies within the range of rotational frequencies inside the PNS, ensuring the existence of an internal corotation region.

**Differential rotation** The instability develops only while significant differential rotation is present. The growth of the spiral coincides with phases in which the fraction of differential rotational energy remains substantial, and weakens as differential rotation is reduced. This dependence on shear is a defining property of the LTWI [69, 123, 72].

**Convective region** The instability preferentially grows when the corotation region overlaps with a convectively unstable layer. Previous studies have shown that buoyancy and shear can cooperate to facilitate mode growth in differentially rotating stars [69, 71, 72]. In our simulations, the spiral amplitude peaks when the corotation region lies within a zone where the square of the Brunt–Väisälä frequency

$$N^2 = \frac{1}{\rho} \frac{\partial \Phi}{\partial r} \left( \frac{1}{c_s^2} \frac{\partial p}{\partial r} - \frac{\partial \rho}{\partial r} \right), \quad (10)$$

satisfies  $N^2 < 0$  (see Section 3.5), further supporting this interpretation.

**Dominant azimuthal modes** The dominant non-axisymmetric modes correspond to low-order azimuthal numbers ( $m = 1, 2$ ), which are characteristic signatures of the LTWI reported in both equilibrium studies and CCSN simulations [66, 124, 72]. The observed morphology and modal hierarchy are therefore consistent with the expected behaviour of the LTWI.

## 3 Results

The five CCSNe models were evolved in 3D for 250 ms after core bounce to investigate the impact of the nuclear EOS on the early post-bounce evolution and on observable signatures such as GW and neutrino emission. The key quantitative properties of the PNS, GW and neutrino signals, and shock development during this phase are summarised in Table 2.

At 250 ms post-bounce, the PNS in all models is still accreting matter and the shock remains stalled at radii of order  $\sim 200$  km. Due to the rapid rotation of the PNS, all models reach values of  $T/|W|$  within the regime where the LTWIs develop ( $T/|W|_{\text{b}} \approx 0.05 - 0.06$ ). Owing to the large amount of rotational energy, all simulations develop strong non-axisymmetric modes characterised by the emergence of large-scale spiral patterns expanding from within the PNS through the post-shock region.

Model name	BH	TS	SL	LS	BB
EOS	BHBA $\phi$	TSO	SLy4	LS220	BBSk3
$T/ W _{\text{ic,b}} [10^{-2}]$	5.2	6.0	5.8	5.8	6.0
$M_{\text{ic,b}} [M_{\odot}]$	0.56	0.48	0.57	0.46	0.50
$R_{\text{ic,b}} [\text{km}]$	12	17	12	19	19
$J_{\text{ic,b}} [10^{48} \text{ erg}\cdot\text{s}]$	1.66	1.26	1.75	1.20	1.39
$E_{\text{diff,ic,b}}/T_{\text{ic,b}}$	0.65	0.68	0.73	0.69	0.69
$T/ W _{\text{b}} [10^{-2}]$	5.23	6.01	5.76	5.78	5.97
$\kappa_{2,[1,15]} [10^{-3}]$	$24.8^{+2.9}$	$27.6^{+2.6}$	$26.0^{+2.4}$	$23.9^{+2.3}$	$26.6^{+2.3}$
$\Delta h_{+, \text{eq}} [\text{cm}]$	441	439	363	384	491
$L_{\nu e, \text{peak}} [10^{53} \text{ erg/s}]$	5.02	5.88	6.97	4.28	6.02
$\kappa_2 [10^{-3}]$	$18.2^{+1.1}$	$20.6^{+1.3}$	$18.9^{+0.7}$	$16.8^{+1.5}$	$20.3^{+1.1}$
$f_{11} [\text{Hz}]$	$159^{+30}$	$181^{+40}$	$185^{+22}$	$181^{+30}$	$174^{+20}$
$f_{22} [\text{Hz}]$	$312^{+18}$	$291^{+30}$	$322^{+35}$	$367^{+40}$	$278^{+36}$
$f_{\nu,1} [\text{Hz}]$	$152^{+30}$	$176^{+35}$	$192^{+31}$	$184^{+35}$	$168^{+44}$
$f_{\nu,2} [\text{Hz}]$	$320^{+47}$	$296^{+35}$	$336^{+55}$	$376^{+49}$	$288^{+31}$
$f_{\text{GW}} [\text{Hz}]$	$312^{+18}$	$296^{+14}$	$328^{+12}$	$360^{+15}$	$288^{+17}$
$f_{h_{\text{char}}/\sqrt{f}} [\text{Hz}]$	314	294	333	373	290
$\kappa_{2,250} [10^{-3}]$	16.9	18.6	16.1	13.3	19.1
$\langle R_{\text{PNS}} \rangle_{\Omega} [\text{km}]$	$62^{+10}_{-14}$	$65^{+9}_{-13}$	$62^{+10}_{-12}$	$59^{+12}_{-13}$	$66^{+9}_{-11}$
$M_{\text{PNS}} [M_{\odot}]$	2.02	1.98	1.98	1.85	1.98
$\langle R_{\text{shock}} \rangle_{\Omega} [\text{km}]$	184	204	209	258	196
$E_{\text{GW}} [10^{47} \text{ erg}]$	2.13	1.90	3.33	3.30	2.03
$E_{\nu} [10^{52} \text{ erg}]$	6.62	6.28	6.22	5.93	6.23
$P_{\text{rot}} [\text{ms}]$	$4.14^{+1.35}$	$4.91^{+1.92}$	$4.44^{+1.65}$	$4.02^{+1.43}$	$5.74^{+1.97}$

Table 2. Models summary and quantitative results. Rows from top to bottom provide: EOS employed in the simulation; ratio between innercore rotational and gravitational energy at core bounce; innercore mass at core bounce; innercore radius at core bounce; angular momentum at core bounce; ratio between differential rotation and rotational energy for the innercore at core bounce; ratio between PNS kinetic rotational energy and gravitational energy at bounce ( $T/|W|$ ); PNS average and standard deviation (superscript) of the tidal Love number ( $\kappa_{2,[1,15]}$ ) in the interval 1 – 15 ms; GW strain range width at bounce time of the + polarization seen by an equatorial observer ( $\Delta h_{+, \text{eq}}$ ); peak electron neutrino luminosity at 250 ms; average and standard deviation (superscript) of the tidal Love number ( $\kappa_2$ ) in the interval 50 – 250 ms; peak frequency of the density spherical harmonics decomposition for  $\ell = 1$ ,  $m = 1$  component ( $\tilde{\rho}_{11}$ ) computed as the Fourier transform and its full width half maximum (FWHM) in the 50 – 250 ms interval ( $f_{11}$ ); peak frequency of the  $\tilde{\rho}_{22}$  Fourier transform and its FWHM in the 50 – 250 ms interval ( $f_{22}$ ); peak frequency below 250 Hz of the Fourier transform and its FWHM for equatorial equivalent neutrino luminosity in the 50 – 250 ms interval (the three flavours have the same peak frequency),  $f_{\nu,1}$ ; peak frequency above 250 Hz of the Fourier transform and its FWHM for equatorial equivalent neutrino luminosity in the 50 – 250 ms interval (the three flavours have the same peak frequency),  $f_{\nu,2}$ ; peak frequency of the GW Fourier transform and its FWHM in the 50 – 250 ms interval ( $f_{\text{GW}}$ ); peak frequency of the characteristic strain,  $h_{\text{char}}/\sqrt{f}$  (the two polarisations have the same peak frequency); PNS tidal Love number ( $\kappa_{2,250}$ ) at 250 ms; average radius of the PNS (computed as an angular average,  $\langle R_{\text{PNS}} \rangle_{\Omega} = \frac{1}{4\pi} \int d\Omega R_{\text{PNS}}(\Omega)$ ) with subscripts and superscripts representing the maximum and minimum deviation from the average at 250 ms, corresponding to the equatorial and polar radius, respectively; mass of the PNS; average shock radius; energy carried away in the form of GWs; cumulative energy carried away as neutrinos; average rotation period of the PNS, computed as  $P_{\text{rot}} = \int_{\text{PNS}} 2\pi\Omega_{\text{rot}}^{-1} dV / \int_{\text{PNS}} dV$ , and its standard deviation (superscript).

### 3.1 Pre-core-bounce evolution

The choice of different EOSs may influence how rotation is amplified and redistributed during the evolution prior to core bounce. Specifically, identical initial rotation profiles do not guarantee identical rotational states at bounce, as the mapping between radius and enclosed mass evolves differently depending on the EOS. For this reason, we analyse the evolution of the collapsing core up to bounce<sup>1</sup>.

At bounce, we define the inner core as the region enclosed between the centre of the star and the outer sonic point ( $|v_r| < c_s$ , with  $c_s$  the sound speed). Although the inner core is defined at bounce, we reconstruct its previous evolution during collapse by identifying its enclosed mass  $M_{\text{ic,b}}$  and tracing this mass shell backward in time. In this way, all inner core quantities are evaluated on a fixed Lagrangian mass coordinate corresponding to the material that forms the inner core at bounce.

We compare the value of  $T/|W|_{\text{ic,b}}$  at bounce, computed as

$$\left( \frac{T}{|W|} \right)_{\text{ic,b}} = \frac{\frac{1}{2} \int_{\text{ic,b}} dV \rho v_{\phi}^2}{\int_{\text{ic,b}} dV \rho \Phi}, \quad (11)$$

<sup>1</sup>Since the simulations are evolved in axisymmetry up to 5 ms before core bounce, this analysis is based on 2D simulations, unless stated otherwise.

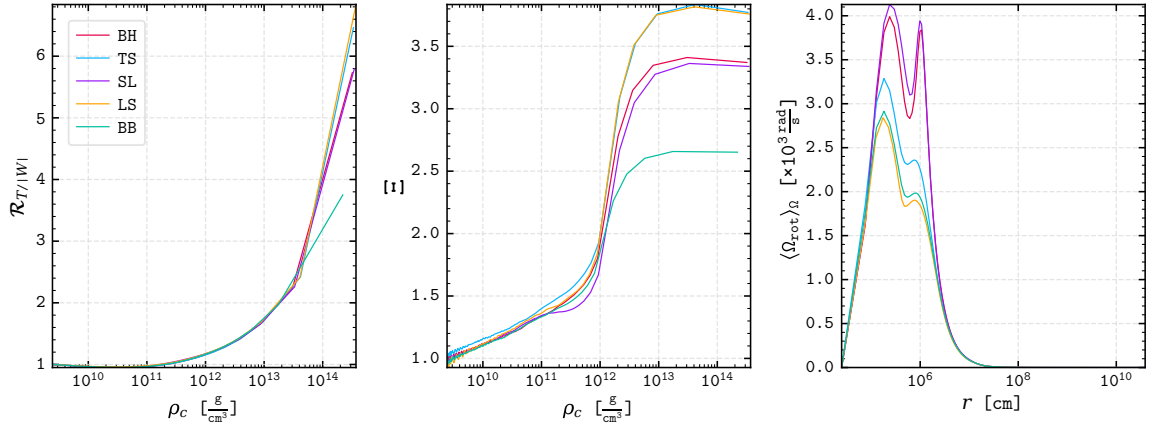


Figure 2. Normalised rotational parameter,  $\mathcal{R}_{T/|W|}$ , (left panel), homology deviation parameter,  $\Xi$  (middle) as a function of the central density,  $\rho_c$ . Right panel: radial profile of the angle-averaged rotational frequency at core bounce.

where  $v_\phi$  is the azimuthal velocity and  $\Phi$  the gravitational potential. This quantity exhibits only moderate relative variations ( $\lesssim 13\%$ ) across the models. The ratio between rotational kinetic and gravitational energy can be approximated, to leading order, as

$$\left(\frac{T}{|W|}\right)_{\text{ic,b}} \sim \frac{J_{\text{ic,b}}^2}{G M_{\text{ic,b}}^3 R_{\text{ic,b}}}, \quad (12)$$

where  $R_{\text{ic,b}}$ , and  $J_{\text{ic,b}}$  are the inner core radius and angular momentum at bounce, respectively. Despite the similar values of  $T/|W|_{\text{ic,b}}$ , the inner core properties differ significantly across models:  $M_{\text{ic,b}}$  ranges from  $0.46$  to  $0.56 M_\odot$ ,  $R_{\text{ic,b}}$  from  $12$  to  $19$  km, and  $J_{\text{ic,b}}$  from  $1.20 \times 10^{48}$  erg · s to  $1.75 \times 10^{48}$  erg · s. We also compute the fraction of differential rotation energy relative to the total rotational energy, obtained by subtracting the rotational energy of an equivalent rigidly rotating configuration as

$$E_{\text{diff}} = T - \frac{1}{2} \frac{J_z^2}{I}, \quad (13)$$

where  $I$  is the moment of inertia and  $J_z$  the  $z$ -component of the angular momentum. We find that restricting to the inner core and evaluated at bounce, the ratio  $E_{\text{diff,ic,b}}/T_{\text{ic,b}}$  varies between  $65\%$  and  $73\%$ .

To remove timing differences during collapse, we compare the evolution of the normalised rotational parameter of the entire system,

$$\mathcal{R}_{T/|W|}(\rho_c) = \frac{T/|W|(\rho_c)}{T/|W|(t=0)}, \quad (14)$$

as a function of the central density  $\rho_c$ .

Assuming angular momentum conservation and homologous contraction, one obtains

$$T \propto \frac{J^2}{I} \propto \frac{1}{R^2}, \quad |W| \propto \frac{GM^2}{R} \propto \frac{1}{R}, \quad \frac{T}{|W|} \propto \frac{1}{R}. \quad (15)$$

The inferred dependence of  $T/|W|$  under homologous contraction motivates the definition of a homology deviation parameter,

$$\Xi(\rho_c) = \frac{T/|W|_{\text{ic}}(\rho_c)}{T/|W|_{\text{ic}}(t=0)} \frac{R_{\text{ic}}(\rho_c)}{R_{\text{ic}}(t=0)}. \quad (16)$$

Here,  $R_{\text{ic}}$  and  $T/|W|_{\text{ic}}$  during collapse are evaluated on a Lagrangian grid defined by the inner core mass at bounce, and assuming that the collapse is spherically symmetric.

The left panel of Figure 2 shows the evolution of  $\mathcal{R}_{T/|W|}$ . Model BB departs from the common trend at  $\rho_c \sim 2 \times 10^{13}$  g/cm<sup>3</sup> and reaches bounce with a value approximately a factor of two smaller than the other models. The remaining models separate into two groups, TS–LS and BH–SL, exhibiting approximately sevenfold and sixfold increases, respectively. The same grouping is reflected in the evolution of  $\Xi$  (middle panel), where deviations from a common trend emerge at  $\rho_c \sim 10^{12}$  g/cm<sup>3</sup>, i.e.,

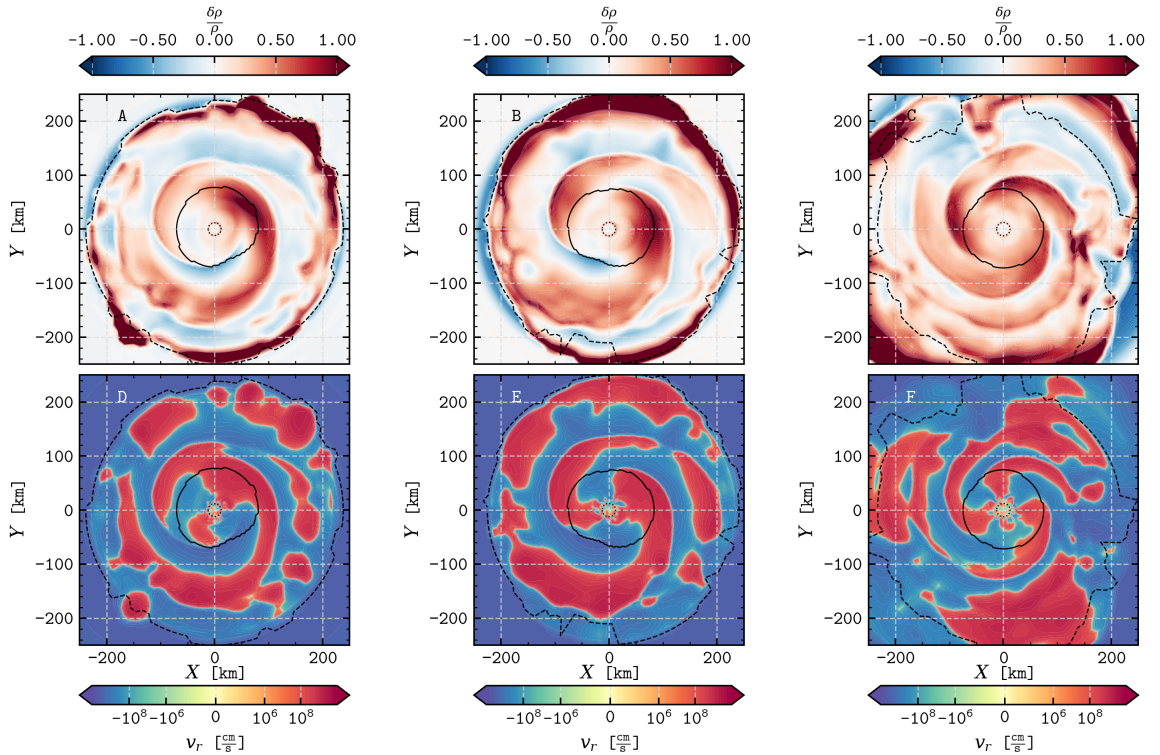


Figure 3. Equatorial slices of the relative deviation from spherical density distribution,  $\delta\rho/\rho$  (top row) and radial velocity,  $v_r$  (bottom row). Left column shows a one-arm spiral at 0.101 s in model LS. Middle and right columns display model BH two- and three-arm spirals at 0.100 s and 0.160 s, respectively. Dashed, solid, and dotted lines represent the isosurfaces at  $10^9$  g/cm<sup>3</sup>,  $10^{11}$  g/cm<sup>3</sup> (as a proxy for the location of the PNS), and  $10^{14}$  g/cm<sup>3</sup>, respectively.

at densities above which neutrinos become trapped. The right panel illustrates that these differences translate into qualitatively distinct angular rotational frequency profiles at bounce. Models BH and SL develop two comparable rotational maxima, and correspondingly stronger differential rotation, while BB, LS, and TS exhibit a single dominant peak. Moreover, the appearance of the outer peak in  $\langle\Omega_{\text{rot}}\rangle_{\Omega}^2$  creates a region outside the inner core where  $d\langle\Omega_{\text{rot}}\rangle_{\Omega}/dr > 0$ . Since the standard local criterion for the axisymmetric magneto-rotational instability (MRI) requires  $d\Omega_{\text{rot}}/dr < 0$ , this positive gradient hinders (on average) the growth of the instability in that layer, i.e., in the region where the MRI would otherwise be expected to develop most easily in a PNS (see, e.g., Rembiasz, Obergaulinger, Cerdá-Durán, Müller, and Aloy [125]).

Overall, this analysis demonstrates that the choice of EOS significantly affects the stratification and rotational structure of the core prior to bounce, even when starting from identical progenitor and initial rotation profiles.

### 3.2 Overview

We describe the evolution of all models, focusing primarily on the equatorial plane, where the non-axisymmetric dynamics (spiral structures associated with the LTWI) are most prominent. Additionally, we assess the degree to which the flow preserves reflection symmetry about the equatorial plane.

**3.2.1 Equatorial plane.** All models develop large-scale spiral patterns once the LTWI sets in, although the detailed morphology and lifetime of the spirals vary significantly across the EOS sample. In all cases, the non-axisymmetric structure originates within the highly deformed PNS and extends into the post-shock region, typically reaching the  $10^9$  g/cm<sup>3</sup> isosurface. As shown in Figure 3, the non-axisymmetric structure is clearly visible in the equatorial plane, both in the radial velocity and in the density deviation from spherical symmetry, defined as

$$\frac{\delta\rho}{\rho} = \frac{\rho - \langle\rho\rangle_{\Omega}}{\langle\rho\rangle_{\Omega}}. \quad (17)$$

<sup>2</sup>Hereafter, we denote with  $\langle A \rangle_{\Omega}$  the solid angle average of a quantity  $A$ , i.e.,  $\langle A \rangle_{\Omega} = (4\pi)^{-1} \int_{4\pi} d\Omega A$ .

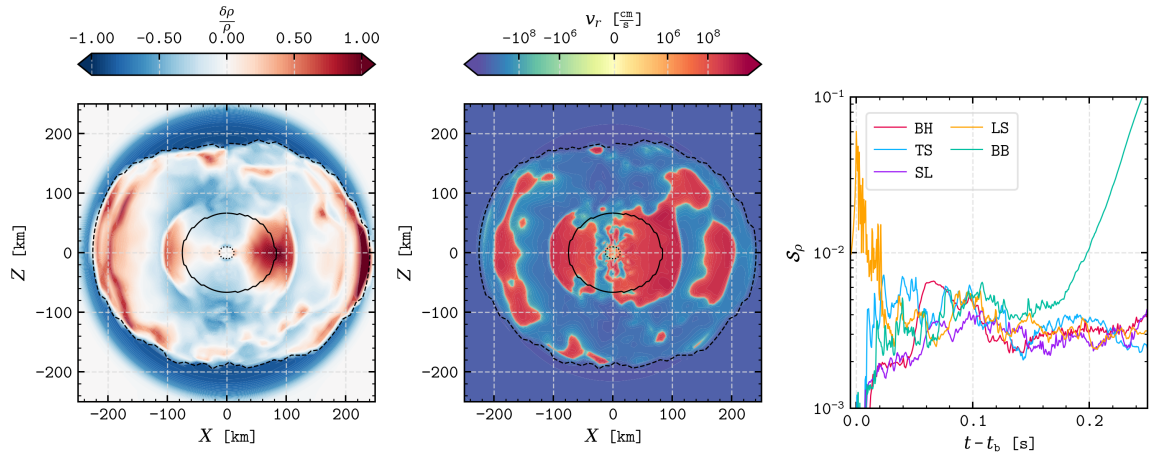


Figure 4. Left and middle panels: polar slices of the relative deviation from the axisymmetric density distribution, and radial velocity, respectively for model BH at 0.101 s. Solid, dashed, and dotted lines have the same meaning as in Figure 3. Right panel, shows the evolution of the density asymmetry score,  $S_\rho$  (Equation (18)), for all models.

The simplest evolution is found in model SL, in which the instability develops into a long-lived two-armed spiral that persists until the end of the simulated interval. By contrast, models TS and BB show a more sequential evolution, in which the spiral first appears as a one-armed pattern and subsequently develops two-armed and three-armed phases before being disrupted. Model BH also exhibits a relatively ordered evolution, forming first a two-armed structure (Figures 3.B and 3.E), and transitioning from a two-armed to a three-armed (Figures 3.C and 3.F) configuration before disappearing. The most complex behaviour is found in model LS, where the morphology changes repeatedly between one-armed (Figures 3.A and 3.D), two-armed, and later multi-armed configurations, with transient additional arms appearing during the nonlinear phase.

The onset time of the spiral activity also differs among models. The earliest spiral develops in model BH at about 50 ms after bounce, whereas the latest onset is found in model BB, where the pattern becomes visible only at about 100 ms. The duration of the strongly non-axisymmetric phase varies accordingly, ranging from relatively short-lived episodes in BH, TS, and BB to a more persistent spiral activity in SL and a more irregular but long-lasting evolution in LS.

Overall, despite these morphological differences, all models show coherent low-order spiral structure whose growth and evolution are consistent with the development of the LTWI. The differences among models are therefore best understood not as a distinction between the presence and absence of the instability, but rather as variations in its dominant azimuthal structure, onset time, and nonlinear evolution.

*3.2.2 Equatorial symmetry.* While the spiral modes cause a strong non-axisymmetric deformation, the system retains an approximate reflection symmetry about the equatorial plane. The spiral arms develop primarily within the equatorial plane, where they extend up to two hundred kilometres from the PNS centre, but no significant asymmetry is observed between the northern and southern hemispheres. The left and middle panels of Figure 4 show the distribution of the density deviation from spherical symmetry and the radial velocity along a vertical slice at a time in which the instability is active. The spiral extends for approximately 100 km in the vertical direction, i.e., its vertical size is roughly comparable to the PNS polar diameter, it is approximately symmetric in density and radial velocity, while it is antisymmetric in azimuthal velocity (not shown).

To quantify the degree of equatorial symmetry, we define the density asymmetry score as:

$$S_\rho = \sqrt{\frac{\int dV (\rho(r, \theta, \phi) - \rho(r, \pi - \theta, \phi))^2}{\int dV \rho^2}}, \quad (18)$$

where we limit the integral to the volume within the  $10^9 \text{ g/cm}^3$  isosurface to capture only the deformation associated with the spiral formation. The right panel of Figure 4 shows the evolution of this quantity for each model. The asymmetry value remains below 1% throughout the evolution in all cases except LS and BB. For model LS the core bounce and subsequent shock formation are somewhat asymmetric. This leads to an initially large asymmetry score, that quickly drops below 1% after

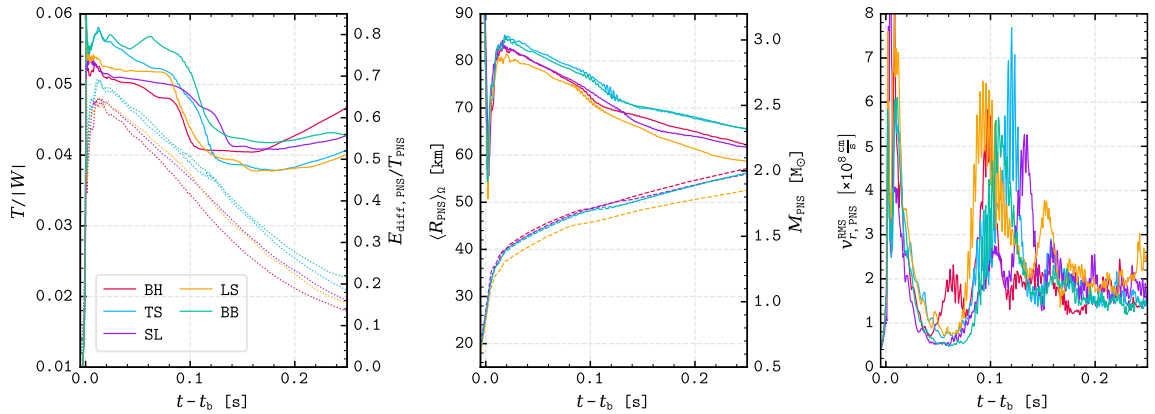


Figure 5. Left panel: evolution of the ratio between rotational and gravitational energy,  $T/|W|$ , of the PNS (solid) and degree of differential rotation  $E_{\text{diff}}/E_{\text{rot}}$  (dotted). Middle panel: PNS average radius (solid) and mass (dashed). Right panel: average residual of the radial velocity inside of the PNS.

$\sim 30$  ms. In model BB, a slightly denser region develops just below the shock front in the northern hemisphere at  $\sim 45^\circ$  from the equatorial plane, making it unrelated to the development of the instability. However, even here the asymmetry ratio reaches at most  $\sim 10\%$ . Thus, the LTWI-driven flow remains approximately equatorially symmetric in most cases, although departures from perfect symmetry do occur. This fact has important implications for the emission of GWs, and, in particular, on the  $\times$ -polarised equatorial component (see Section 3.6).

### 3.3 PNS Structure and Energetics

Following the overview of the instability, we now analyse the evolution of the global PNS properties that regulate the development of the LTWI. The development of spirals in the equatorial plane is associated with the LTWI and induces dynamical changes in the PNS rotational profile and in the shear energy. For this reason, regarding the energetics of the PNS, we analyse the evolution of the ratio between rotational and gravitational energy of the PNS computed as in Equation (11), but extended to the whole PNS defined as the isodensity surface at  $10^{11} \text{ g/cm}^3$ , and the amount of differential rotational energy (Equation (13)). Additionally, we compare the evolution of the PNS masses and radii for our models, and to measure the asymmetric radial motion within the PNS, we define the *PNS residual of the radial velocity* as

$$v_{r,\text{PNS}}^{\text{RMS}} = \sqrt{\langle (v_r - \langle v_r \rangle_{\Omega})^2 \rangle_{\text{PNS}}}, \quad (19)$$

where  $v_r$  is the radial velocity and  $\langle \cdot \rangle_{\text{PNS}}$  denotes averaging over a spherical shell (subscript  $\Omega$ ) or throughout the PNS volume. Finally, to quantify the development of the spiral we employ the time evolution of the normalised azimuthal Fourier amplitudes of the density,

$$A_m(t) = \frac{|\int dV \rho(r, \phi, z, t) e^{im\phi}|}{\int dV \rho(r, \phi, z, t)}, \quad (20)$$

evaluated within the isosurface at  $10^9 \text{ g/cm}^3$ .

In the left panel of Figure 5, we show the evolution of the PNS  $T/|W|$ , as solid lines, which closely connects with the development of the spiral instability.

As reported by [124, 72], a decrease in  $T/|W|$  is associated with the onset of spiral patterns in the context of LTWI. In our simulations,  $T/|W|$  drops from  $\sim 5\%$  to  $\sim 4\%$  on timescales of approximately  $\sim 50$  ms. This decrease is slightly lower than the  $5\%$  found by [124], but higher than the  $2.3\%$  observed in model H studied by [72]. Additionally, in [72] the  $T/|W|$  reduction in the model that develops LTWI compared to the 2D counterpart that does not develop it is less sharp than in the other cases. Across all models, variations in  $T/|W|$  are correlated with the development and decay of the spiral instability. In particular, local decreases of  $T/|W|$  coincide with the emergence of spiral arms. The instability shows greater activity (as quantified by  $A_m$ ; see below) when  $T/|W|$  reaches its minimum, after which the ratio remains approximately constant while the spiral pattern is sustained. At later times, the increase of  $T/|W|$  coincides with the weakening and eventual disruption of the spiral structure.

An illustrative example is model BH: the accelerated decrease observed at  $\approx 50$  ms marks the initial emergence of a two-armed spiral. The second more pronounced decay happening at  $\approx 100$  ms,

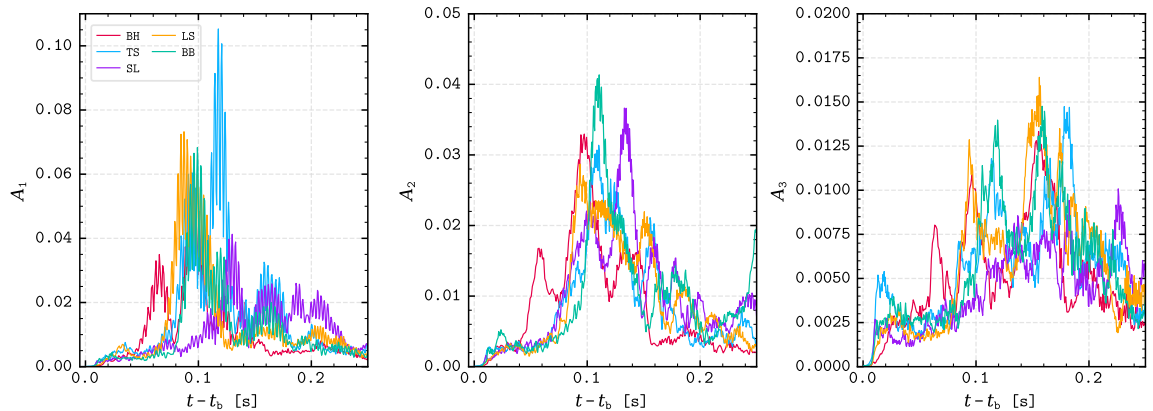


Figure 6. Evolution of the normalised azimuthal Fourier amplitudes of the density for  $m = 1$  (left panel),  $m = 2$  (middle panel) and  $m = 3$  (right panel). Note the scale difference on the  $y$ -axis.

corresponds to its full development. Finally, by 160 ms the spiral is totally disrupted as  $T/|W|$  rises back to approximately its original value.

However, a low value of  $T/|W|$  is not a sufficient condition for the development of the instability. Another crucial requirement is that the PNS be differentially rotating [68, 123]. Using Equation (13), we compute the fraction of differential-rotation energy relative to the total rotational energy (left panel of Figure 5, dotted line). As in [72], the energy at bounce is approximately equally distributed between rigid and differential rotation. After bounce, the fraction of differential-rotation energy increases to  $\sim 70\%$  at  $\sim 20$  ms, before decreasing nearly linearly, reaching 15 – 20% of the total by 250 ms. Notably, the instability develops when the differential-rotation energy remains relatively high, at least 45% of the total.

The formation of the spiral and the onset of the LTWI are tied to the rotation rate of the models and also have consequences on the PNS evolution. In all models, the PNS continues to accrete mass throughout the simulation. The stiffer EOS of model LS produces a PNS with a mass consistently lower by approximately  $0.15 M_{\odot}$  compared to the other models (dashed line in the mid panel of Figure 5). After about 40 ms, however, the accretion rates among all considered EOSs converge to similar values. Over the same period, the PNS average radii show only minor differences, differing by less than 5 km.

Between 75 ms and 125 ms, all models undergo a brief phase lasting approximately 10 ms during which the PNS accretion rate temporarily drops to nearly zero before recovering to its previous level. In this interval, the PNS contraction also accelerates, leading to a more rapid decrease in radius. This transient behaviour coincides with the onset of the LTWI. The spiral mode development transports angular momentum outward from the PNS into the post-shock region. The associated increase in centrifugal support drives an outward mass flux that temporarily counteracts accretion onto the PNS, producing the observed drop in the accretion rate.

The right panel of Figure 5 shows relatively broad peaks in  $v_{r,\text{PNS}}^{\text{RMS}}$ . Looking, e.g., at equatorial maps of  $\delta\rho/\rho$ , these peaks coincide with the formation of one or more spiral arms, with the largest values occurring when the instability is fully developed. In some models (e.g., BH), these peaks coincide with the small drops in  $T/|W|$  shown in Figure 5, supporting a connection between at least some of the local decreases in  $T/|W|$  and the emergence of spiral arms. More generally, we find a broad correlation whereby larger peaks in  $v_{r,\text{PNS}}^{\text{RMS}}$  are associated with larger drops in  $T/|W|$ .

Figure 6 shows the evolution of the normalised Fourier amplitudes for  $m = 1, 2,$  and  $3$  in our model sample. The growth of these amplitudes indicates the development of non-axisymmetric spiral structure, with the dominant mode identified by the largest  $A_m$ . In all models except SL, the  $m = 1$  (left panel) component dominates over  $m = 2$  (middle), and  $m = 3$  (right) during the first 100 ms post-bounce. At later times, either the  $m = 1$  or  $m = 2$  mode becomes dominant depending on the model, while  $m = 3$  remains subdominant. In model SL, the  $m = 2$  component dominates throughout the LTWI evolution, consistent with the presence of a sustained two-armed spiral, as discussed in Section 3.2. We take the maximum amplitude of the dominant Fourier component as a proxy for the saturation of the LTWI and the peak development of the spiral. Moreover, we find that the largest peaks in  $A_m$  coincide in time with the largest peaks in  $v_{r,\text{PNS}}^{\text{RMS}}$  (Figure 5), which supports the use of  $v_{r,\text{PNS}}^{\text{RMS}}$  as a proxy for the onset and relative strength of the instability. In the following, we employ a spherical harmonics decomposition rather than a Fourier decomposition, as it provides a more

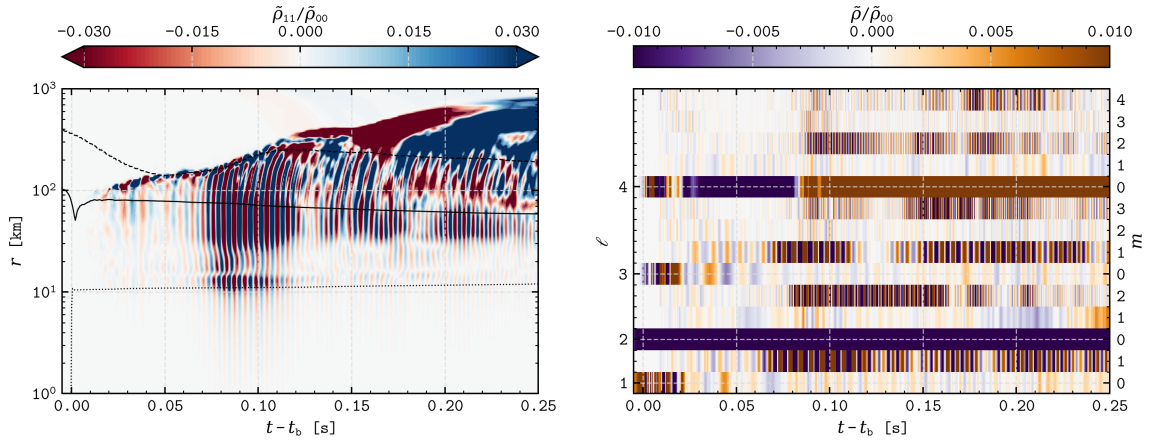


Figure 7. Left panel: space-time evolution of the spherical harmonics decomposition of the density for  $\ell = 1$ ,  $m = 1$ , normalised by the  $\ell = 0$ ,  $m = 0$  component. Dotted, solid, and dashed lines represent the isosurfaces at  $10^{14}$ ,  $10^{11}$ , and  $10^9$  g/cm<sup>3</sup>, respectively. Right panel: evolution of the normalised spherical harmonics decomposition of the density at  $r = 30$  km, for  $0 < \ell \leq 4$  and  $m \geq 0$ . Both panels refer to model LS.

complete characterization of the angular structure and enables a direct morphological comparison with the GW signal.

### 3.4 Spherical harmonics decomposition

To quantitatively characterise the development of the LTWI, we analyse the growth of its non-axisymmetric modes using a spherical-harmonic decomposition of the density field. The spherical harmonics coefficients of the density on a sphere of radius  $r$  are

$$\tilde{\rho}_{\ell m}(r) = \int d\Omega \rho(r, \theta, \phi) Y_{\ell m}(\theta, \phi), \quad (21)$$

where  $Y_{\ell m}(\theta, \phi)$  are the (real) spherical harmonics, defined as

$$Y_{\ell m}(\theta, \phi) = \begin{cases} \sqrt{2}(-)^m \Im[Y_{\ell m}^{\text{cpx}}(\theta, \phi)], & \text{if } m < 0 \\ \Re[Y_{\ell m}^{\text{cpx}}(\theta, \phi)], & \text{if } m = 0 \\ \sqrt{2}(-)^m \Re[Y_{\ell m}^{\text{cpx}}(\theta, \phi)], & \text{if } m > 0 \end{cases}. \quad (22)$$

where  $Y_{\ell m}^{\text{cpx}}$  are the complex spherical harmonics,

$$Y_{\ell m}^{\text{cpx}}(\theta, \phi) = \sqrt{\frac{2\ell + 1}{4\pi} \frac{(\ell - m)!}{(\ell + m)!}} P_{\ell m}(\cos \theta) e^{im\phi}, \quad (23)$$

and  $P_{\ell m}$  are the associated Legendre polynomials, computed as

$$P_{\ell m}(\cos \theta) = (-)^m 2^\ell (1 - \cos^2 \theta)^{m/2} \sum_{k=m}^{\ell} \frac{k!}{(k-m)!} \cos^{k-m} \theta \binom{\ell}{k} \binom{(\ell+k-1)/2}{\ell}. \quad (24)$$

The spiral deformation is associated with the  $\ell = m$  components. Specifically, the number of azimuthal arms in the equatorial deviation from the axisymmetric density and radial velocity corresponds to the order  $m$  of the dominant spherical harmonic.

Figure 7 shows this decomposition for model LS, which we select as it exhibits the richest mode evolution, thus providing a clear link between the large-scale structure described in Section 3.2 and its harmonic content. The left panel of Figure 7 shows the space-time evolution of the normalised  $\tilde{\rho}_{11}/\tilde{\rho}_{00}$  amplitude. The  $(\ell, m) = (1, 1)$  component emerges in two distinct radial regions that become active during the initial development of the LTWI at approximately 75 ms. The first is an inner region, where the  $(\ell, m) = (1, 1)$  component remains confined within  $r = 20$  km and disappears around 110 ms, i.e., while the spiral mode is active. For this reason and because Figure 3 indicates that the spiral structure originates at  $r > 20$  km, we suggest that the inner region does not contribute to the development of the large-scale spiral. The second is an outer region above  $\sim 25$  km extending to the PNS surface. This outer component, however, is not restricted to the PNS interior, but propagates

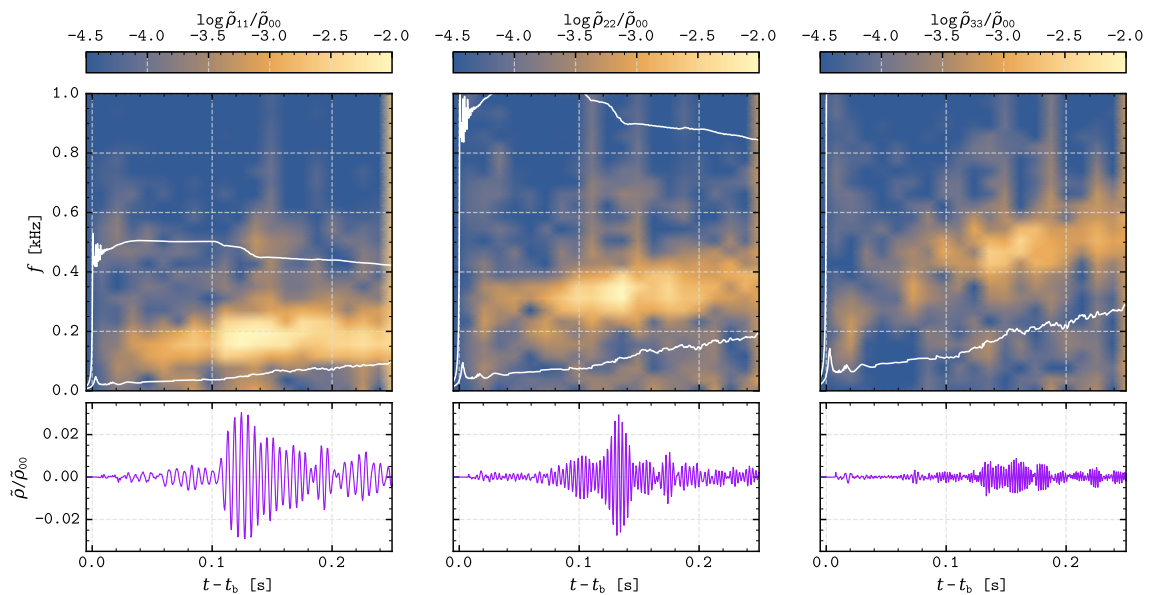


Figure 8. Spectrograms of the normalised spherical harmonics decomposition of the density performed with a time window of 20 ms (top row) and corresponding time series (bottom row) for  $(\ell, m)$  equal to (1, 1), (2, 2), and (3, 3) for model SL at  $r = 30$  km. White lines represent the maximum rotation frequency within the PNS and the surface-averaged rotation frequency, both multiplied by  $m = 1, 2$ , and 3 from left to right.

outward at a reduced speed, eventually reaching the shock. These two zones are separated by a transition layer in which their contribution overlaps.

To determine the hierarchy of unstable modes, in the right panel of Figure 7, we display the time evolution of all spherical-harmonic amplitudes with  $\ell \leq 4$  and  $m \geq 0$  evaluated at a radius of 30 km, which lies within the instability region. Throughout the evolution we observe contributions from all  $\ell = m$  modes, together with  $(\ell, m) = (3, 1)$ ,  $(4, 2)$ , and  $(4, 0)$ .

Two purely axisymmetric components arise from the changing deformation due to the rapid rotation rather than any instability. The axisymmetric quadrupole,  $(2, 0)$ , is negative throughout the evolution, consistent with the high degree of equatorial flattening produced by the rapid rotation. The behaviour of the axisymmetric hexadecapole,  $(4, 0)$ , is more complex. Its sign change indicates an evolution of the higher-order structure of the deformation, reflecting variations not only between the polar and equatorial regions but also at intermediate latitudes.

The  $(\ell, m) = (1, 1)$  mode appears at  $\sim 70$  ms and persists through the simulation, indicating the formation of a one-armed spiral. Around  $\sim 80$  ms the  $(\ell, m) = (2, 2)$  component emerges, marking the development of a second arm. Between  $\sim 150$  ms and  $\sim 220$  ms the appearance of the  $\ell = m = 3$  and  $\ell = m = 4$  components signals the growth of additional arms and the progressive fragmentation of the pattern. The presence of  $(3, 1)$  and  $(4, 2)$  modes shows that the spiral has a three-dimensional character and couples to the background rotational deformation; these mixed-order modes indicate vertical structure and mode–mode coupling. However, their amplitudes remain subdominant, and the overall flow preserves north–south symmetry to a high degree.

Overall, the modal evolution recovered from the spherical–harmonic analysis matches the qualitative behaviour described in Section 3.2. The appearance, ordering, and spatial origin of the modes depend on the specific flow geometry of each model and reflect the non-linear development of the LTWI.

In order to characterise the frequency of the instability, we compute the spectrograms of  $\tilde{\rho}_{\ell m}/\tilde{\rho}_{00}$  at a radius of  $r = 30$  km, within the region where the instability produces the strongest pattern. In Figure 8 we show the spectrograms of the  $(\ell, m) = (1, 1)$ ,  $(2, 2)$ , and  $(3, 3)$  components in the top row, together with the corresponding time series in the bottom row, for model SL.

A rotating pattern with azimuthal number  $m$  produces  $m$  oscillation cycles per rotation period, and the characteristic signal frequency is

$$f \simeq m f_{\text{rot}}, \quad (25)$$

where  $f_{\text{rot}} = \Omega_{\text{rot}}/2\pi$  is the linear rotational frequency. Therefore, plotting  $m f_{\text{rot}}$  in spectrograms provides a useful reference for identifying the frequencies associated with rotating non-axisymmetric modes. The  $\ell = m = 1$  mode, present from (at least) 50 ms, becomes stronger at approximately

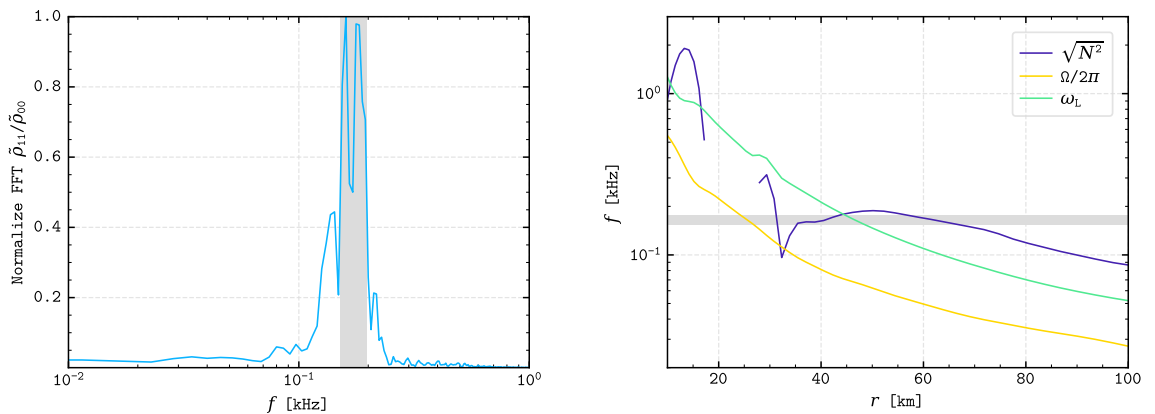


Figure 9. Left panel: normalised Fourier transform of the  $\tilde{\rho}_{11}/\tilde{\rho}_{00}$  averaged between  $r = 25$  km and  $r = 45$  km for the time interval 75 – 170 ms for model TS. The shaded rectangle represents the FWHM, computed from the locations at which the normalised Fourier transform is equal to half of its maximum value. Right panel: propagation diagram of the equatorial profiles of rotation (yellow), Brunt–Väisälä (blue), and Lamb (green) frequencies at 110 ms. The band represents the FWHM of the dominant frequency of the mode (1, 1).

100 ms with a frequency of about 170 Hz (left panel of Figure 8). In contrast to previous works [124, 71, 72], in our models, irrespective of the EOS, the mode frequency remains almost constant throughout the entire instability phase. According to [68, 123, 126], the LTWI is triggered when the frequency of one of the PNS modes matches the local rotation frequency, defining a corotation point. The maximum rotation frequency of the differentially rotating PNS is located near the centre, while the minimum is found near the surface. As indicated by the white lines, which represent these extrema, the  $\ell = m = 1$  mode possesses at least one corotation point inside the PNS, since its frequency lies between the two curves.

In the middle panel of Figure 8, we present a similar analysis for the  $\ell = m = 2$  mode, which is directly associated with the two-armed spiral structure. This mode appears at approximately 80 ms with a frequency roughly twice that of the  $\ell = m = 1$  mode, and it remains essentially constant during the time in which the amplitude of the mode is enhanced (0.1 – 0.2 s). Again, a corotation point lies within the PNS, as the mode frequency is enclosed by the maximum and minimum rotational frequencies multiplied by  $m = 2$ .

In the right panel of Figure 8 we show the  $\ell = m = 3$  mode, which becomes visible at later times, around 120 ms. Its frequency is roughly three times that of the  $\ell = m = 1$  mode, and it is also enclosed between three times the maximum and minimum PNS frequencies, indicating once again a corotation point.

The bottom panels of Figure 8 compare the time-series amplitudes of these modes. This comparison clearly shows that the  $\ell = m = 2$  mode dominates the early dynamics of the LTWI phase in model SL, consistently with the observed two-armed spiral. The  $\ell = m = 1$  mode becomes relevant only at later times, and  $\ell = m = 3$  mode remains subdominant.

Despite the differences introduced in the rotation profile and in the stratification of the inner core during collapse evolution (Section 3.1), and consequently in the PNS structure, the LTWI develops in all models considered. In particular, the instability sets in within a comparable post-bounce time interval of 50 – 90 ms in all cases, which indicates that its onset is a feature largely independent from the choice of the EOS. At the same time, quantitative properties of the instability exhibit a dependence on the EOS. In particular, the pattern frequency varies between models, reflecting differences in the structure of the PNS. Additionally, variations are observed in the dominant azimuthal structure of the spiral modes, as well as in the associated GW emission (see Section 3.6). These results suggest that the development of the LTWI is a robust outcome in our model set, whose characteristics are sensitive to the underlying microphysics encoded in the EOS.

### 3.5 Characterization of the corotation regions

Building upon the results presented in Section 3.4, we determine the temporal evolution of the corotation radius,  $R_{\text{cor}}$ . Since the LTWI exhibits an approximately constant pattern frequency during its saturated phase, we estimate this frequency from the Fourier spectrum of the  $(\ell, m) = (1, 1)$  mode over the time interval in which the instability is active. We compute the Fourier transform at radii between 25 km and 45 km, in 1 km increments, and average the resulting spectra over this radial interval. The pattern frequency is then identified with the maximum of this radially averaged

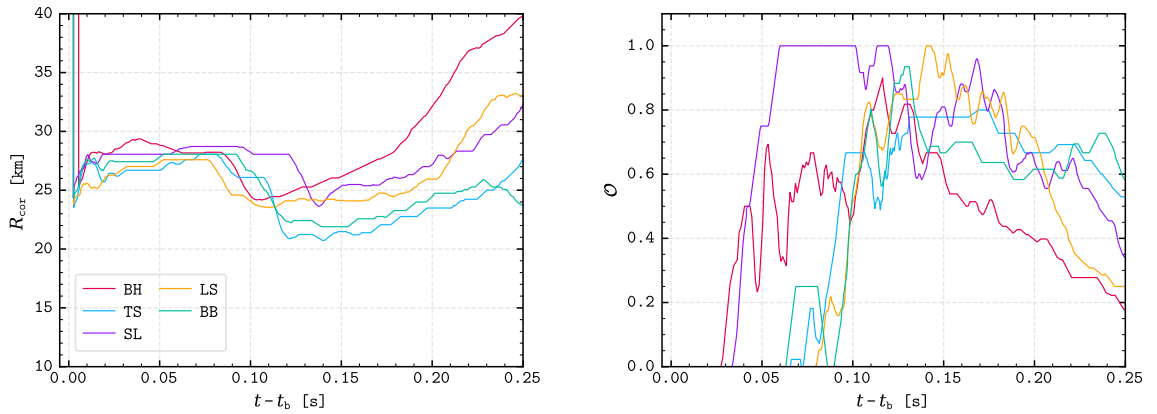


Figure 10. The left and right panels show the evolution of the average corotation radius, and overlap between the corotation and convective regions for all the models, respectively.

spectrum, and the spectral width is estimated from its FWHM. This procedure, illustrated for model TS in the left panel of Figure 9 provides a robust estimate of the global pattern speed while reducing the sensitivity to local fluctuations at individual radii.

Since we have extracted a band of frequencies, we define a corotation region,  $R_{\text{cor}}$ , which spans several kilometers, as the radial interval for which the equatorial rotation frequency satisfies

$$f_{\text{rot}} \in \left[ f_{\text{mode}} - \frac{\Delta f}{2}, f_{\text{mode}} + \frac{\Delta f}{2} \right], \quad (26)$$

with  $\Delta f$  being the FWHM.

To assess where the corotation region lies within the PNS, in the right panel of Figure 9 we show the radial profiles of the rotation, Brunt–Väisälä angular frequency,

$$\omega_{\text{BV}} = \frac{|N|}{2\pi}, \quad (27)$$

and Lamb frequency

$$\omega_{\text{L}} = \frac{1}{2\pi} \frac{\sqrt{\ell(\ell+1)}c_s}{r}, \quad (28)$$

evaluated for  $\ell = 1$ , and where  $c_s$  is the sound speed.

We use the Brunt–Väisälä frequency as a proxy to locate zones of convective instability, as  $N^2 < 0$ . Consistent with previous work [69, 71, 72], the growth of the LTWI is strongest when the corotation region lies within such a convectively unstable zone. Furthermore, previous studies [123, 126] indicate that the unstable mode associated with the LTWI is not a  $p$ -mode, which requires  $f_{\text{mode}} \gtrsim \omega_{\text{L}}$  for acoustic propagation, but is instead consistent with  $f$ -,  $g$ -, or  $i$ -modes.

We define the radial extent of the convectively unstable region (where  $N^2(r, t) < 0$ ) at each time  $t$  as the interval

$$[r_-(t), r_+(t)]. \quad (29)$$

In a similar fashion, the spectral width of the corotating mode taken as the instantaneous FWHM defines a corotation region

$$[r_{\text{cor}}^-(t), r_{\text{cor}}^+(t)]. \quad (30)$$

Since, in the models considered here, the convectively unstable layer and the corotation region each form a single connected radial interval, we measure the fractional radial overlap between the corotation region and the convectively unstable layer with the *overlap function*

$$\mathcal{O}(t) = \frac{\max[0, \min(r_+(t), r_{\text{cor}}^+(t)) - \max(r_-(t), r_{\text{cor}}^-(t))]}{r_{\text{cor}}^+(t) - r_{\text{cor}}^-(t)}, \quad (31)$$

which, by construction, is 0 if there is no overlap between the two regions, while  $\mathcal{O} = 1$  if the corotation region is fully embedded in the convective layer.

Figure 10 shows the evolution of the corotation radius and of the overlap function for all models, in the left and right panels, respectively. In each case,  $R_{\text{cor}}$  initially moves inward entering the convectively unstable zone of the PNS. As the corotation region continues to shrink, its overlap with

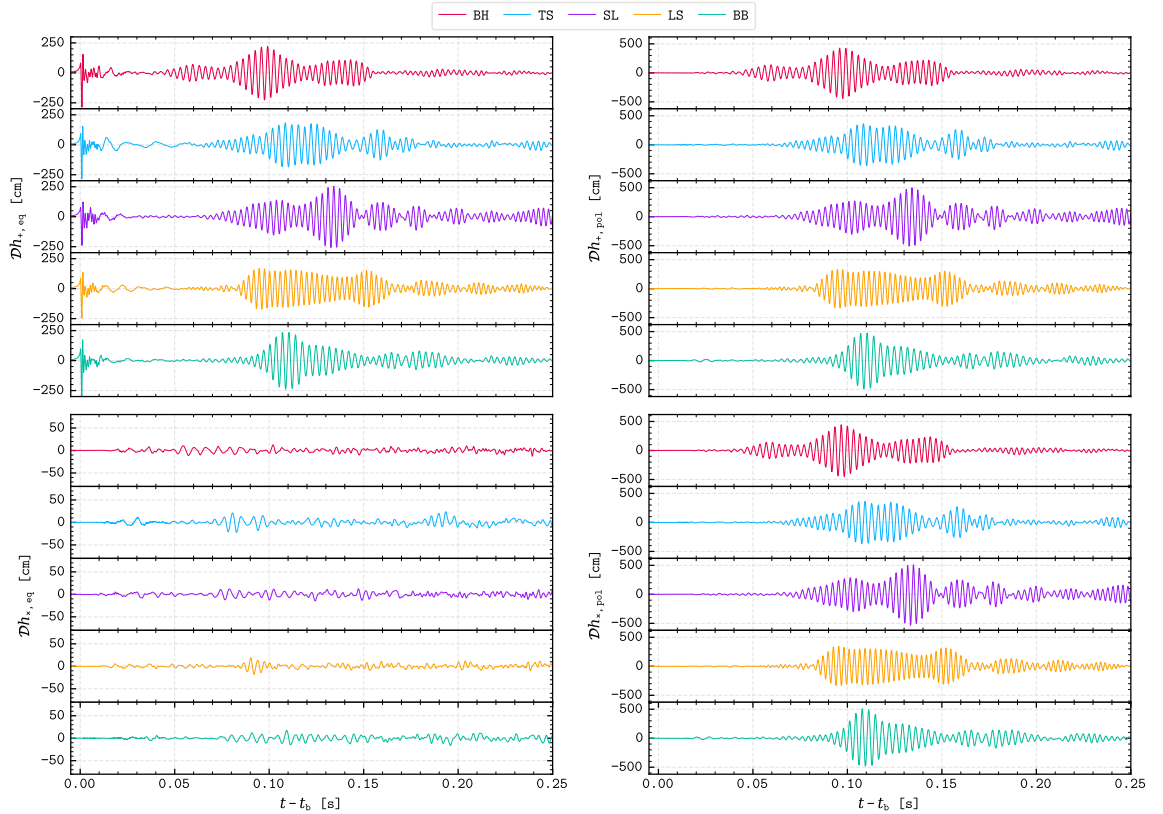


Figure 11. GW strains emitted by a source at a distance  $\mathcal{D}$ . The top and bottom left panels show the strains measured at the equator for the  $+$  and  $\times$  polarisations, respectively. The top and bottom right panels show the corresponding polarisations measured along the polar axis. Each panel contains results from models BH, TS, SL, LS, and BB.

the convectively unstable zone increases. In our limited sample of models, the onset of the LTWI happens when the overlap reaches  $\gtrsim 50\%$ , while the instability strength is maximum (as indicated by the peak of the Fourier amplitudes in Figure 6) when the corotation radius reaches its minimum value and the overlap between the corotation and convective regions reaches  $\gtrsim 75\%$ . After the instability peak, with the loss of differential rotation, the corotation region gradually moves outward, eventually exiting the convective zone. Model SL constitutes an exception: the two regions show complete overlap  $\sim 50$  ms before the instability begins to develop. This discrepancy may stem from the limitations of the definition of the convective region, which is based on the equatorial average of the Brunt–Väisälä frequency, and may not fully capture the multidimensional structure of convection.

Based on the results presented so far, we conclude that the observed dynamics is due to the development of a LTWI. The presence of substantial differential rotation and the evolution of the  $T/|W|$  ratio place the system in a regime susceptible to shear instabilities [69, 123, 72]. The development of large-scale non-axisymmetric spiral patterns and the growth of  $m = 1$  and  $m = 2$  components in the Fourier amplitudes and the  $\ell = m$  coefficients in the spherical harmonics decompositions, indicates the emergence of a coherent global mode [66, 124, 72]. The approximately constant pattern frequency, together with the fact that the dominant emission frequencies lie within the range of the angular velocity inside the PNS, are consistent with the presence of a corotation region. The corotation region is also located within a convectively unstable layer, a condition that has been identified in previous studies as necessary for the development of the LTWI [66, 67, 68, 69].

We now turn to a description of the impact of the LTWI on the multimessenger emission, more specifically on the GW and neutrino signals.

### 3.6 Gravitational waves

**3.6.1 Overall evolution** In this section we focus on the impact of the LTWI on the GW emission. Figure 11 shows the two independent polarisations,  $+$  and  $\times$ , emitted by a source at a distance  $\mathcal{D}$  measured along the polar axis (pol) and the equator (eq).

Before discussing the behaviour of individual models, we summarise the features common to all of them. All models emit only a weak signal with  $\times$  polarization in equatorial directions, with

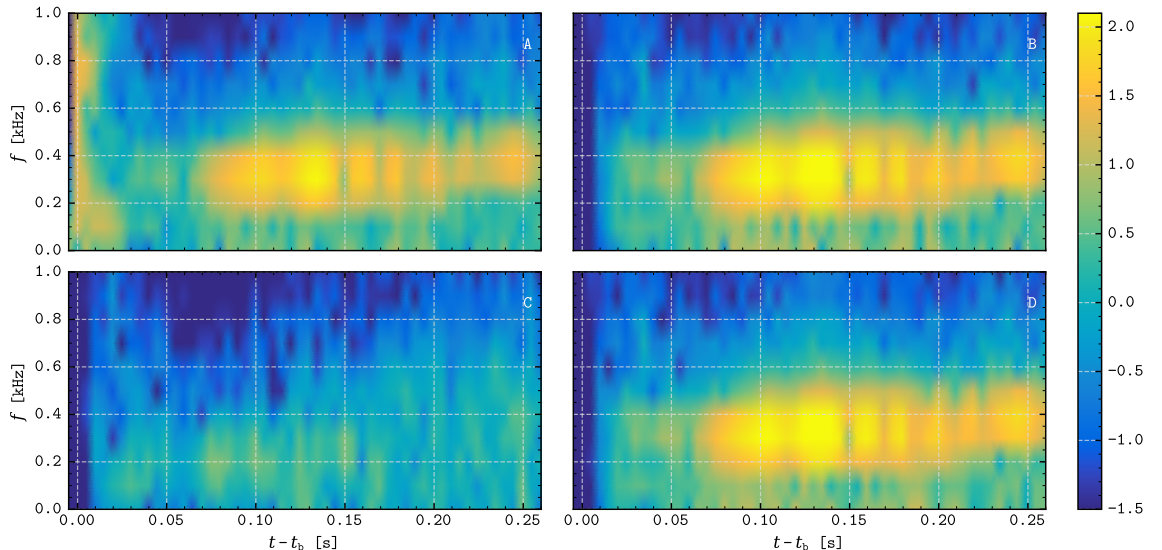


Figure 12. Spectrograms of the GW strains measured at the equator (panels **A**: + polarization, and **C**:  $\times$  polarization) and along the polar axis (panels **B**: + polarization, and **D**:  $\times$  polarization) for model SL.

an amplitude  $|\mathcal{D}h_{\times,\text{eq}}| \lesssim 20$  cm. This is a direct consequence of the system being approximately symmetric about the equator, as described in Section 3.2.2. In contrast, the + polarization for equatorial observers exhibits the characteristic bounce signal of rapidly rotating progenitors: a slow rise followed by a sharp drop, with a strain width (i.e., the difference between the highest and lowest points in the bounce signal) of 360 – 490 cm. Once the LTWI develops, the signal amplitude increases to  $|\mathcal{D}h_{+,\text{eq}}| \sim 250$  cm, with a morphology that depends on the specific model and is described below.

Along the polar direction, the two polarisations show morphologies very similar to each other and to  $h_{+,\text{eq}}$ , aside from the absence of the bounce feature. The GW signal grows to about  $|\mathcal{D}h_{+,\times,\text{pol}}| \sim 500$  cm, i.e., twice as high as the emission in an equatorial direction,  $|\mathcal{D}h_{+,\text{eq}}|$ . The two polar polarization components are phase-shifted by  $\pi/2$ ; otherwise they are morphologically equivalent.

Furthermore, the morphology of the polarisations, once the LTWI develops, is similar to the time series of the  $(\ell, m) = (2, 2)$  mode of the density decomposition (middle panel of Figure 8). To quantify this correspondence we use the matching score,  $\mathcal{M}$ , [127]:

$$\mathcal{M} = \frac{\langle S_1(t) | S_2(t) \rangle}{\sqrt{\langle S_1(t) | S_1(t) \rangle \langle S_2(t) | S_2(t) \rangle}}, \quad (32)$$

where  $S_i(t)$  denotes the two signals, and  $\langle \cdot | \cdot \rangle$  represents the inner product. Specifically, we compare  $h_{\times,\text{pol}}$  with the  $(\ell, m) = (2, 2)$  spherical-harmonic component of the density at 40 km, during the period of activity of the instability (50 – 250 ms). This analysis reveals that each model has a  $\mathcal{M} \geq 0.7$ , indicating that the evolution of  $h_{\times,\text{pol}}$  closely tracks that of the  $(2, 2)$  mode.

We now turn to a model-by-model description of the detailed GW morphology during the growth and saturation of the LTWI. Since the morphology of the polarisations is similar to one another, we focus on  $h_{+,\text{pol}}$ , referring to the upper right panel of Figure 11.

The temporal evolution of the GW enhancement differs across the models. Model BH shows an enhanced phase lasting  $\sim 100$  ms (50 – 150 ms): the signal grows over several tens of milliseconds, reaches a peak, and then gradually weakens until disappearing at 150 ms. In model TS, the amplitude increases progressively, reaching a maximum at  $\sim 100$  ms and remaining enhanced for  $\sim 40$  ms before weakening and fragmenting into a final clump of emission. The signal in model SL rises more slowly, peaking at 135 ms and then dropping sharply, after which only weak, isolated pulses remain. Model LS instead shows a rapid increase in amplitude, with the peak level sustained for more than 100 ms before declining; the subsequent emission appears in short bursts of moderately enhanced strength. Finally, model BB displays a rapid increase followed by a gradual decay of the signal until the end of the simulation.

To summarise, the five models are similar in terms of the maximum amplitude and the duration of the time during which the emission is strongest. They differ when it comes to the time at which the enhanced emission starts and how fast it rises as well as the activity in the form of late pulses.

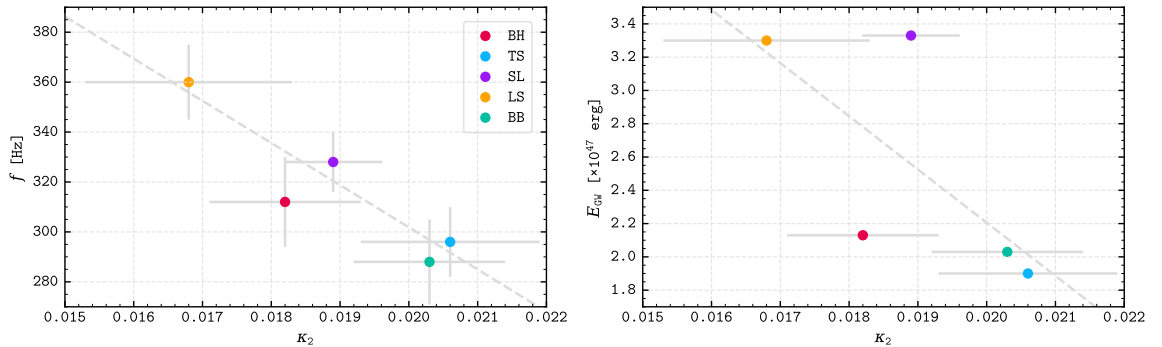


Figure 13. Left panel: dominant frequency of the GW signal associated with the LTWI against the average tidal Love number  $\kappa_2$ . Right panel: energy emitted in GWs until 250 ms against  $\kappa_2$ . Errors on the x-axis represent the standard deviation from the average value of  $\kappa_2$ . Errors on the y-axis represent half of the FWHM. The dashed line represents the linear fit.

A complementary view of the aforementioned features in the time-frequency domain is provided by the spectrogram of the GW signal. In Figure 12 we display time-frequency maps of the two polarisations for polar and equatorial observers of model SL performed with a time window of 15 ms.

The equatorial symmetry is reflected in the suppression of the  $\times$  polarization for equatorial observers (panel C). The emitted power remains weak throughout the simulation and no specific emission frequency is observed. On the other hand, the  $+$  polarization on the equator (panel A) shows the broad-band, loud emission associated with core bounce [3]. This signal is followed by a low-frequency ( $f \leq 250$  Hz) weaker component lasting for  $\sim 30$  ms, which corresponds to prompt convection (described in [58] for axisymmetric models).

Once the LTWI develops, a strong feature emerges. A strong GW signal begins at  $\sim 75$  ms with a frequency of  $\sim 320$  Hz in all polarisations except  $h_{\times,eq}$ . This feature persists until the end of the simulation, maintaining an approximately constant frequency. Panels A, B, and D show that this component is present in  $h_{+,eq}$ ,  $h_{\times,pol}$ , and  $h_{+,pol}$ , and it is consistent with the  $(\ell, m) = (2, 2)$  character of emission. Comparing these spectrograms with the spherical-harmonic decomposition of the density (see middle panel of Figure 8) we find that the  $(2, 2)$  mode exhibits the same frequency and temporal evolution as the GW signal. Moreover, we remark that not only the GW and  $(2, 2)$  mode frequencies closely align, but also the overall morphology of the waveform resembles that of the time series of the density mode.

Since the GW emission associated with the development of the LTWI shows an approximately constant frequency throughout the active phase, we can extract its dominant frequency using the same procedure employed in Section 3.5 for the  $(\ell, m) = (1, 1)$  mode. Specifically, we compute the Fourier transform of  $h_{\times,pol}$  over the interval in which the instability is active (50 – 250 ms). We then identify the peak frequency, with an uncertainty given by the FWHM. These peak frequencies coincide with those of the  $(2, 2)$  density mode (see Table 2).

To assess how the choice of the EOS influences this emission, we use the tidal Love number of the PNS. For each model, we construct the time series of  $\kappa_2$  and compute its mean and standard deviation over the same 50–250 ms window.

The left panel of Figure 13 shows the dominant GW frequency associated with the LTWI plotted against the average tidal Love number. We observe that a clear trend emerges: models with a smaller Love number, which in our convention correspond to more compact/stiffer PNS configurations, emit at higher frequencies. On the contrary, larger values of  $\kappa_2$ , correlated in our models with softer EOSs, produce lower frequencies. A linear fit to the data yields

$$f = (-17.4 \pm 4.0) \times 10^3 \kappa_2 + (6.4 \pm 8) \times 10^2, \quad (33)$$

with a coefficient of determination  $R_{fit}^2 = 0.83$ .

The right panel of Figure 13 shows the total energy emitted in the form of GWs,  $E_{GW}$ , at 250 ms as a function of the tidal Love number. Contrary to the peak frequency,  $E_{GW}$  does not exhibit a clear monotonic dependence on the EOS stiffness. Instead, the models cluster into two distinct subsets. Models LS and SL emit  $\sim 3 \times 10^{47}$  erg, while models BH, BB, and TS emit roughly  $2 \times 10^{47}$  erg. This separation is consistent with the morphology of the signals: the higher-energy models are precisely those in which the GW emission shows a series of pulses of moderate amplitude after the main period of enhanced emission has passed. On the contrary, the lower-energy models show a shorter phase of strong non-axisymmetric activity, which peaks rapidly before disappearing, leading to a

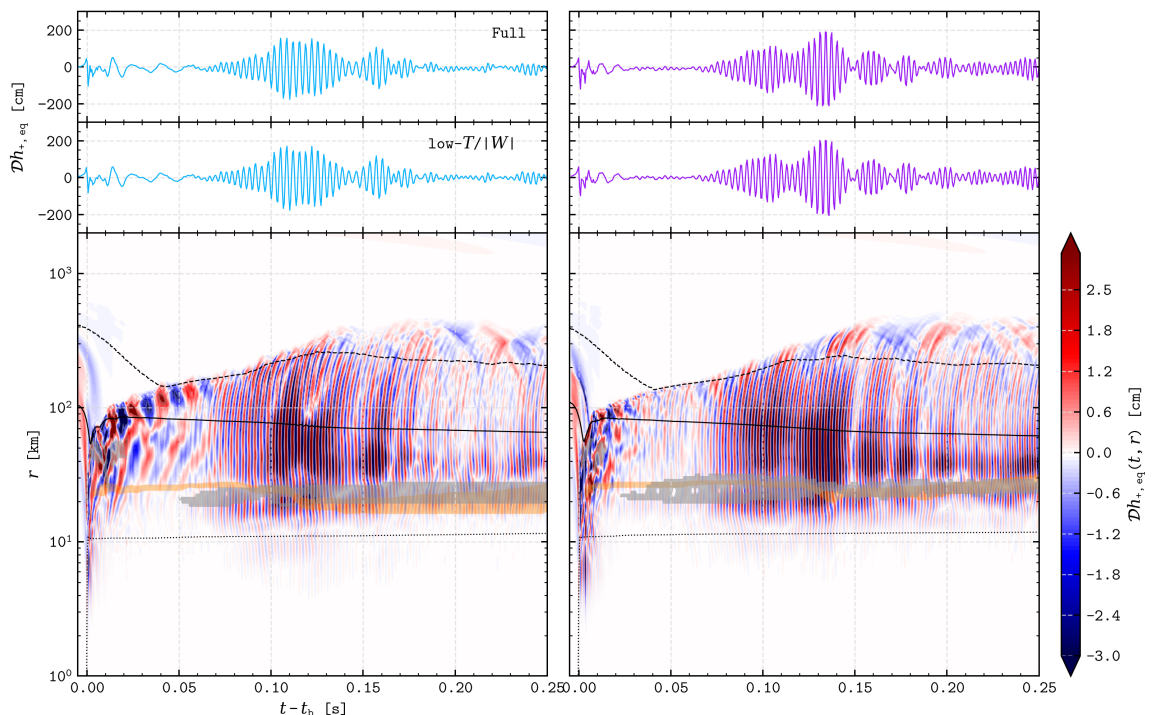


Figure 14. Evolution of the + polarization of the GW amplitude for an observer on the equatorial plane for models TS (left) and SL (right). The two upper panels show the time evolution of the GW amplitude for the entire simulation domain (top panels), and for the region between the isosurfaces of  $10^{14}$  g/cm $^3$  and  $10^9$  g/cm $^3$  (middle panels). The bottom panels show the space-time evolution of  $\mathcal{D}h_{+,eq}(r, t)$ . Solid, dashed and dotted lines have the same meaning as in the left panel of Figure 7. Gray shades mark convective regions on the equatorial plane (i.e., where  $N^2 < 0$ ) within the PNS. Orange shades indicate the corotation region. The waveforms and space-time diagrams are computed from the simulation data with a temporal resolution of 0.5 ms, which limits the resolution of frequencies to 1 kHz. As a result, discrepancies are present, particularly during the bounce and early post-bounce phases, when higher-frequency components are dominant (see Figure 11). However, since the GW emission associated with the LTWI is confined to frequencies well below 1 kHz, the decomposition remains reliable for analysing the instability-driven signal.

correspondingly smaller integrated emission (see previous discussion on the morphology of the signals). Moreover, this clustering might also reflect differences in the underlying microphysics of the EOSs. In particular, the EOSs of models SL and LS, adopt a single nucleon approximation (SNA) for heavy nuclei below nuclear saturation density, while those of models BH, BB, and TS describe matter in NSE with an ensemble of nuclei. The fluid in the region where the LTWI develops is treated with the high-density EOS, which may affect its thermodynamic structure. Therefore, the different treatment of the matter, may have an impact on the convection and the differential rotation profile, potentially leading to the observed separation between the energy carried away as GWs.

*3.6.2 Space-time evolution of the GW emitting regions* To visualize the spatial origin and temporal development of the emission, we compute the GW amplitude as a function of time and radius. We focus on the + polarization for an equatorial observer in two representative cases: model TS, where the spiral modes terminate, and model SL, where they continue with reduced strength. For this analysis, we refer to the last row of Figure 14, while the total amplitude and the contribution from the region enclosed by the  $10^{14}$  g/cm $^3$  and  $10^9$  g/cm $^3$  isosurfaces are displayed in the first and second rows, respectively.

The bounce signal, associated with the formation of the PNS, marks the onset of GW emission. During the few tens of milliseconds following the bounce signal, several modes emerge. These include prompt convection between 25 km and 60 km, driven by negative entropy and  $Y_e$  gradients, and oscillations of the innermost 10 km of the PNS. These modes correspond to the ones described for the fast-rotating model in Cusinato, Obergaulinger, and Aloy [58].

After prompt convection ceases, model TS enters a  $\sim 50$  ms phase in which the GW signal is dominated by low-frequency modes propagating from the centre toward the PNS surface (corresponding to mode (4) in [58]). In contrast, in model SL, these modes are either disrupted or strongly suppressed by the onset of PNS convection in the equatorial region (gray regions in the bottom row of Figure 14).

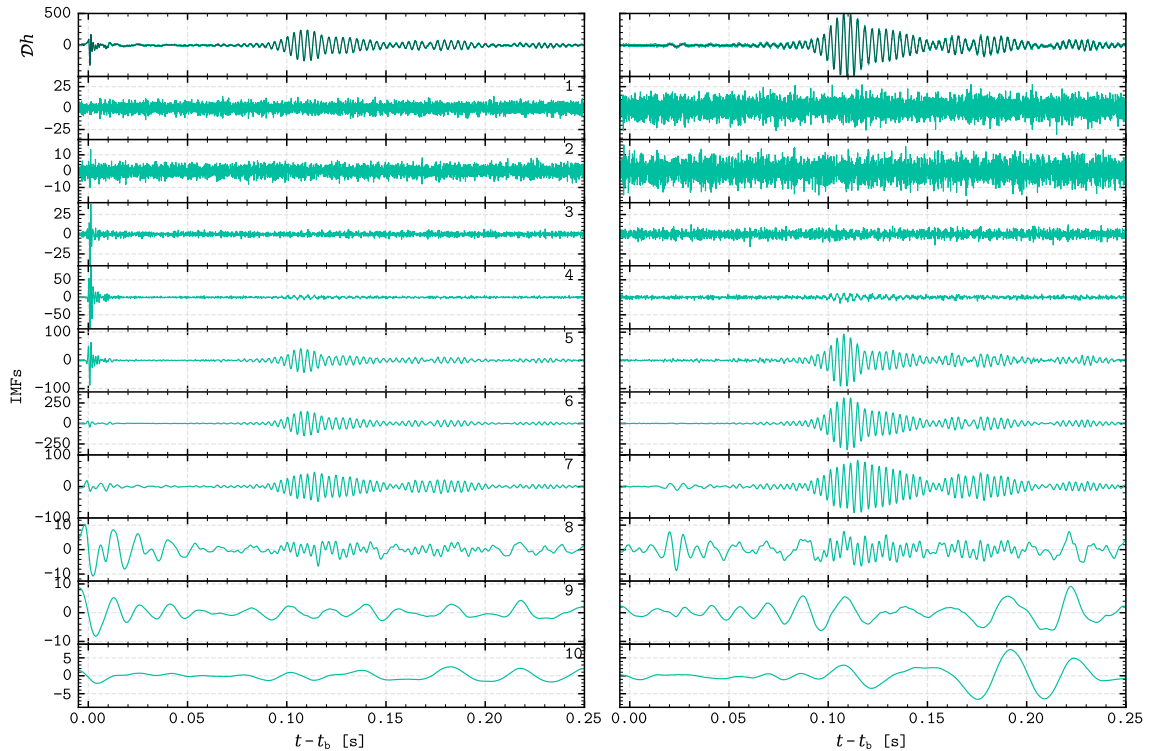


Figure 15. Time evolution of the total GW + polarization for an observer on the equatorial plane (left), and  $\times$  polarization for an observer on the polar axis and corresponding EEMD in ten IMFs for model BB. The black lines in the top row represent the original strain, the green lines the sum of the IMFs.

These convective motions excite fast oscillating modes that propagate outward and pile up at the shock, interrupting the previously dominant low-frequency component.

In both models, the LTWI begins to influence the GW signal only after PNS convection has developed. Once the corotation region (orange shading in the bottom row of Figure 14) enters the convectively unstable layer, the instability leads to a high amplification of the GW signal. The modes of the resulting signal consist of fast oscillations at  $\sim 400$  Hz originating at radii of  $\sim 20$  km, and spanning the entire PNS. These modes penetrate below the  $10^{14}$  g/cm<sup>3</sup> isodensity surface, where they are quickly damped and therefore this part contributes negligibly to the observable signal. The modes due to the LTWI also possess outward-propagating components that cross the PNS boundary, slow down, but retain much of their amplitude before eventually being partially reflected and dissipated at the shock. In model SL, the corotation region appears to enter the convective zone earlier than the actual onset of the instability; this is likely due to our approximate identification of convective regions which is based on an angle-averaged  $N^2$  over  $\theta \in [-30^\circ, 30^\circ]$ , which may overestimate the outer radial boundary of the convective layer (see Section 3.5).

Following the peak development of the instability, models TS and SL differ in their evolution. In model TS, the GW enhancement associated with the LTWI ceases, leaving only weak modes spanning the entire PNS and propagating outwards. On the other hand, in model SL, the corotation region remains fully embedded in the convective zone and similar modes to the maximum activity continue for longer and with them the enhanced emission, albeit at a reduced amplitude.

Finally, we find that most of the sub-kilohertz GWs are emitted from the region bounded by the  $10^{14}$  g/cm<sup>3</sup> and  $10^9$  g/cm<sup>3</sup> isosurfaces. The matching score defined in Equation (32) between the GW extracted from this region and the signal from the full domain yields  $\mathcal{M} \geq 0.9$  for all polarisations and observer orientations.

**3.6.3 GW EEMD decomposition** We apply the procedure described in Section 2.4 to decompose our signals into 10 IMFs. Prior to the EEMD we remove the residual, computed with a single EMD, to prevent a slow drift of the reconstructed GW amplitude toward positive values that indicates jet formation. In practice, since none of our models have exploded or formed jets during the simulated time, the residual contribution to the waveform is negligible.

Figure 15 shows the resulting IMF decomposition: the + polarization for an equatorial observer in the left panel and the  $\times$  polarization for a polar observer in the right panel. The two polarisations

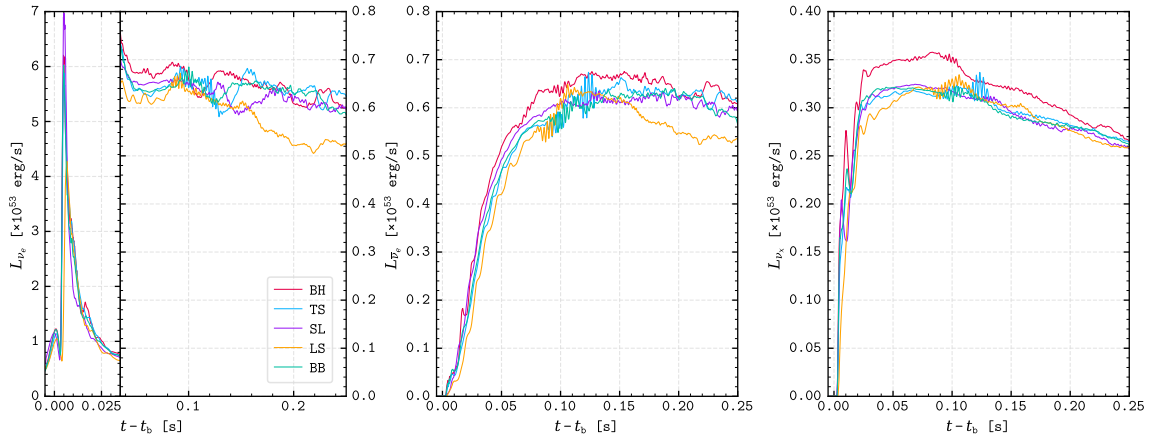


Figure 16. Time evolution of the neutrino luminosity for electron neutrinos,  $\nu_e$ , (left), electron antineutrinos,  $\bar{\nu}_e$ , (middle), and a single heavy lepton neutrino flavour,  $\nu_x$ , (right).

display qualitatively similar IMF behaviour. Specifically, IMFs 1 and 2 reflect residual components of the added white noise that were not fully averaged out by the ensemble procedure. IMFs 3 and 4 are very weak (peak  $\mathcal{D}h \leq 10$  cm) and, aside from a small contribution of the bounce signal in  $h_{+,eq}$ , they contribute negligibly to the overall strain. Similarly, IMFs 8-10 are weak ( $\mathcal{D}h \leq 10$  cm) and do not substantially affect the total signal.

IMFs 5-7 are the dominant components, with maximum amplitudes above 50 cm. By computing the matching score defined in Equation (32) between the original waveform and the reconstruction from each IMF, we find that the component associated with the LTWI is well captured by IMF 6 alone. Across the full simulation sample, for all observer directions and polarisations, IMF 6 matches the full signal generated by the LTWI at  $\mathcal{M} \geq 0.99$ , with only minor corrections when IMFs 5 and 7 are included.

### 3.7 Neutrino signal

Figure 16 shows the total neutrino luminosities extracted at 500 km for electron neutrinos ( $L_{\nu_e}$ , left panel), electron antineutrinos ( $L_{\bar{\nu}_e}$ , middle panel), and heavy-lepton neutrinos ( $L_{\nu_x}$ , right panel).

Previous studies have found that the neutronization burst shows only a moderate sensitivity to the progenitor structure and nuclear EOS [128, 129]. In contrast, our models exhibit a significant variation in the amplitude of the initial  $L_{\nu_e}$  breakout peak, spanning  $4 \times 10^{53} - 7 \times 10^{53}$  erg/s. This suggests that EOS-dependent effects may be more pronounced in our setup. These differences likely reflect variations in the PNS structure and in the location of the neutrinosphere at shock breakout, and may additionally be enhanced by multidimensional effects absent in 1D simulations (e.g., [129]).

We find that neither the effective stiffness parameter nor the  $B_1$  and  $B_2$  proxies based on cold EOS properties (see Table 1) provide a reliable predictor of the neutronization burst peak across our set of models. Nevertheless, these quantities do capture a robust limiting behaviour, as they consistently identify model LS as producing the weakest burst.

The two EOS with the smaller initial values of the Love number ( $\kappa_{[1,15]}$  models LS and BH; see Table 2) are indeed associated with the lowest breakout luminosities, while intermediate-stiffness models yield stronger emission. Stiffer EOS provide greater pressure support at a given density, leading to a less compact core at bounce. This may result in weaker shock formation and reduced compression at shock breakout, thereby producing a weaker prompt  $\nu_e$  burst.

The  $B_1$  and  $B_2$  proxies reproduce some aspects of the behaviour, correctly identifying model LS as the weakest case and placing BH, BB, and SL in the intermediate-to-high range. However, they also show clear discrepancies: in particular, they systematically overestimate the burst strength of model TS and incorrectly rank BB above SL.

Overall, this indicates that the neutronization burst peak is not primarily controlled by cold EOS properties, but instead by dynamical quantities emerging during collapse and bounce. These likely include the evolution of the electron fraction, the thermal response of the EOS at sub-saturation densities, and the detailed structure of the core at shock breakout. The fact that all indicators robustly identify model LS as producing the weakest burst likely reflects its comparatively low pressure support in these regimes, leading to a more compact core and reduced shock strength.

Most of the light curves are similar to each other, but there are a few outliers. The electron neutrino and anti-neutrino luminosities of model LS show a noticeable drop around 150 ms to a level

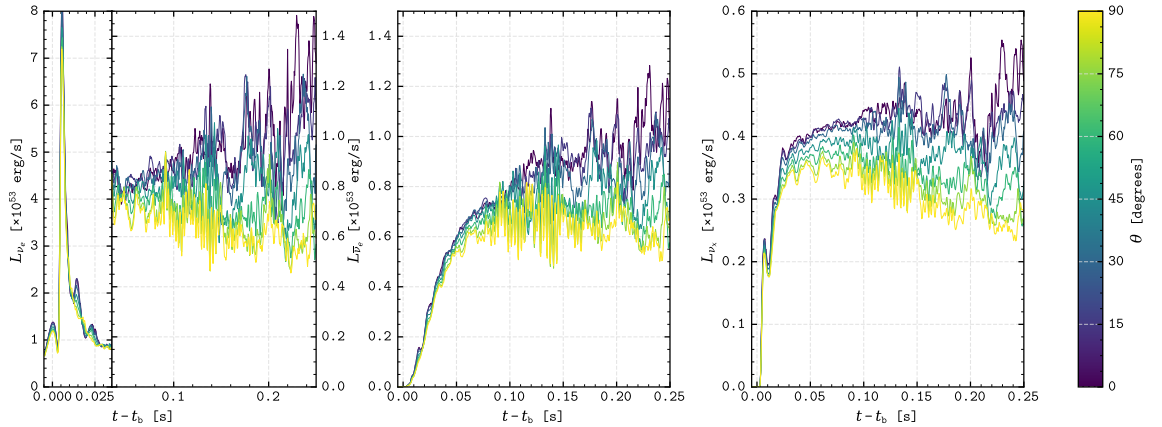


Figure 17. Time evolution of the isotropic equivalent neutrino luminosity emitted for different values of the colatitudinal angle  $\theta$  for model SL. Panels from left to right show electron neutrinos,  $\nu_e$ , electron antineutrinos,  $\bar{\nu}_e$ , and heavy lepton neutrinos,  $\nu_x$ .

about  $\sim 20\%$  lower than in the other models. This phenomenon is caused by an interplay between the EOS and the rotation. The stiffer EOS of model LS has a smaller and less massive PNS compared to the other models. Additionally, the accretion rate diminishes at  $\sim 120$  ms lowering the neutrino luminosities. The drop in the neutrino luminosities also coincides with the dissipation of the spiral structure, which eliminates a source of PNS destabilisation. The heavy-lepton neutrino luminosity ( $L_{\nu_x}$ ) for model BH dominates over the other models by  $\sim 15\%$ . This behaviour may be caused by the inclusion of the  $\Lambda$ -hyperons at high densities, which enlarge the heavy-lepton neutrinosphere. Although a larger decoupling radius would typically imply lower temperatures, in this case the temperature remains comparable to the other models, leading to an overall increase in the emitted neutrino luminosity.

Models BB, LS, and TS develop fast luminosity oscillations at around 100 ms after bounce, with a characteristic frequency of  $\sim 350$  Hz. These oscillations correspond to the onset of large-scale non-axisymmetric modes within the PNS, and they are visible in all three neutrino flavours.

Since the neutrinospheres reside within the region affected by the instability, they are expected to be perturbed once the LTWI mode sets in. However, the angle-integrated luminosities can mask the  $\phi$ -dependent variations associated with spiral modes. Therefore, to assess the angular dependence of the neutrino-signal modulation resulting from the LTWI, we compute the isotropic equivalent neutrino luminosity,

$$L_{\nu_i}^{\text{iso}}(\theta, \phi) = 4\pi r^2 F_{\nu_i}^r(r, \theta, \phi), \quad (34)$$

where  $F_{\nu_i}^r(r, \theta, \phi)$  is the radial neutrino flux and  $\nu_i$  denotes the neutrino flavour. We extract these luminosities at  $r = 500$  km for a fixed azimuth  $\phi = 0^\circ$ , while varying the polar angle  $\theta$  from  $0^\circ$  to  $90^\circ$ . In Figure 17 we compare the isotropic equivalent luminosities for model SL.

We find that although the integrated luminosity shows no clear signature of non-axisymmetric instability, the equivalent luminosities evaluated in specific directions do. In particular, viewing angles between  $75^\circ$  and  $90^\circ$  display more persistent and regular oscillations, consistent with the predominantly equatorial nature of the LTWI, while toward the poles the signal appears more intermittent and lacks clear long-lived modulation. This is a direct consequence of the LTWI, which develops on the equatorial plane, and the spiral modes lead to larger temporal fluctuations in the position and the neutrinospheres. Additionally, the neutrino luminosities are more intense at the poles than at the equator for all flavours. This reflects the rotationally induced flattening of the neutrinospheres: in the equatorial plane, the larger radius places the decoupling region at lower temperatures compared to the poles, resulting in a reduced equatorial emission.

In Figure 18 we show the spectrograms of the angle-integrated neutrino luminosity (left), the equatorial isotropic equivalent luminosity (middle), and the polar isotropic equivalent luminosity (right) for  $\bar{\nu}_e$  of model TS. The integrated luminosity exhibits a clear feature at a frequency just below 400 Hz, lasting from  $\sim 80$  ms to  $\sim 130$  ms, which matches the dominant  $(\ell, m) = (2, 2)$  mode identified in Section 3.4. The equatorial luminosity reveals this same mode, which persists for a longer duration (75 – 140 ms) as well as an additional prominent feature below 200 Hz associated with the  $(\ell, m) = (1, 1)$  mode (see Table 2). This lower-frequency contribution is likely suppressed in the integrated luminosity because its non-axisymmetric emission pattern largely cancels out under angle integration. In contrast, the polar emission shows no evidence of any LTWI-driven modulation. This

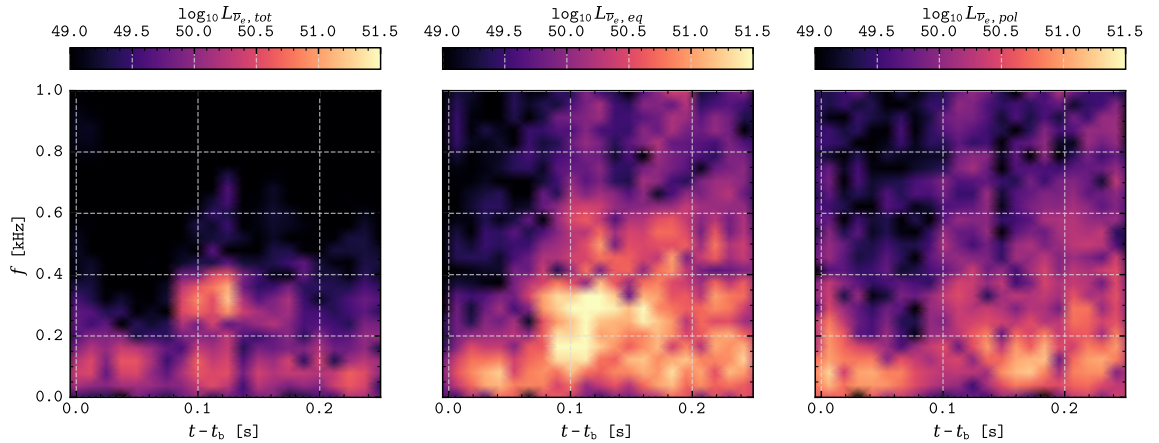


Figure 18. Spectrograms of the electron antineutrino luminosity for model TS: the total luminosity (left), the isotropic equivalent luminosity from the equator (middle), and the isotropic equivalent luminosity from the pole (right). In all spectrograms a band-pass filter in the range  $f = [50, 1000]$ Hz has been applied.

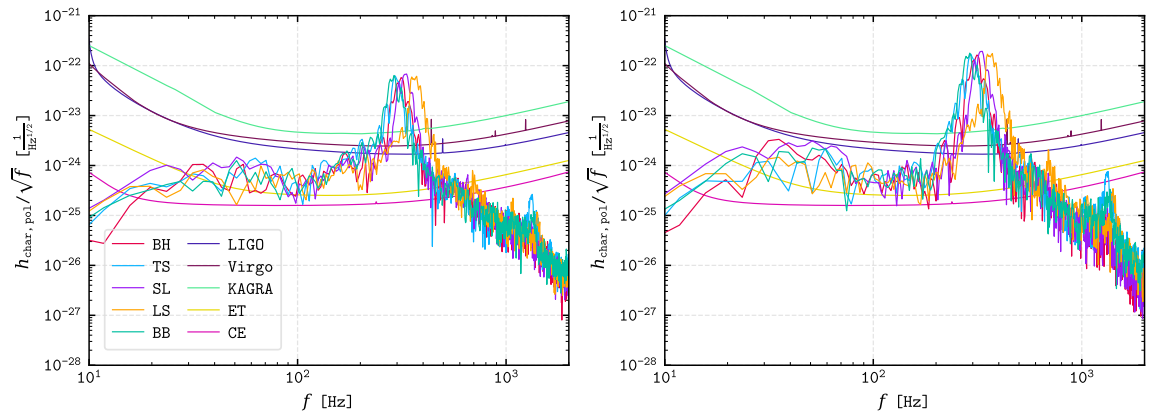


Figure 19. Characteristic GW spectra for equatorial (left panel) and polar (right) observers, assuming a source distance of 1 Mpc, compared with the design sensitivity curves of current- and next-generation interferometers.

behaviour is fully consistent with the predominantly equatorial character of the LTWI discussed in Section 3.2.2. Equivalent spectrograms for  $\nu_e$  and  $\nu_x$  and other models display the same qualitative trends (not shown).

## 4 Discussion

In this section we discuss the prospects for detecting the GWs and neutrino signals emitted by our models.

### 4.1 GWs: Prospects of detection

We assess the detectability of the GW emission by computing the characteristic strain [130] for polar and equatorial observers,

$$h_{\text{char}}(f) = 2f \sqrt{|\tilde{h}_+(f)|^2 + |\tilde{h}_\times(f)|^2}, \quad (35)$$

where  $\tilde{h}_{+/\times}(f)$  denote the Fourier transforms of the GW at a distance  $\mathcal{D}$ .

Figure 19 shows  $h_{\text{char}}/f^{1/2}$  (Equation (35)) for equatorial and polar observers, compared with the design amplitude spectral densities (ASDs) curves of the current-generation detectors, LIGO [11, 131, 132], Virgo [12, 131, 132], and KAGRA [13, 131, 132], as well as the projected ASDs of third-generation detectors such as the ET [15, 133] and CE [14, 134].

All models show a maximum emission peak around 330 Hz, which is associated with the  $(\ell, m) = (2, 2)$  mode generated by the LTWI (Table 2). This frequency lies close to the most sensitive band of both current- and next-generation detectors. The equatorial and polar spectra are broadly similar because the emission is dominated by the same non-axisymmetric instability. However, the equatorial emission is weaker since the symmetry about the equatorial plane suppresses the  $h_\times$  polarization for equatorial observers.

		BH	TS	SL	LS	BB
LIGO	pol	2.44	2.37	2.89	2.62	2.50
	eqt	0.890	0.875	1.03	0.932	0.904
Virgo	pol	1.66	1.61	1.96	1.74	1.71
	eqt	0.605	0.598	0.700	0.623	0.619
KAGRA	pol	0.862	0.848	1.00	0.863	0.905
	eqt	0.313	0.314	0.358	0.310	0.325
ET	pol	14.1	13.9	16.3	14.0	14.88
	eqt	5.13	5.17	5.85	5.03	5.35
CE	pol	22.1	21.5	26.1	23.3	22.79
	eqt	8.10	8.04	9.38	8.41	8.28

Table 3. Maximum source distance (in Mpc) at which our models achieve an optimal SNR of 8 in current- and next-generation ground based detectors.

Models TS and LS also show secondary peaks at approximately twice and three times the dominant frequency, corresponding to the excitation of higher-order spiral modes with  $(\ell, m) = (3, 3)$  and  $(\ell, m) = (4, 4)$ .

To quantify detectability, we compute the maximum distance at which each model yields a signal-to-noise-ratio (SNR) of 8, adopting the optimal matched-filter SNR. We define the SNR as in Moore, Cole, and Berry [130],

$$\varrho = \sqrt{\int_0^{+\infty} d \ln f \left( \frac{h_{\text{char}}(f)}{h_n(f)} \right)^2}, \quad (36)$$

where  $h_n(f)^2 = f \text{ASD}(f)^2$ , in which we used the ASD relative to the detector noise. The maximum distances at which each model achieves  $\varrho = 8$  for both polar and equatorial orientations are listed in Table 3.

The equatorial symmetry which suppresses the  $h_{\times}$  polarization for equatorial observers reduces the detection distance by more than a factor of two relative to the polar direction. Among our models, SL reaches the largest detection distances: 2.89 Mpc for polar observers with advanced LIGO, and up to 26.1 Mpc with CE. This is mainly due to its slightly stronger and broader dominant emission peak (Figure 19). In current detectors, all models are detectable well beyond the Milky Way for both orientations, with the most favourable (polar) line of sight reaching Andromeda [135]. In third-generation detectors, they become detectable throughout the Local Group.

The distances presented in this work exceed those reported by e.g., [136] by factors of  $\sim (3 - 5)$  (polar) and  $\sim (8 - 10)$  (equatorial). This arises from both the much higher amplitudes of our models and the more favourable location of the dominant emission peak within the optimal sensitivity band of the detectors.

#### 4.2 Neutrinos: Prospects of detection

Galactic CCSN explosions are expected to emit neutrinos which are detectable by current- and next-generation neutrino experiments. In this study, we focus on neutrino observatories that, at the time of writing, are operational, are of different types, or provide complementary detection channels. For this reason, we consider SK [16], IceCube [20, 21], JUNO [18], and Sudbury neutrino observatory with liquid scintillator (SNO+) [137].

SK and IceCube are 32.5 kt and 3.5 Mt water (or ice) Cherenkov detectors, respectively, and are primarily sensitive to electron antineutrinos via the inverse beta decay (IBD) reaction,

$$\bar{\nu}_e + p \rightarrow e^+ + n. \quad (37)$$

JUNO and SNO+ are liquid scintillator neutrino observatories consisting of spherical volumes containing 20 kt and 780 t of linear alkylbenzene, respectively. The former is most sensitive to  $\bar{\nu}_e$  via IBD, while the latter is primarily sensitive to  $\nu_e$  via charged-current interactions on carbon,

$$\nu_e + {}^{12}\text{C} \rightarrow {}^{12}\text{N} + e^-. \quad (38)$$

Since neutrino flavours may oscillate during their propagation from the collapsing star to the detector, we consider three scenarios: no flavour conversion, and adiabatic flavour conversion due to Mikheyev-Smirnov-Wolfenstein (MSW) effects assuming either the normal or inverted neutrino mass

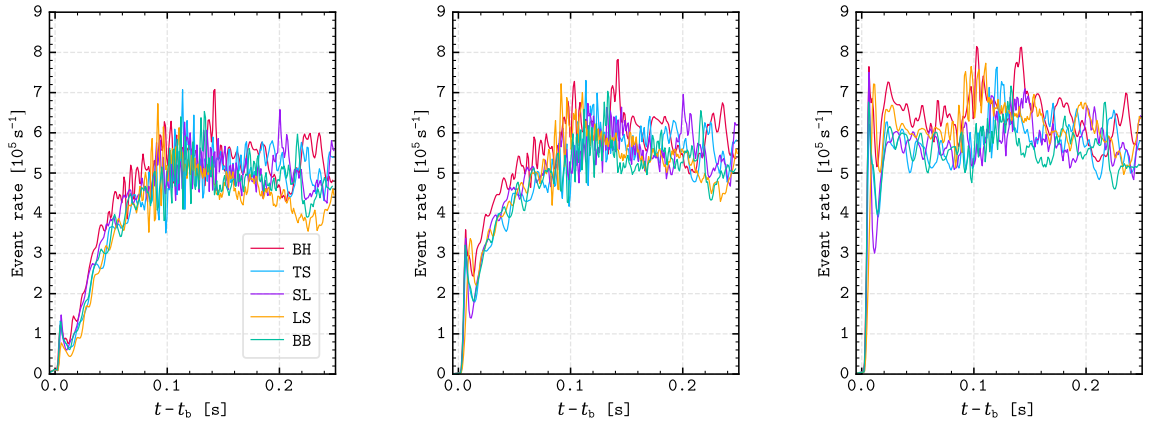


Figure 20. Neutrino event rates based on the equatorial,  $(\theta, \phi) = (\frac{\pi}{2}, 0)$ , isotropic equivalent luminosities for the main detection channel in IceCube, assuming no neutrino oscillations (left panel), adiabatic MSW with normal (middle panel) and inverted (right panel) mass order at a distance of 10 kpc.

hierarchy. The neutrino and antineutrino fluxes at Earth are given by [138]:

$$\begin{aligned}
 F_e &= p_m F_e^0 + (1 - p_m) F_x^0, \\
 \bar{F}_e &= \bar{p}_m \bar{F}_e^0 + (1 - \bar{p}_m) F_x^0, \\
 F_\mu + F_\tau &= (1 - p_m) F_e^0 + (1 + p_m) F_x^0, \\
 \bar{F}_\mu + \bar{F}_\tau &= (1 - \bar{p}_m) \bar{F}_e^0 + (1 + \bar{p}_m) F_x^0,
 \end{aligned} \tag{39}$$

where  $F^0$  and  $\bar{F}^0$  denote the neutrino and antineutrino fluxes at the source in the absence of flavour conversion, the subscript  $x$  represents a heavy-lepton neutrino species, and  $p_m$  and  $\bar{p}_m$  are the neutrino and antineutrino survival probabilities, respectively, with  $m = (n, i)$  corresponding to the normal or inverted mass hierarchy. The neutrino and antineutrino survival probabilities are given by

$$\begin{aligned}
 p_n &= \sin^2 \theta_{13}, & p_i &= \sin^2 \theta_{12} \cos^2 \theta_{13}, \\
 \bar{p}_n &= \cos^2 \theta_{12} \cos^2 \theta_{13}, & \bar{p}_i &= \sin^2 \theta_{13},
 \end{aligned} \tag{40}$$

where  $\theta_{12}$  and  $\theta_{13}$  are the neutrino mixing angles, set to  $\sin^2 \theta_{12} = 0.297$  and  $\sin^2 \theta_{13} = 0.025$  [139].

Neutrino flavour conversion is simulated using SNEWPY [140], while detector effects and event rates are simulated with SNOwGLOBES [141].

Figure 20 shows the neutrino event rates expected in IceCube at a reference distance of 10 kpc for our set of models, assuming no flavour conversion and adiabatic MSW conversion with normal and inverted mass ordering (left, middle, and right panels, respectively). For all oscillation scenarios, the predicted event rates are of order  $\sim 5 \times 10^5$  events/s, consistent with the findings of [142]. The overall event rate depends on the assumed flavour-conversion model, with the inverted-hierarchy MSW case showing a more sustained, constant event rate immediately following the bounce compared to the other models.

Importantly, the rapid oscillations observed in the equatorial neutrino luminosity (Figure 17) persist across all flavour conversion models in the detected event rates. The modulation associated with the spiral mode survives the flavour-conversion and detector-response pipeline in the ideal event-rate signal. At Galactic distances, the predicted event rates are sufficiently high that such a modulation could be observable, depending on its fractional amplitude and on the adopted time binning. However, the maximum distance at which the modulation itself can be identified is expected to be smaller than the distance at which the burst can be detected, and requires a dedicated statistical analysis including Poisson fluctuations and detector backgrounds. Assuming that of order  $10^3$  detected events are required to identify the high-frequency modulation, the corresponding distance scale is  $\sim 10^2$  kpc for the event rates considered here, rather than the larger distance at which the overall burst may still be detectable.

The time-frequency maps of the equatorial neutrino event rates for model TS, in Figure 21 further confirm the imprints of the LTWI. All the assumed flavour-conversion scenarios show clear imprints of the spiral modes at frequencies just below 200 Hz and 400 Hz (see Table 2) persisting from approximately 75 ms to 140 ms. The dominant features in the event-rate spectrograms are consistent

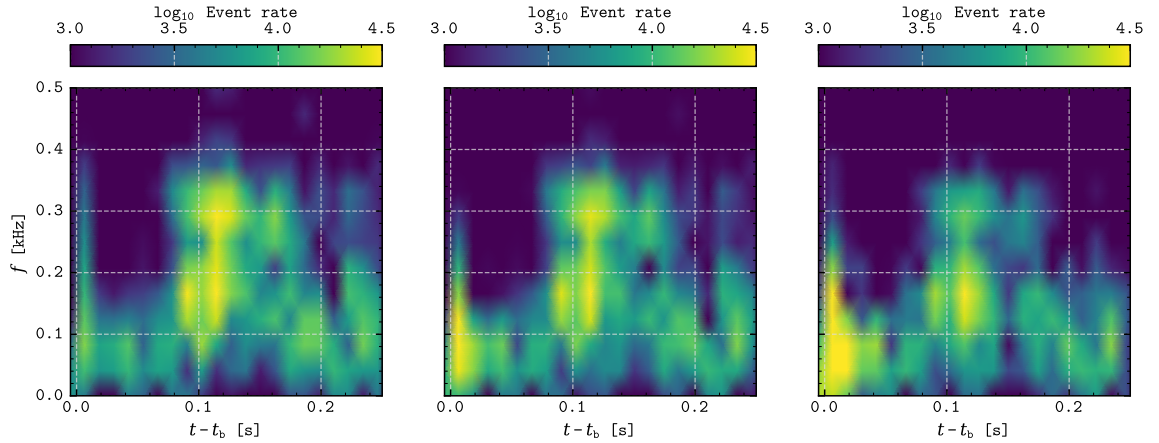


Figure 21. Spectrograms of the neutrino event rate of the equatorial neutrino luminosities for model **TS** simulated in the main detection channel in IceCube, assuming no neutrino oscillations (left panel), adiabatic MSW with normal (middle panel) and inverted (right panel) mass order at a distance of 10 kpc. The neutrino event rate has a non-zero mean causing an excess of power in the low frequencies, therefore in all spectrograms a high-pass filter at  $f = 50$  Hz has been applied.

with the LTWI modulation shown in Figure 18, demonstrating a potentially robust multimessenger correlation for the LTWI. While flavour conversion affects the overall event-rate normalisation, the characteristic frequencies and temporal evolution of the instability-induced modulations are largely insensitive to the oscillation model.

Finally, we quantify the detectability distances for polar, equatorial, and angle-averaged neutrino emission assuming no flavour conversion and adiabatic MSW conversion with normal and inverted mass ordering. We define the detectability distance as the maximum distance at which at least 25 neutrino events are expected over the 250 ms duration of the simulations. This choice is historically motivated, as it corresponds to the order of magnitude of the total number of neutrinos detected from SN 1987A, and is adopted here as a common benchmark to facilitate a direct comparison between detectors, emission geometries, and flavour-conversion scenarios, rather than as a formal detection-significance criterion. Additionally, we note that more sophisticated detectability criteria which take into account time-dependent backgrounds, will lower the detectability estimates. Therefore, the resulting distances for IceCube, SK, JUNO, and SNO+ summarised in Table 4 should be regarded as optimistic upper limits. IceCube achieves the largest detection distances, reaching  $\sim 700 - 800$  kpc, due to its large instrumented volume. SK and JUNO, which have comparable target masses and are both dominated by the IBD channel, yield similar detection distances of approximately 80 kpc. SNO+, with its smaller mass and primary sensitivity to  $\nu_e$ , reaches maximum distances of order  $\sim 15$  kpc. Among our models, BH and LS show the largest and smallest detectability distances, respectively, consistent with their higher and lower neutrino luminosities and mean energies. As already noted in Section 3.7, polar emission yields larger detection distances than equatorial and average emission for all detectors. The detection horizon is also affected by the assumed flavour-conversion scenario: SK and JUNO are most favourable in the absence of oscillations, whereas IceCube and SNO+ achieve larger distances for adiabatic MSW conversion with inverted mass ordering, reflecting the different flavour sensitivities of the detectors.

We compare the detection distances for GWs and neutrino emission (Tables 3 and 4). For neutrinos, we adopt the distances obtained for SK, as its detection is dominated by resolved inverse beta decay events, providing a relatively direct link between the detected counts and the underlying neutrino flux. For GWs, we consider the sensitivity of a single Advanced LIGO detector representative of the current generation. We find that the GW signal is detectable at distances  $\sim 8$  to  $\sim 30$  times larger than those for neutrinos, depending on the viewing angle. In contrast, the neutrino signal remains effectively limited to distances comparable to that of SN 1987A. This highlights the broader reach of GWs for probing rapidly rotating CCSN events, despite their stronger dependence on source orientation.

#### 4.3 Influence of the EOS on the detection distance

The nuclear EOS introduces only modest variations (of order  $\sim 5\%$ ) in the overall neutrino detectability horizon, even though it affects several quantities that determine the detailed properties of the signal.

Among the models, the total emitted neutrino energy varies only moderately,  $E_\nu \simeq (5.9 - 6.6) \times$

			BH	TS	SL	LS	BB
IceCube	avg	No	724	692	704	670	687
		MSW NMO	784	740	751	739	735
		MSW IMO	844	790	797	812	786
	eqt	No	677	653	658	625	642
		MSW NMO	734	701	705	670	690
		MSW IMO	793	751	751	777	741
	pol	No	821	768	775	742	771
		MSW NMO	883	817	823	812	820
		MSW IMO	944	866	868	885	869
JUNO	avg	No	83	80	80	77	79
		MSW NMO	82	78	79	77	78
		MSW IMO	77	73	74	74	73
	eqt	No	78	76	75	73	74
		MSW NMO	77	74	74	73	73
		MSW IMO	73	70	69	70	69
	pol	No	93	88	88	84	88
		MSW NMO	92	86	86	81	86
		MSW IMO	86	80	80	80	81
SK	avg	No	86	83	84	80	82
		MSW NMO	85	72	82	80	81
		MSW IMO	81	77	77	77	76
	eqt	No	81	79	78	75	77
		MSW NMO	80	77	77	76	76
		MSW IMO	76	73	72	74	72
	pol	No	97	92	92	88	92
		MSW NMO	96	90	90	88	90
		MSW IMO	90	84	84	84	84
SNO+	avg	No	16	16	16	15	15
		MSW NMO	16	15	15	15	14
		MSW IMO	15	14	15	15	15
	eqt	No	15	15	15	14	14
		MSW NMO	15	15	15	14	14
		MSW IMO	14	14	14	14	14
	pol	No	18	17	17	17	17
		MSW NMO	18	17	17	17	17
		MSW IMO	17	16	16	16	16

Table 4. Maximum distance (in kpc) at which our models yield 25 neutrino detections in the first 250 ms for current neutrino experiments and no neutrino flavour oscillations, adiabatic MSW with normal (NMO) and inverted (IMO) mass order.

$10^{52}$  erg, which corresponds to a spread of about  $\Delta E_\nu/E_\nu \sim 10\%$ . Since the number of detected events scales approximately as  $N_{\text{det}} \propto E_\nu/(4\pi D^2)$ , the maximum detection distance behaves as  $D_{\text{max}} \propto \sqrt{E_\nu}$ .

$$\frac{\Delta D_{\text{max}}}{D_{\text{max}}} \simeq \frac{1}{2} \frac{\Delta E_\nu}{E_\nu} \sim 5\%. \quad (41)$$

Hence, differences among the considered EOSs affect the detection distance only at the few-percent level.

The different EOSs influence the PNS structure, in particular its radius at early times, which in turn modifies the location and temperature of the neutrinosphere. In our models the PNS radius varies in the range  $R_{\text{PNS}} \sim 59 - 66$  km. Because the detection cross section of the dominant IBD channel scales approximately as  $\sigma_{\text{IBD}} \propto E_\nu^2$  [143, 144], even modest changes in the mean neutrino energy can produce noticeable variations in the event rate. Thus EOS-dependent differences in the PNS compactness may translate into small but measurable differences in the detected neutrino signal.

The LTWI produces time-dependent modulations in the neutrino emission. The characteristic frequency of this variability is set by the spiral mode frequency,  $f_{\text{LTWI}} \sim 150 - 180$  Hz, which corresponds to millisecond-scale luminosity variations. The amplitude of these modulations is typically only a few percent of the total luminosity, so their detectability depends critically on the event statistics of the detector. Large-volume detectors such as IceCube are particularly sensitive to such high-frequency variations because their enormous effective detection volume provides very high counting statistics and millisecond time resolution [20, 145].

Finally, the EOS affects the duration of the LTWI phase. In the models analysed here the instability lasts between  $\sim 40$  and  $\sim 170$  ms depending on the EOS. For a characteristic frequency  $f_{\text{LTWI}} \sim 170$  Hz, this corresponds to a number of oscillation cycles  $N_{\text{cycles}} \simeq f_{\text{LTWI}} \Delta t \sim 7 - 30$ . A longer-lasting instability therefore increases the likelihood that periodic modulations could be

extracted from the neutrino signal. In summary, while the EOS has only a modest impact on the overall neutrino detection horizon, it influences several aspects of the signal, including the neutrinosphere temperature, the average neutrino energy, and the amplitude and duration of the LTWI-driven variability, which may provide additional diagnostics of the dense-matter physics in a nearby CCSN.

## 5 Conclusion

We presented the first 250 ms of evolution from five rapidly rotating CCSN simulations based on the same  $35 M_{\odot}$  Wolf-Rayet progenitor, adopting identical initial magnetic-field and rotational configurations while varying the high-density EOS. The selected EOSs, namely BBSk3, BHBA $\phi$ , LS220, SLy4, and TSO, span a broad range of stiffness, correlated in this paper to the value of the tidal Love number, symmetry-energy slopes, and maximum neutron-star masses, and include both RMF and Skyrme-based descriptions of dense matter. All EOSs, except LS220, are consistent with current astrophysical and experimental constraints, while LS220 enables direct comparison with a large body of previous CCSN studies. The goal of this work was to investigate the impact of the nuclear EOS on the development of non-axisymmetric instabilities during the early post-bounce phase, and on their associated multimessenger emission.

Our analysis shows that the high-density EOS already affects the dynamics prior to core bounce, significantly modifying the stratification and rotational structure of the inner core. In particular, the EOS alters both the rotational profile and the amount of differential rotational energy available at bounce, thereby influencing the initial conditions for the post-bounce evolution and the LTWI growth.

Despite these EOS-dependent differences, all models retain sufficient differential rotation and develop overlapping corotation and convectively unstable regions inside the PNS, conditions that favour the onset of the LTWI. Unlike previous studies of the instability [70, 71, 72], our simulations also include weak magnetic fields, whose strength is not sufficient to suppress the development of LTWI. In all models, the LTWI develops through the growth of large-scale non-axisymmetric spiral structures, dominated by low-order azimuthal modes ( $m = 1, 2$ ) in the equatorial plane, and generates quasi-periodic modulations in both GWs and neutrino emission lasting for approximately 100 ms. The characteristic GW and neutrino frequencies remain quasi-constant during the active phase of the instability, with typical values of  $\sim 330$  Hz and  $\sim 170$  Hz, respectively. These frequencies lie above the typical SASI range ( $\lesssim 100$  Hz) and below the dominant PNS oscillation frequencies ( $\gtrsim 500$  Hz), placing the LTWI in a comparatively distinct region of the multimessenger spectrum. In contrast to previous studies [70, 71, 72], we do not observe a clear phase of increasing mode frequency during the activity of the instability.

We find that the peak frequency of the GW emission associated with the LTWI correlates approximately linearly with the stiffness of the nuclear EOS as measured by  $\kappa_2$ , with stiffer EOSs producing higher frequencies. This trend likely arises because the EOS modifies the compactness and rotational structure of the PNS, thus affecting the characteristic pattern frequency of the spiral modes. These results suggest that future GW observations of rapidly rotating CCSNe may provide direct constraints on the properties of dense matter. At the same time, a broader exploration of progenitor rotation rates will be necessary to disentangle EOS effects from possible degeneracies with the rotational configuration of the collapsing core.

In addition, we find that the GW component associated with the instability can be effectively isolated through the EEMD decomposition of the strain signal. Together with the results of Cusinato, Obergaulinger, and Aloy [58], this further supports the usefulness of EEMD techniques for associating specific frequency components of the GW signal with their underlying emission regions.

Finally, we find that the nuclear EOS also affects the amplitude of the neutrino breakout burst, while the onset of the LTWI induces characteristic quasi-periodic modulations in the neutrino luminosities. These signatures primarily originate from neutrinos emitted near the equatorial region and exhibit distinct frequency components associated with the dominant non-axisymmetric modes. Corresponding features are also visible in the simulated event rates of next-generation neutrino detectors, highlighting the intrinsically multimessenger nature of the instability and the possibility of jointly probing its dynamics through GW and neutrino observations.

Overall, our results indicate that the LTWI is a robust feature of rapidly rotating CCSNe across a broad range of nuclear EOSs, while its characteristic multimessenger signatures retain measurable sensitivity to the properties of dense matter. Future work extending this analysis to a broader range of progenitors, rotation rates, magnetic-field strengths, and longer post-bounce evolution times will be necessary to assess the generality of these trends and their detectability with current- and next-generation multimessenger observatories. In particular, this study considered only a single

rapidly rotating Wolf-Rayet progenitor, limiting our ability to explore how progenitor properties such as initial mass, metallicity, compactness, and angular-momentum distribution affect the development of the LTWI and its multimessenger signatures. Extending the analysis to a wider set of progenitors and to a larger sample of nuclear EOSs will therefore be crucial to probe the robustness of the trends identified here.

Additionally, although our simulations include magnetic fields, the adopted pre-collapse configuration remains dynamically weak. Stronger magnetic-field configurations may substantially modify the rotational structure of the PNS and the growth of non-axisymmetric instabilities. Exploring the interplay between magnetic stresses, differential rotation, and the LTWI therefore represents an important direction for future investigations.

Finally, numerical resolution is known to affect the post-bounce dynamics of CCSNe, including turbulence, shock evolution, and explosion properties [146, 147, 148]. Higher-resolution simulations will then be required to assess the quantitative robustness of the instability growth, amplitude, and associated multimessenger emission reported in this work.

### Acknowledgments

We thank the organisers and participants of *SN 2025gw: First IGWN Symposium on Core Collapse Supernova Gravitational Wave Theory and Detection* held in Warsaw in July 2025 for inspiring discussions on the subject. MAA thanks the Yukawa Institute for Theoretical Physics at Kyoto University. Discussions during the YITP long-term workshop YITP-T-26-02 on "Multi-Messenger Astrophysics in the Dynamic Universe" were useful to complete this work.

### Funding

We acknowledge support from grants PID2021-127495NB-I00 and PID2025-171322NB-C22 funded by MCIN/AEI/10.13039/501100011033 and the European Union, as well as from the Astrophysics and High Energy Physics programme of the Generalitat Valenciana (ASFAE/2022/026), funded by MCIN and the European Union NextGenerationEU (PRTR-C17.I1), and from the Prometeo excellence programme grant CIPROM/2022/13 funded by the Generalitat Valenciana. MC acknowledges the support through the Generalitat Valenciana via the grant CIDEAGENT/2019/031. The computations have been performed on servers Lluïsvives and Tirant-4 (grant AECT-2025-2-0002) of the Servei d'Informàtica de la Universitat de València and on the Red Española de Supercomputación (RES) on MareNostrum (grants AECT-2025-1-0012 and AECT-2025-2-0006). MAA acknowledges partial funding of the YITP for attending the long-term workshop YITP-T-26-02.

### Data availability

The data are available upon reasonable request to the authors.

### References

- [1] Adam Burrows. "Supernova Neutrinos". In: *ApJ* 334 (Nov. 1988), p. 891. DOI: [10.1086/166885](https://doi.org/10.1086/166885).
- [2] Takami Kuroda, Kei Kotake, and Tomoya Takiwaki. "A New Gravitational-wave Signature from Standing Accretion Shock Instability in Supernovae". In: *ApJ* 829.1, L14 (Sept. 2016), p. L14. DOI: [10.3847/2041-8205/829/1/L14](https://doi.org/10.3847/2041-8205/829/1/L14). arXiv: [1605.09215](https://arxiv.org/abs/1605.09215) [[astro-ph.HE](https://arxiv.org/abs/1605.09215)].
- [3] Sherwood Richers, Christian D. Ott, Ernazar Abdikamalov, Evan O'Connor, and Chris Sullivan. "Equation of state effects on gravitational waves from rotating core collapse". In: *Phys. Rev. D* 95.6, 063019 (Mar. 2017), p. 063019. DOI: [10.1103/PhysRevD.95.063019](https://doi.org/10.1103/PhysRevD.95.063019). arXiv: [1701.02752](https://arxiv.org/abs/1701.02752) [[astro-ph.HE](https://arxiv.org/abs/1701.02752)].
- [4] Oliver Eggenberger Andersen, Shuai Zha, André da Silva Schneider, Aurore Betranhandy, Sean M. Couch, and Evan P. O'Connor. "Equation-of-state Dependence of Gravitational Waves in Core-collapse Supernovae". In: *ApJ* 923.2, 201 (Dec. 2021), p. 201. DOI: [10.3847/1538-4357/ac294c](https://doi.org/10.3847/1538-4357/ac294c). arXiv: [2106.09734](https://arxiv.org/abs/2106.09734) [[astro-ph.HE](https://arxiv.org/abs/2106.09734)].
- [5] R. Daniel Murphy, Alejandro Casallas-Lagos, Anthony Mezzacappa, Michele Zanolin, Ryan E. Landfield, Eric J. Lentz, Pedro Marronetti, Javier M. Antelis, and Claudia Moreno. "Dependence of the reconstructed core-collapse supernova gravitational wave high-frequency feature on the nuclear equation of state in real interferometric data". In: *Phys. Rev. D* 110.8, 083006 (Oct. 2024), p. 083006. DOI: [10.1103/PhysRevD.110.083006](https://doi.org/10.1103/PhysRevD.110.083006). arXiv: [2406.01784](https://arxiv.org/abs/2406.01784) [[astro-ph.HE](https://arxiv.org/abs/2406.01784)].
- [6] Alexei V. Filippenko. "Optical Spectra of Supernovae". In: *ARA&A* 35 (Jan. 1997), pp. 309–355. DOI: [10.1146/annurev.astro.35.1.309](https://doi.org/10.1146/annurev.astro.35.1.309).

- [7] Stephen J. Smartt. “Progenitors of Core-Collapse Supernovae”. In: *ARA&A* 47.1 (Sept. 2009), pp. 63–106. DOI: [10.1146/annurev-astro-082708-101737](https://doi.org/10.1146/annurev-astro-082708-101737). arXiv: [0908.0700](https://arxiv.org/abs/0908.0700) [[astro-ph.SR](#)].
- [8] Avishay Gal-Yam. “Observational and Physical Classification of Supernovae”. In: *Handbook of Supernovae*. Ed. by Athem W. Alsabti and Paul Murdin. 2017, p. 195. DOI: [10.1007/978-3-319-21846-5\\_35](https://doi.org/10.1007/978-3-319-21846-5_35).
- [9] Jacco Vink. “Supernova remnants: the X-ray perspective”. In: *A&A Rev.* 20, 49 (Dec. 2012), p. 49. DOI: [10.1007/s00159-011-0049-1](https://doi.org/10.1007/s00159-011-0049-1). arXiv: [1112.0576](https://arxiv.org/abs/1112.0576) [[astro-ph.HE](#)].
- [10] S. Orlando et al. “Tracing the ejecta structure of supernova 1987A: Insights and diagnostics from 3D magnetohydrodynamic simulations”. In: *A&A* 699, A305 (July 2025), A305. DOI: [10.1051/0004-6361/202554862](https://doi.org/10.1051/0004-6361/202554862). arXiv: [2504.19896](https://arxiv.org/abs/2504.19896) [[astro-ph.HE](#)].
- [11] LIGO Scientific Collaboration et al. “Advanced LIGO”. In: *Classical and Quantum Gravity* 32.7, 074001 (Apr. 2015), p. 074001. DOI: [10.1088/0264-9381/32/7/074001](https://doi.org/10.1088/0264-9381/32/7/074001). arXiv: [1411.4547](https://arxiv.org/abs/1411.4547) [[gr-qc](#)].
- [12] F Acernese et al. “Advanced Virgo: a second-generation interferometric gravitational wave detector”. In: *Classical and Quantum Gravity* 32.2 (Dec. 2014), p. 024001. DOI: [10.1088/0264-9381/32/2/024001](https://doi.org/10.1088/0264-9381/32/2/024001). URL: <https://dx.doi.org/10.1088/0264-9381/32/2/024001>.
- [13] T. Akutsu et al. “KAGRA: 2.5 generation interferometric gravitational wave detector”. In: *Nature Astronomy* 2019 3:1 3 (1 Jan. 2019), pp. 35–40. ISSN: 2397-3366. DOI: [10.1038/s41550-018-0658-y](https://doi.org/10.1038/s41550-018-0658-y). URL: <https://www.nature.com/articles/s41550-018-0658-y>.
- [14] Varun Srivastava, Derek Davis, Kevin Kuns, Philippe Landry, Stefan Ballmer, Matthew Evans, Evan D. Hall, Jocelyn Read, and B. S. Sathyaprakash. “Science-driven Tunable Design of Cosmic Explorer Detectors”. In: *ApJ* 931.1, 22 (May 2022), p. 22. DOI: [10.3847/1538-4357/ac5f04](https://doi.org/10.3847/1538-4357/ac5f04). arXiv: [2201.10668](https://arxiv.org/abs/2201.10668) [[gr-qc](#)].
- [15] S. Hild et al. “Sensitivity studies for third-generation gravitational wave observatories”. In: *Classical and Quantum Gravity* 28.9, 094013 (May 2011), p. 094013. DOI: [10.1088/0264-9381/28/9/094013](https://doi.org/10.1088/0264-9381/28/9/094013). arXiv: [1012.0908](https://arxiv.org/abs/1012.0908) [[gr-qc](#)].
- [16] K. Abe et al. “Real-time supernova neutrino burst monitor at Super-Kamiokande”. In: *Astroparticle Physics* 81 (Aug. 2016), pp. 39–48. DOI: [10.1016/j.astropartphys.2016.04.003](https://doi.org/10.1016/j.astropartphys.2016.04.003). arXiv: [1601.04778](https://arxiv.org/abs/1601.04778) [[astro-ph.HE](#)].
- [17] Thomas Dealtry. “Hyper-Kamiokande”. In: *arXiv e-prints*, arXiv:1904.10206 (Apr. 2019), arXiv:1904.10206. DOI: [10.48550/arXiv.1904.10206](https://doi.org/10.48550/arXiv.1904.10206). arXiv: [1904.10206](https://arxiv.org/abs/1904.10206) [[hep-ex](#)].
- [18] Fengpeng An et al. “Neutrino physics with JUNO”. In: *Journal of Physics G Nuclear Physics* 43.3, 030401 (Mar. 2016), p. 030401. DOI: [10.1088/0954-3899/43/3/030401](https://doi.org/10.1088/0954-3899/43/3/030401). arXiv: [1507.05613](https://arxiv.org/abs/1507.05613) [[physics.ins-det](#)].
- [19] B. Abi et al. “Deep Underground Neutrino Experiment (DUNE), Far Detector Technical Design Report, Volume II: DUNE Physics”. In: *arXiv e-prints*, arXiv:2002.03005 (Feb. 2020), arXiv:2002.03005. DOI: [10.48550/arXiv.2002.03005](https://doi.org/10.48550/arXiv.2002.03005). arXiv: [2002.03005](https://arxiv.org/abs/2002.03005) [[hep-ex](#)].
- [20] R. Abbasi et al. “IceCube sensitivity for low-energy neutrinos from nearby supernovae”. In: *A&A* 535, A109 (Nov. 2011), A109. DOI: [10.1051/0004-6361/201117810](https://doi.org/10.1051/0004-6361/201117810). arXiv: [1108.0171](https://arxiv.org/abs/1108.0171) [[astro-ph.HE](#)].
- [21] Lutz Köpke and IceCube Collaboration. “Supernova Neutrino Detection with IceCube”. In: *Journal of Physics Conference Series*. Vol. 309. Journal of Physics Conference Series. IOP, Aug. 2011, 012029, p. 012029. DOI: [10.1088/1742-6596/309/1/012029](https://doi.org/10.1088/1742-6596/309/1/012029). arXiv: [1106.6225](https://arxiv.org/abs/1106.6225) [[astro-ph.HE](#)].
- [22] KM3NeT Collaboration. “Letter of intent for KM3NeT 2.0”. In: *Journal of Physics G Nuclear Physics* 43.8, 084001 (Aug. 2016), p. 084001. DOI: [10.1088/0954-3899/43/8/084001](https://doi.org/10.1088/0954-3899/43/8/084001). arXiv: [1601.07459](https://arxiv.org/abs/1601.07459) [[astro-ph.IM](#)].
- [23] R. M. Bionta et al. “Observation of a neutrino burst in coincidence with supernova 1987A in the Large Magellanic Cloud”. In: *Phys. Rev. Lett.* 58.14 (Apr. 1987), pp. 1494–1496. DOI: [10.1103/PhysRevLett.58.1494](https://doi.org/10.1103/PhysRevLett.58.1494).
- [24] K. Hirata et al. “Observation of a neutrino burst from the supernova SN1987A”. In: *Phys. Rev. Lett.* 58.14 (Apr. 1987), pp. 1490–1493. DOI: [10.1103/PhysRevLett.58.1490](https://doi.org/10.1103/PhysRevLett.58.1490).

- [25] E. N. Alexeyev, L. N. Alexeyeva, I. V. Krivosheina, and V. I. Volchenko. “Detection of the neutrino signal from SN 1987A in the LMC using the INR Baksan underground scintillation telescope”. In: *Physics Letters B* 205.2-3 (Apr. 1988), pp. 209–214. DOI: [10.1016/0370-2693\(88\)91651-6](https://doi.org/10.1016/0370-2693(88)91651-6).
- [26] Yudai Suwa, Akira Harada, Masayuki Harada, Yusuke Koshio, Masamitsu Mori, Fumi Nakanishi, Ken’ichiro Nakazato, Kohsuke Sumiyoshi, and Roger A. Wendell. “Observing Supernova Neutrino Light Curves with Super-Kamiokande. III. Extraction of Mass and Radius of Neutron Stars from Synthetic Data”. In: *ApJ* 934.1, 15 (July 2022), p. 15. DOI: [10.3847/1538-4357/ac795e](https://doi.org/10.3847/1538-4357/ac795e). arXiv: [2204.08363](https://arxiv.org/abs/2204.08363) [[astro-ph.HE](#)].
- [27] Hans-Thomas Janka. “Neutrino Emission from Supernovae”. In: *Handbook of Supernovae*. Ed. by Athem W. Alsabti and Paul Murdin. 2017, p. 1575. DOI: [10.1007/978-3-319-21846-5\\_4](https://doi.org/10.1007/978-3-319-21846-5_4).
- [28] Bernhard Müller. “Hydrodynamics of core-collapse supernovae and their progenitors”. In: *Living Reviews in Computational Astrophysics* 6.1, 3 (June 2020), p. 3. DOI: [10.1007/s41115-020-0008-5](https://doi.org/10.1007/s41115-020-0008-5). arXiv: [2006.05083](https://arxiv.org/abs/2006.05083) [[astro-ph.SR](#)].
- [29] A. Burrows and D. Vartanyan. “Core-collapse supernova explosion theory”. In: *Nature* 589.7840 (Jan. 2021), pp. 29–39. DOI: [10.1038/s41586-020-03059-w](https://doi.org/10.1038/s41586-020-03059-w). arXiv: [2009.14157](https://arxiv.org/abs/2009.14157) [[astro-ph.SR](#)].
- [30] Shoichi Yamada, Hiroki Nagakura, Ryuichiro Akaho, Akira Harada, Shun Furusawa, Wakana Iwakami, Hirotada Okawa, Hideo Matsufuru, and Kohsuke Sumiyoshi. “Physical mechanism of core-collapse supernovae that neutrinos drive”. In: *Proceedings of the Japan Academy, Series B* 100.3 (Mar. 2024), pp. 190–233. DOI: [10.2183/pjab.100.015](https://doi.org/10.2183/pjab.100.015).
- [31] J. R. Wilson. “Supernovae and Postcollapse Behavior”. In: *Numerical Astrophysics*. Ed. by J. M. Centrella, J. M. LeBlanc, and R. L. Bowers. Boston: Jones and Bartlett, 1982, pp. 422–434.
- [32] H. A. Bethe and J. R. Wilson. “Revival of a stalled supernova shock by neutrino heating”. In: *ApJ* 295 (Aug. 1985), pp. 14–23. DOI: [10.1086/163343](https://doi.org/10.1086/163343).
- [33] Hans-Thomas Janka. “Explosion Mechanisms of Core-Collapse Supernovae”. In: *Annual Review of Nuclear and Particle Science* 62.1 (Nov. 2012), pp. 407–451. DOI: [10.1146/annurev-nucl-102711-094901](https://doi.org/10.1146/annurev-nucl-102711-094901). arXiv: [1206.2503](https://arxiv.org/abs/1206.2503) [[astro-ph.SR](#)].
- [34] Hidetomo Sawai and Shoichi Yamada. “The Evolution and Impacts of Magnetorotational Instability in Magnetized Core-collapse Supernovae”. In: *ApJ* 817.2, 153 (Feb. 2016), p. 153. DOI: [10.3847/0004-637X/817/2/153](https://doi.org/10.3847/0004-637X/817/2/153). arXiv: [1504.03035](https://arxiv.org/abs/1504.03035) [[astro-ph.HE](#)].
- [35] Philipp Mösta, Sherwood Richers, Christian D. Ott, Roland Haas, Anthony L. Piro, Kristen Boydston, Ernazar Abdikamalov, Christian Reisswig, and Erik Schnetter. “Magnetorotational Core-collapse Supernovae in Three Dimensions”. In: *ApJ* 785.2, L29 (Apr. 2014), p. L29. DOI: [10.1088/2041-8205/785/2/L29](https://doi.org/10.1088/2041-8205/785/2/L29). arXiv: [1403.1230](https://arxiv.org/abs/1403.1230) [[astro-ph.HE](#)].
- [36] M. Obergaulinger and M. Á. Aloy. “Magnetorotational core collapse of possible gamma-ray burst progenitors - IV. A wider range of progenitors”. In: *MNRAS* 512.2 (May 2022), pp. 2489–2507. DOI: [10.1093/mnras/stac613](https://doi.org/10.1093/mnras/stac613). arXiv: [2108.13864](https://arxiv.org/abs/2108.13864) [[astro-ph.HE](#)].
- [37] M. Bugli, J. Guilet, M. Obergaulinger, P. Cerdá-Durán, and M. A. Aloy. “The impact of non-dipolar magnetic fields in core-collapse supernovae”. In: *MNRAS* 492.1 (Feb. 2020), pp. 58–71. DOI: [10.1093/mnras/stz3483](https://doi.org/10.1093/mnras/stz3483). arXiv: [1909.02824](https://arxiv.org/abs/1909.02824) [[astro-ph.HE](#)].
- [38] Evan O’Connor and Christian D. Ott. “Black Hole Formation in Failing Core-Collapse Supernovae”. In: *ApJ* 730.2, 70 (Apr. 2011), p. 70. DOI: [10.1088/0004-637X/730/2/70](https://doi.org/10.1088/0004-637X/730/2/70). arXiv: [1010.5550](https://arxiv.org/abs/1010.5550) [[astro-ph.HE](#)].
- [39] L. Dessart, A. Burrows, E. Livne, and C. D. Ott. “The Proto-Neutron Star Phase of the Collapsar Model and the Route to Long-Soft Gamma-Ray Bursts and Hypernovae”. In: *ApJ* 673.1 (Jan. 2008), p. L43. DOI: [10.1086/527519](https://doi.org/10.1086/527519). arXiv: [0710.5789](https://arxiv.org/abs/0710.5789) [[astro-ph](#)].
- [40] M. Obergaulinger and M. Á. Aloy. “Protomagnetar and black hole formation in high-mass stars”. In: *MNRAS* 469.1 (July 2017), pp. L43–L47. DOI: [10.1093/mnrasl/slx046](https://doi.org/10.1093/mnrasl/slx046). arXiv: [1703.09893](https://arxiv.org/abs/1703.09893) [[astro-ph.SR](#)].
- [41] Goni Halevi, Swapnil Shankar, Philipp Mösta, Roland Haas, and Erik Schnetter. “A Black Hole Is Born: 3D General-relativistic Magnetohydrodynamic Simulation of Black Hole Formation from Core Collapse”. In: *ApJ* 991.2, L51 (Oct. 2025), p. L51. DOI: [10.3847/2041-8213/ae08a6](https://doi.org/10.3847/2041-8213/ae08a6). arXiv: [2506.20837](https://arxiv.org/abs/2506.20837) [[astro-ph.HE](#)].

- [42] J. Matsumoto, Y. Asahina, T. Takiwaki, K. Kotake, and H. R. Takahashi. “Magnetic support for neutrino-driven explosion of 3D non-rotating core-collapse supernova models”. In: *MNRAS* 516.2 (Oct. 2022), pp. 1752–1767. DOI: [10.1093/mnras/stac2335](https://doi.org/10.1093/mnras/stac2335). arXiv: [2202.07967](https://arxiv.org/abs/2202.07967) [[astro-ph.HE](#)].
- [43] Tianshu Wang and Adam Burrows. “Nucleosynthetic Analysis of Three-dimensional Core-collapse Supernova Simulations”. In: *ApJ* 962.1, 71 (Feb. 2024), p. 71. DOI: [10.3847/1538-4357/ad12b8](https://doi.org/10.3847/1538-4357/ad12b8). arXiv: [2311.03446](https://arxiv.org/abs/2311.03446) [[astro-ph.HE](#)].
- [44] Jin Matsumoto, Tomoya Takiwaki, and Kei Kotake. “Neutrino-driven massive stellar explosions in 3D fostered by magnetic fields via turbulent  $\alpha$ -effect”. In: *MNRAS* 528.1 (Feb. 2024), pp. L96–L101. DOI: [10.1093/mnrasl/slاد173](https://doi.org/10.1093/mnrasl/slاد173). arXiv: [2307.03400](https://arxiv.org/abs/2307.03400) [[astro-ph.HE](#)].
- [45] Kuo-Chuan Pan, Matthias Liebendörfer, Sean M. Couch, and Friedrich-Karl Thielemann. “Equation of State Dependent Dynamics and Multi-messenger Signals from Stellar-mass Black Hole Formation”. In: *ApJ* 857.1, 13 (Apr. 2018), p. 13. DOI: [10.3847/1538-4357/aab71d](https://doi.org/10.3847/1538-4357/aab71d). arXiv: [1710.01690](https://arxiv.org/abs/1710.01690) [[astro-ph.HE](#)].
- [46] Jade Powell, Bernhard Müller, and Alexander Heger. “The final core collapse of pulsational pair instability supernovae”. In: *MNRAS* 503.2 (May 2021), pp. 2108–2122. DOI: [10.1093/mnras/stab614](https://doi.org/10.1093/mnras/stab614). arXiv: [2101.06889](https://arxiv.org/abs/2101.06889) [[astro-ph.HE](#)].
- [47] Oliver Eggenberger Andersen, Evan O’Connor, Haakon Andresen, André da Silva Schneider, and Sean M. Couch. “Black Hole Supernovae, Their Equation of State Dependence, and Ejecta Composition”. In: *ApJ* 980.1, 53 (Feb. 2025), p. 53. DOI: [10.3847/1538-4357/ada899](https://doi.org/10.3847/1538-4357/ada899). arXiv: [2411.11969](https://arxiv.org/abs/2411.11969) [[astro-ph.HE](#)].
- [48] Yudai Suwa, Tomoya Takiwaki, Kei Kotake, Tobias Fischer, Matthias Liebendörfer, and Katsuhiko Sato. “On the Importance of the Equation of State for the Neutrino-driven Supernova Explosion Mechanism”. In: *ApJ* 764.1, 99 (Feb. 2013), p. 99. DOI: [10.1088/0004-637X/764/1/99](https://doi.org/10.1088/0004-637X/764/1/99). arXiv: [1206.6101](https://arxiv.org/abs/1206.6101) [[astro-ph.HE](#)].
- [49] Jade Powell and Bernhard Müller. “Impact of the nuclear equation of state on the explodability of massive stars”. In: *arXiv e-prints*, arXiv:2510.20076 (Oct. 2025), arXiv:2510.20076. DOI: [10.48550/arXiv.2510.20076](https://doi.org/10.48550/arXiv.2510.20076). arXiv: [2510.20076](https://arxiv.org/abs/2510.20076) [[astro-ph.HE](#)].
- [50] A. Marek, H.-T. Janka, and E. Müller. “Equation-of-state dependent features in shock-oscillation modulated neutrino and gravitational-wave signals from supernovae”. In: *A&A* 496.2 (Mar. 2009), pp. 475–494. DOI: [10.1051/0004-6361/200810883](https://doi.org/10.1051/0004-6361/200810883). arXiv: [0808.4136](https://arxiv.org/abs/0808.4136) [[astro-ph](#)].
- [51] Pia Jakobus, Bernhard Müller, Alexander Heger, Shuai Zha, Jade Powell, Anton Motornenko, Jan Steinheimer, and Horst Stöcker. “Gravitational Waves from a Core g Mode in Supernovae as Probes of the High-Density Equation of State”. In: *Phys. Rev. Lett.* 131.19, 191201 (Nov. 2023), p. 191201. DOI: [10.1103/PhysRevLett.131.191201](https://doi.org/10.1103/PhysRevLett.131.191201). arXiv: [2301.06515](https://arxiv.org/abs/2301.06515) [[astro-ph.HE](#)].
- [52] Jeremiah W. Murphy, Christian D. Ott, and Adam Burrows. “A Model for Gravitational Wave Emission from Neutrino-Driven Core-Collapse Supernovae”. In: *ApJ* 707.2 (Dec. 2009), pp. 1173–1190. DOI: [10.1088/0004-637X/707/2/1173](https://doi.org/10.1088/0004-637X/707/2/1173). arXiv: [0907.4762](https://arxiv.org/abs/0907.4762) [[astro-ph.SR](#)].
- [53] Konstantin N. Yakunin et al. “Gravitational waves from core collapse supernovae”. In: *Classical and Quantum Gravity* 27.19, 194005 (Oct. 2010), p. 194005. DOI: [10.1088/0264-9381/27/19/194005](https://doi.org/10.1088/0264-9381/27/19/194005). arXiv: [1005.0779](https://arxiv.org/abs/1005.0779) [[gr-qc](#)].
- [54] Bernhard Müller, Hans-Thomas Janka, and Andreas Marek. “A New Multi-dimensional General Relativistic Neutrino Hydrodynamics Code of Core-collapse Supernovae. III. Gravitational Wave Signals from Supernova Explosion Models”. In: *ApJ* 766.1, 43 (Mar. 2013), p. 43. DOI: [10.1088/0004-637X/766/1/43](https://doi.org/10.1088/0004-637X/766/1/43). arXiv: [1210.6984](https://arxiv.org/abs/1210.6984) [[astro-ph.SR](#)].
- [55] Konstantin N. Yakunin et al. “Gravitational wave signatures of ab initio two-dimensional core collapse supernova explosion models for 12 -25  $M_{\odot}$  stars”. In: *Phys. Rev. D* 92.8, 084040 (Oct. 2015), p. 084040. DOI: [10.1103/PhysRevD.92.084040](https://doi.org/10.1103/PhysRevD.92.084040). arXiv: [1505.05824](https://arxiv.org/abs/1505.05824) [[astro-ph.HE](#)].
- [56] Alejandro Torres-Forné, Pablo Cerdá-Durán, Andrea Passamonti, and José A. Font. “Towards asteroseismology of core-collapse supernovae with gravitational-wave observations - I. Cowling approximation”. In: *MNRAS* 474.4 (Mar. 2018), pp. 5272–5286. DOI: [10.1093/mnras/stx3067](https://doi.org/10.1093/mnras/stx3067). arXiv: [1708.01920](https://arxiv.org/abs/1708.01920) [[astro-ph.SR](#)].

- [57] Alejandro Torres-Forné, Pablo Cerdá-Durán, Andrea Passamonti, Martin Obergaulinger, and José A. Font. “Towards asteroseismology of core-collapse supernovae with gravitational wave observations - II. Inclusion of space-time perturbations”. In: *MNRAS* 482.3 (Jan. 2019), pp. 3967–3988. DOI: [10.1093/mnras/sty2854](https://doi.org/10.1093/mnras/sty2854). arXiv: [1806.11366](https://arxiv.org/abs/1806.11366) [[astro-ph.HE](#)].
- [58] M. Cusinato, M. Obergaulinger, and M. Á. Aloy. “Convection signatures in early-time gravitational waves from core-collapse supernovae”. In: *A&A* 705, A179 (Jan. 2026), A179. DOI: [10.1051/0004-6361/202556543](https://doi.org/10.1051/0004-6361/202556543). arXiv: [2507.16903](https://arxiv.org/abs/2507.16903) [[astro-ph.HE](#)].
- [59] John M. Blondin, Anthony Mezzacappa, and Christine DeMarino. “Stability of Standing Accretion Shocks, with an Eye toward Core-Collapse Supernovae”. In: *ApJ* 584.2 (Feb. 2003), pp. 971–980. DOI: [10.1086/345812](https://doi.org/10.1086/345812). arXiv: [astro-ph/0210634](https://arxiv.org/abs/astro-ph/0210634) [[astro-ph](#)].
- [60] John M. Blondin and Anthony Mezzacappa. “Pulsar spins from an instability in the accretion shock of supernovae”. In: *Nature* 445.7123 (Jan. 2007), pp. 58–60. DOI: [10.1038/nature05428](https://doi.org/10.1038/nature05428). arXiv: [astro-ph/0611680](https://arxiv.org/abs/astro-ph/0611680) [[astro-ph](#)].
- [61] Pablo Cerdá-Durán, Nicolas DeBrye, Miguel A. Aloy, José A. Font, and Martin Obergaulinger. “Gravitational Wave Signatures in Black Hole Forming Core Collapse”. In: *ApJ* 779.2, L18 (Dec. 2013), p. L18. DOI: [10.1088/2041-8205/779/2/L18](https://doi.org/10.1088/2041-8205/779/2/L18). arXiv: [1310.8290](https://arxiv.org/abs/1310.8290) [[astro-ph.SR](#)].
- [62] H. Andresen, B. Müller, E. Müller, and H. -Th. Janka. “Gravitational wave signals from 3D neutrino hydrodynamics simulations of core-collapse supernovae”. In: *MNRAS* 468.2 (June 2017), pp. 2032–2051. DOI: [10.1093/mnras/stx618](https://doi.org/10.1093/mnras/stx618). arXiv: [1607.05199](https://arxiv.org/abs/1607.05199) [[astro-ph.HE](#)].
- [63] Anthony Mezzacappa et al. “Gravitational-wave signal of a core-collapse supernova explosion of a 15  $M_{\odot}$  star”. In: *Phys. Rev. D* 102.2, 023027 (July 2020), p. 023027. DOI: [10.1103/PhysRevD.102.023027](https://doi.org/10.1103/PhysRevD.102.023027). arXiv: [2007.15099](https://arxiv.org/abs/2007.15099) [[astro-ph.HE](#)].
- [64] Anthony Mezzacappa et al. “Core collapse supernova gravitational wave emission for progenitors of 9.6, 15, and 25 $M_{\odot}$ ”. In: *Phys. Rev. D* 107.4, 043008 (Feb. 2023), p. 043008. DOI: [10.1103/PhysRevD.107.043008](https://doi.org/10.1103/PhysRevD.107.043008). arXiv: [2208.10643](https://arxiv.org/abs/2208.10643) [[astro-ph.SR](#)].
- [65] Marco Cusinato, Martin Obergaulinger, Miguel Á. Aloy, and José A. Font. “Resonant amplification of multimessenger emission in rotating stellar core collapse”. In: *Physical Review Research* 8.1, 013180 (Feb. 2026), p. 013180. DOI: [10.1103/6wp3-sw9y](https://doi.org/10.1103/6wp3-sw9y).
- [66] Masaru Shibata, Shigeyuki Karino, and Yoshiharu Eriguchi. “Dynamical instability of differentially rotating stars”. In: *MNRAS* 334.2 (Aug. 2002), pp. L27–L31. DOI: [10.1046/j.1365-8711.2002.05724.x](https://doi.org/10.1046/j.1365-8711.2002.05724.x). arXiv: [gr-qc/0206002](https://arxiv.org/abs/gr-qc/0206002) [[gr-qc](#)].
- [67] Masaru Shibata, Shigeyuki Karino, and Yoshiharu Eriguchi. “Dynamical bar-mode instability of differentially rotating stars: effects of equations of state and velocity profiles”. In: *MNRAS* 343.2 (Aug. 2003), pp. 619–626. DOI: [10.1046/j.1365-8711.2003.06699.x](https://doi.org/10.1046/j.1365-8711.2003.06699.x). arXiv: [astro-ph/0304298](https://arxiv.org/abs/astro-ph/0304298) [[astro-ph](#)].
- [68] A. L. Watts, N. Andersson, and D. I. Jones. “The Nature of Low T/—W— Dynamical Instabilities in Differentially Rotating Stars”. In: *ApJ* 618.1 (Jan. 2005), pp. L37–L40. DOI: [10.1086/427653](https://doi.org/10.1086/427653). arXiv: [astro-ph/0309554](https://arxiv.org/abs/astro-ph/0309554) [[astro-ph](#)].
- [69] Motoyuki Saijo and Shin’ichirou Yoshida. “Low T/—W— dynamical instabilities in differentially rotating stars: Diagnosis with canonical angular momentum”. In: *Albert Einstein Century International Conference*. Ed. by Jean-Michel Alimi and André Füzfa. Vol. 861. American Institute of Physics Conference Series. AIP, Nov. 2006, pp. 728–735. DOI: [10.1063/1.2399650](https://doi.org/10.1063/1.2399650). arXiv: [astro-ph/0604146](https://arxiv.org/abs/astro-ph/0604146) [[astro-ph](#)].
- [70] Shota Shibagaki, Takami Kuroda, Kei Kotake, and Tomoya Takiwaki. “A new gravitational-wave signature of low-T/—W— instability in rapidly rotating stellar core collapse”. In: *MNRAS* 493.1 (Mar. 2020), pp. L138–L142. DOI: [10.1093/mnras/1/slaa021](https://doi.org/10.1093/mnras/1/slaa021). arXiv: [1909.09730](https://arxiv.org/abs/1909.09730) [[astro-ph.HE](#)].
- [71] Tomoya Takiwaki, Kei Kotake, and Thierry Foglizzo. “Insights into non-axisymmetric instabilities in three-dimensional rotating supernova models with neutrino and gravitational-wave signatures”. In: *MNRAS* 508.1 (Nov. 2021), pp. 966–985. DOI: [10.1093/mnras/stab2607](https://doi.org/10.1093/mnras/stab2607). arXiv: [2107.02933](https://arxiv.org/abs/2107.02933) [[astro-ph.HE](#)].
- [72] M. Bugli, J. Guilet, T. Foglizzo, and M. Obergaulinger. “Three-dimensional core-collapse supernovae with complex magnetic structures - II. Rotational instabilities and multimessenger signatures”. In: *MNRAS* 520.4 (Apr. 2023), pp. 5622–5634. DOI: [10.1093/mnras/stad496](https://doi.org/10.1093/mnras/stad496). arXiv: [2210.05012](https://arxiv.org/abs/2210.05012) [[astro-ph.HE](#)].

- [73] Christian D. Ott, Shangli Ou, Joel E. Tohline, and Adam Burrows. “One-armed Spiral Instability in a Low-T/—W— Postbounce Supernova Core”. In: *ApJ* 625.2 (June 2005), pp. L119–L122. DOI: [10.1086/431305](https://doi.org/10.1086/431305). arXiv: [astro-ph/0503187](https://arxiv.org/abs/astro-ph/0503187) [[astro-ph](#)].
- [74] S. Scheidegger, T. Fischer, S. C. Whitehouse, and M. Liebendörfer. “Gravitational waves from 3D MHD core collapse simulations”. In: *A&A* 490.1 (Oct. 2008), pp. 231–241. DOI: [10.1051/0004-6361:20078577](https://doi.org/10.1051/0004-6361:20078577). arXiv: [0709.0168](https://arxiv.org/abs/0709.0168) [[astro-ph](#)].
- [75] S. Scheidegger, R. Käppeli, S. C. Whitehouse, T. Fischer, and M. Liebendörfer. “The influence of model parameters on the prediction of gravitational wave signals from stellar core collapse”. In: *A&A* 514, A51 (May 2010), A51. DOI: [10.1051/0004-6361/200913220](https://doi.org/10.1051/0004-6361/200913220). arXiv: [1001.1570](https://arxiv.org/abs/1001.1570) [[astro-ph.HE](#)].
- [76] M. Obergaulinger. “Astrophysical magnetohydrodynamics and radiative transfer: numerical methods and applications”. PhD thesis. Max-Planck-Institute for Astrophysics, Garching, Jan. 2008.
- [77] O. Just, M. Obergaulinger, and H. -T. Janka. “A new multidimensional, energy-dependent two-moment transport code for neutrino-hydrodynamics”. In: *MNRAS* 453.4 (Nov. 2015), pp. 3386–3413. DOI: [10.1093/mnras/stv1892](https://doi.org/10.1093/mnras/stv1892). arXiv: [1501.02999](https://arxiv.org/abs/1501.02999) [[astro-ph.HE](#)].
- [78] O. Just, R. Bollig, H. -Th Janka, M. Obergaulinger, R. Glas, and S. Nagataki. “Core-collapse supernova simulations in one and two dimensions: comparison of codes and approximations”. In: *MNRAS* 481.4 (Dec. 2018), pp. 4786–4814. DOI: [10.1093/mnras/sty2578](https://doi.org/10.1093/mnras/sty2578). arXiv: [1805.03953](https://arxiv.org/abs/1805.03953) [[astro-ph.HE](#)].
- [79] M. Obergaulinger, O. Just, and M. A. Aloy. “Core collapse with magnetic fields and rotation”. In: *Journal of Physics G Nuclear Physics* 45.8 (Aug. 2018), p. 084001. DOI: [10.1088/1361-6471/aac982](https://doi.org/10.1088/1361-6471/aac982). arXiv: [1806.00393](https://arxiv.org/abs/1806.00393) [[astro-ph.HE](#)].
- [80] Adam Griffiths, Miguel-Ángel Aloy, and Martin Obergaulinger. “The first 3D MHD core-collapse progenitors I: General properties, convection and nuclear burning”. In: *arXiv e-prints*, arXiv:2605.22927 (May 2026), arXiv:2605.22927. arXiv: [2605.22927](https://arxiv.org/abs/2605.22927) [[astro-ph.SR](#)].
- [81] J. Cernohorsky and S. A. Bludman. “Maximum Entropy Distribution and Closure for Bose-Einstein and Fermi-Dirac Radiation Transport”. In: *ApJ* 433 (Sept. 1994), p. 250. DOI: [10.1086/174640](https://doi.org/10.1086/174640).
- [82] Eirik Endeve, Christian Y. Cardall, and Anthony Mezzacappa. “Conservative Moment Equations for Neutrino Radiation Transport with Limited Relativity”. In: *arXiv e-prints*, arXiv:1212.4064 (Dec. 2012), arXiv:1212.4064. DOI: [10.48550/arXiv.1212.4064](https://doi.org/10.48550/arXiv.1212.4064). arXiv: [1212.4064](https://arxiv.org/abs/1212.4064) [[astro-ph.SR](#)].
- [83] M. Rampp and H. -T. Janka. “Radiation hydrodynamics with neutrinos. Variable Eddington factor method for core-collapse supernova simulations”. In: *A&A* 396 (Dec. 2002), pp. 361–392. DOI: [10.1051/0004-6361:20021398](https://doi.org/10.1051/0004-6361:20021398). arXiv: [astro-ph/0203101](https://arxiv.org/abs/astro-ph/0203101) [[astro-ph](#)].
- [84] S. E. Woosley and A. Heger. “The Progenitor Stars of Gamma-Ray Bursts”. In: *ApJ* 637.2 (Feb. 2006), pp. 914–921. DOI: [10.1086/498500](https://doi.org/10.1086/498500). arXiv: [astro-ph/0508175](https://arxiv.org/abs/astro-ph/0508175) [[astro-ph](#)].
- [85] M. Á. Aloy and M. Obergaulinger. “Magnetorotational core collapse of possible GRB progenitors - II. Formation of protomagnetars and collapsars”. In: *MNRAS* 500.4 (Jan. 2021), pp. 4365–4397. DOI: [10.1093/mnras/staa3273](https://doi.org/10.1093/mnras/staa3273). arXiv: [2008.03779](https://arxiv.org/abs/2008.03779) [[astro-ph.HE](#)].
- [86] Adam Griffiths, Miguel-Ángel Aloy, and Martin Obergaulinger. “The first 3D MHD core-collapse progenitors II: Rotation, magnetic-field amplification, and magnetic topology”. In: *arXiv e-prints*, arXiv:2605.22938 (May 2026), arXiv:2605.22938. arXiv: [2605.22938](https://arxiv.org/abs/2605.22938) [[astro-ph.SR](#)].
- [87] Y. Suwa, T. Takiwaki, K. Kotake, and K. Sato. “Magnetorotational Collapse of Population III Stars”. In: *PASJ* 59 (Aug. 2007), pp. 771–785. DOI: [10.1093/pasj/59.4.771](https://doi.org/10.1093/pasj/59.4.771). arXiv: [0704.1945](https://arxiv.org/abs/0704.1945) [[astro-ph](#)].
- [88] M. Obergaulinger and M. Á. Aloy. “Magnetorotational core collapse of possible GRB progenitors - III. Three-dimensional models”. In: *MNRAS* 503.4 (May 2021), pp. 4942–4963. DOI: [10.1093/mnras/stab295](https://doi.org/10.1093/mnras/stab295). arXiv: [2008.07205](https://arxiv.org/abs/2008.07205) [[astro-ph.HE](#)].
- [89] S. Typel, M. Oertel, and T. Klähn. “CompOSE CompStar online supernova equations of state harmonising the concert of nuclear physics and astrophysics compose.obspm.fr”. In: *Physics of Particles and Nuclei* 46.4 (July 2015), pp. 633–664. DOI: [10.1134/S1063779615040061](https://doi.org/10.1134/S1063779615040061).

- [90] M. Oertel, M. Hempel, T. Klöhn, and S. Typel. “Equations of state for supernovae and compact stars”. In: *Reviews of Modern Physics* 89.1, 015007 (Jan. 2017), p. 015007. DOI: [10.1103/RevModPhys.89.015007](https://doi.org/10.1103/RevModPhys.89.015007). arXiv: [1610.03361](https://arxiv.org/abs/1610.03361) [[astro-ph.HE](#)].
- [91] M. C. Miller et al. “PSR J0030+0451 Mass and Radius from NICER Data and Implications for the Properties of Neutron Star Matter”. In: *ApJ* 887.1, L24 (Dec. 2019), p. L24. DOI: [10.3847/2041-8213/ab50c5](https://doi.org/10.3847/2041-8213/ab50c5). arXiv: [1912.05705](https://arxiv.org/abs/1912.05705) [[astro-ph.HE](#)].
- [92] T. E. Riley et al. “A NICER View of PSR J0030+0451: Millisecond Pulsar Parameter Estimation”. In: *ApJ* 887.1, L21 (Dec. 2019), p. L21. DOI: [10.3847/2041-8213/ab481c](https://doi.org/10.3847/2041-8213/ab481c). arXiv: [1912.05702](https://arxiv.org/abs/1912.05702) [[astro-ph.HE](#)].
- [93] M. C. Miller et al. “The Radius of PSR J0740+6620 from NICER and XMM-Newton Data”. In: *ApJ* 918.2, L28 (Sept. 2021), p. L28. DOI: [10.3847/2041-8213/ac089b](https://doi.org/10.3847/2041-8213/ac089b). arXiv: [2105.06979](https://arxiv.org/abs/2105.06979) [[astro-ph.HE](#)].
- [94] Thomas E. Riley et al. “A NICER View of the Massive Pulsar PSR J0740+6620 Informed by Radio Timing and XMM-Newton Spectroscopy”. In: *ApJ* 918.2, L27 (Sept. 2021), p. L27. DOI: [10.3847/2041-8213/ac0a81](https://doi.org/10.3847/2041-8213/ac0a81). arXiv: [2105.06980](https://arxiv.org/abs/2105.06980) [[astro-ph.HE](#)].
- [95] B. P. Abbott et al. “GW170817: Measurements of Neutron Star Radii and Equation of State”. In: *Phys. Rev. Lett.* 121.16, 161101 (Oct. 2018), p. 161101. DOI: [10.1103/PhysRevLett.121.161101](https://doi.org/10.1103/PhysRevLett.121.161101). arXiv: [1805.11581](https://arxiv.org/abs/1805.11581) [[gr-qc](#)].
- [96] Andrew W. Steiner, James M. Lattimer, and Edward F. Brown. “The Equation of State from Observed Masses and Radii of Neutron Stars”. In: *ApJ* 722.1 (Oct. 2010), pp. 33–54. DOI: [10.1088/0004-637X/722/1/33](https://doi.org/10.1088/0004-637X/722/1/33). arXiv: [1005.0811](https://arxiv.org/abs/1005.0811) [[astro-ph.HE](#)].
- [97] P. B. Demorest, T. Pennucci, S. M. Ransom, M. S. E. Roberts, and J. W. T. Hessels. “A two-solar-mass neutron star measured using Shapiro delay”. In: *Nature* 467.7319 (Oct. 2010), pp. 1081–1083. DOI: [10.1038/nature09466](https://doi.org/10.1038/nature09466). arXiv: [1010.5788](https://arxiv.org/abs/1010.5788) [[astro-ph.HE](#)].
- [98] John Antoniadis et al. “A Massive Pulsar in a Compact Relativistic Binary”. In: *Science* 340.6131 (Apr. 2013), p. 448. DOI: [10.1126/science.1233232](https://doi.org/10.1126/science.1233232). arXiv: [1304.6875](https://arxiv.org/abs/1304.6875) [[astro-ph.HE](#)].
- [99] James M. Lattimer and Douglas F. Swesty. “A generalized equation of state for hot, dense matter”. In: *Nucl. Phys. A* 535.2 (Dec. 1991), pp. 331–376. DOI: [10.1016/0375-9474\(91\)90452-C](https://doi.org/10.1016/0375-9474(91)90452-C).
- [100] A. S. Schneider, L. F. Roberts, and C. D. Ott. “Open-source nuclear equation of state framework based on the liquid-drop model with Skyrme interaction”. In: *Phys. Rev. C* 96.6, 065802 (Dec. 2017), p. 065802. DOI: [10.1103/PhysRevC.96.065802](https://doi.org/10.1103/PhysRevC.96.065802).
- [101] Sarmistha Banik, Matthias Hempel, and Debades Bandyopadhyay. “New Hyperon Equations of State for Supernovae and Neutron Stars in Density-dependent Hadron Field Theory”. In: *ApJS* 214.2, 22 (Oct. 2014), p. 22. DOI: [10.1088/0067-0049/214/2/22](https://doi.org/10.1088/0067-0049/214/2/22). arXiv: [1404.6173](https://arxiv.org/abs/1404.6173) [[astro-ph.HE](#)].
- [102] Adriana R. Raduta and Mikhail V. Beznogov. “New ab initio constrained extended Skyrme equations of state for simulations of neutron stars, supernovae, and binary mergers: I. Sub-saturation density domain”. In: *A&A* 701, A143 (Sept. 2025), A143. DOI: [10.1051/0004-6361/202555351](https://doi.org/10.1051/0004-6361/202555351). arXiv: [2504.21725](https://arxiv.org/abs/2504.21725) [[nucl-th](#)].
- [103] Stefanos Tsiopelas, Armen Sedrakian, and Micaela Oertel. “Finite-temperature equations of state of compact stars with hyperons: three-dimensional tables”. In: *European Physical Journal A* 60.6, 127 (June 2024), p. 127. DOI: [10.1140/epja/s10050-024-01351-1](https://doi.org/10.1140/epja/s10050-024-01351-1). arXiv: [2406.00484](https://arxiv.org/abs/2406.00484) [[nucl-th](#)].
- [104] B. P. Abbott et al. “GW170817: Observation of Gravitational Waves from a Binary Neutron Star Inspiral”. In: *Phys. Rev. Lett.* 119.16, 161101 (Oct. 2017), p. 161101. DOI: [10.1103/PhysRevLett.119.161101](https://doi.org/10.1103/PhysRevLett.119.161101). arXiv: [1710.05832](https://arxiv.org/abs/1710.05832) [[gr-qc](#)].
- [105] B. P. Abbott et al. “GW190425: Observation of a Compact Binary Coalescence with Total Mass  $\sim 3.4 M_{\odot}$ ”. In: *ApJ* 892.1, L3 (Mar. 2020), p. L3. DOI: [10.3847/2041-8213/ab75f5](https://doi.org/10.3847/2041-8213/ab75f5). arXiv: [2001.01761](https://arxiv.org/abs/2001.01761) [[astro-ph.HE](#)].
- [106] Ingo Tews, James M. Lattimer, Akira Ohnishi, and Evgeni E. Kolomeitsev. “Symmetry Parameter Constraints from a Lower Bound on Neutron-matter Energy”. In: *ApJ* 848.2, 105 (Oct. 2017), p. 105. DOI: [10.3847/1538-4357/aa8db9](https://doi.org/10.3847/1538-4357/aa8db9). arXiv: [1611.07133](https://arxiv.org/abs/1611.07133) [[nucl-th](#)].

- [107] E. Chabanat, P. Bonche, P. Haensel, J. Meyer, and R. Schaeffer. “A Skyrme parametrization from subnuclear to neutron star densities Part II. Nuclei far from stabilities”. In: *Nucl. Phys. A* 635.1-2 (May 1998), pp. 231–256. DOI: [10.1016/S0375-9474\(98\)00180-8](https://doi.org/10.1016/S0375-9474(98)00180-8).
- [108] M. Dutra, O. Lourenço, J. S. Sá Martins, A. Delfino, J. R. Stone, and P. D. Stevenson. “Skyrme interaction and nuclear matter constraints”. In: *Phys. Rev. C* 85.3, 035201 (Mar. 2012), p. 035201. DOI: [10.1103/PhysRevC.85.035201](https://doi.org/10.1103/PhysRevC.85.035201). arXiv: [1202.3902](https://arxiv.org/abs/1202.3902) [[nucl-th](#)].
- [109] Adriana R. Raduta and Mikhail V. Beznogov. “New ab initio constrained extended Skyrme equations of state for simulations of neutron stars, supernovae, and binary mergers: I. Sub-saturation density domain”. In: *A&A* 701, A143 (Sept. 2025), A143. DOI: [10.1051/0004-6361/202555351](https://doi.org/10.1051/0004-6361/202555351). arXiv: [2504.21725](https://arxiv.org/abs/2504.21725) [[nucl-th](#)].
- [110] F. Douchin and P. Haensel. “A unified equation of state of dense matter and neutron star structure”. In: *A&A* 380 (Dec. 2001), pp. 151–167. DOI: [10.1051/0004-6361:20011402](https://doi.org/10.1051/0004-6361:20011402). arXiv: [astro-ph/0111092](https://arxiv.org/abs/astro-ph/0111092) [[astro-ph](#)].
- [111] James M. Lattimer and Douglas F. Swesty. “A generalized equation of state for hot, dense matter”. In: *Nucl. Phys. A* 535.2 (Dec. 1991), pp. 331–376. DOI: [10.1016/0375-9474\(91\)90452-C](https://doi.org/10.1016/0375-9474(91)90452-C).
- [112] Sarmistha Banik, Matthias Hempel, and Debades Bandyopadhyay. “New Hyperon Equations of State for Supernovae and Neutron Stars in Density-dependent Hadron Field Theory”. In: *ApJS* 214.2, 22 (Oct. 2014), p. 22. DOI: [10.1088/0067-0049/214/2/22](https://doi.org/10.1088/0067-0049/214/2/22). arXiv: [1404.6173](https://arxiv.org/abs/1404.6173) [[astro-ph.HE](#)].
- [113] Tanja Hinderer, Benjamin D. Lackey, Ryan N. Lang, and Jocelyn S. Read. “Tidal deformability of neutron stars with realistic equations of state and their gravitational wave signatures in binary inspiral”. In: *Phys. Rev. D* 81.12, 123016 (June 2010), p. 123016. DOI: [10.1103/PhysRevD.81.123016](https://doi.org/10.1103/PhysRevD.81.123016). arXiv: [0911.3535](https://arxiv.org/abs/0911.3535) [[astro-ph.HE](#)].
- [114] Charles W. Misner, Kip S. Thorne, and John Archibald Wheeler. *Gravitation*. 1973.
- [115] Kip S. Thorne. “Multipole expansions of gravitational radiation”. In: *Reviews of Modern Physics* 52.2 (Apr. 1980), pp. 299–340. DOI: [10.1103/RevModPhys.52.299](https://doi.org/10.1103/RevModPhys.52.299).
- [116] Shuai Zha. “Proper way to spatially decompose the gravitational-wave origin in stellar collapse simulations”. In: *Phys. Rev. D* 110.8, 083034 (Oct. 2024), p. 083034. DOI: [10.1103/PhysRevD.110.083034](https://doi.org/10.1103/PhysRevD.110.083034). arXiv: [2405.09729](https://arxiv.org/abs/2405.09729) [[astro-ph.HE](#)].
- [117] Raphaël Raynaud, Pablo Cerdá-Durán, and Jérôme Guilet. “Gravitational wave signature of proto-neutron star convection: I. MHD numerical simulations”. In: *MNRAS* 509.3 (Jan. 2022), pp. 3410–3426. DOI: [10.1093/mnras/stab3109](https://doi.org/10.1093/mnras/stab3109). arXiv: [2103.12445](https://arxiv.org/abs/2103.12445) [[astro-ph.SR](#)].
- [118] N. E. Huang, Z. Shen, S. R. Long, M. C. Wu, H. H. Shih, Q. Zheng, N. -C. Yen, C. C. Tung, and H. H. Liu. “The empirical mode decomposition and the Hilbert spectrum for nonlinear and non-stationary time series analysis”. In: *Proceedings of the Royal Society of London Series A* 454.1971 (Mar. 1998), pp. 903–998. DOI: [10.1098/rspa.1998.0193](https://doi.org/10.1098/rspa.1998.0193).
- [119] Norden E. Huang, Zheng Shen, and Steven R. Long. “A NEW VIEW OF NONLINEAR WATER WAVES: The Hilbert Spectrum1”. In: *Annual Review of Fluid Mechanics* 31 (Jan. 1999), pp. 417–457. DOI: [10.1146/annurev.fluid.31.1.417](https://doi.org/10.1146/annurev.fluid.31.1.417).
- [120] Man-Li C. Wu, Siegfried D. Schubert, Max J. Suarez, and Norden E. Huang. “An Analysis of Moisture Fluxes into the Gulf of California”. In: *Journal of Climate* 22.8 (Jan. 2009), p. 2216. DOI: [10.1175/2008JCLI2525.1](https://doi.org/10.1175/2008JCLI2525.1).
- [121] Dawid Laszuk. *Python implementation of Empirical Mode Decomposition algorithm*. <https://github.com/laszukdawid/PyEMD>. 2017. DOI: [10.5281/zenodo.5459184](https://doi.org/10.5281/zenodo.5459184).
- [122] Hiroshi Akima. “A New Method of Interpolation and Smooth Curve Fitting Based on Local Procedures”. In: *J. ACM* 17 (1970), pp. 589–602. URL: <https://api.semanticscholar.org/CorpusID:33862277>.
- [123] A. Passamonti and N. Andersson. “The intimate relation between the low T/W instability and the corotation point”. In: *MNRAS* 446.1 (Jan. 2015), pp. 555–565. DOI: [10.1093/mnras/stu2062](https://doi.org/10.1093/mnras/stu2062). arXiv: [1409.0677](https://arxiv.org/abs/1409.0677) [[astro-ph.SR](#)].
- [124] Shota Shibagaki, Takami Kuroda, Kei Kotake, and Tomoya Takiwaki. “Characteristic time variability of gravitational-wave and neutrino signals from three-dimensional simulations of non-rotating and rapidly rotating stellar core collapse”. In: *MNRAS* 502.2 (Apr. 2021), pp. 3066–3084. DOI: [10.1093/mnras/stab228](https://doi.org/10.1093/mnras/stab228). arXiv: [2010.03882](https://arxiv.org/abs/2010.03882) [[astro-ph.HE](#)].

- [125] T. Rembiasz, M. Obergaulinger, P. Cerdá-Durán, E. Müller, and M. A. Aloy. “Termination of the magnetorotational instability via parasitic instabilities in core-collapse supernovae”. In: *MNRAS* 456.4 (Mar. 2016), pp. 3782–3802. DOI: [10.1093/mnras/stv2917](https://doi.org/10.1093/mnras/stv2917). arXiv: [1508.04799](https://arxiv.org/abs/1508.04799) [[astro-ph.SR](#)].
- [126] A. Passamonti and N. Andersson. “Merger-inspired rotation laws and the low-T/W instability in neutron stars”. In: *MNRAS* 498.4 (Nov. 2020), pp. 5904–5915. DOI: [10.1093/mnras/staa2725](https://doi.org/10.1093/mnras/staa2725). arXiv: [2003.10198](https://arxiv.org/abs/2003.10198) [[astro-ph.SR](#)].
- [127] Sofia Suvorova, Jade Powell, and Andrew Melatos. “Reconstructing gravitational wave core-collapse supernova signals with dynamic time warping”. In: *Phys. Rev. D* 99.12, 123012 (June 2019), p. 123012. DOI: [10.1103/PhysRevD.99.123012](https://doi.org/10.1103/PhysRevD.99.123012). arXiv: [1901.02535](https://arxiv.org/abs/1901.02535) [[astro-ph.IM](#)].
- [128] M. Kachelrieß, R. Tomàs, R. Buras, H.-Th. Janka, A. Marek, and M. Rampp. “Exploiting the neutronization burst of a galactic supernova”. In: *Phys. Rev. D* 71.6, 063003 (Mar. 2005), p. 063003. DOI: [10.1103/PhysRevD.71.063003](https://doi.org/10.1103/PhysRevD.71.063003). arXiv: [astro-ph/0412082](https://arxiv.org/abs/astro-ph/0412082) [[astro-ph](#)].
- [129] L. Hüdepohl, B. Müller, H.-T. Janka, A. Marek, and G. G. Raffelt. “Neutrino Signal of Electron-Capture Supernovae from Core Collapse to Cooling”. In: *Phys. Rev. Lett.* 104.25, 251101 (June 2010), p. 251101. DOI: [10.1103/PhysRevLett.104.251101](https://doi.org/10.1103/PhysRevLett.104.251101). arXiv: [0912.0260](https://arxiv.org/abs/0912.0260) [[astro-ph.SR](#)].
- [130] C. J. Moore, R. H. Cole, and C. P. L. Berry. “Gravitational-wave sensitivity curves”. In: *Classical and Quantum Gravity* 32.1, 015014 (Jan. 2015), p. 015014. DOI: [10.1088/0264-9381/32/1/015014](https://doi.org/10.1088/0264-9381/32/1/015014). arXiv: [1408.0740](https://arxiv.org/abs/1408.0740) [[gr-qc](#)].
- [131] B. P. Abbott et al. “Prospects for observing and localizing gravitational-wave transients with Advanced LIGO, Advanced Virgo and KAGRA”. In: *Living Reviews in Relativity* 23.1, 3 (Sept. 2020), p. 3. DOI: [10.1007/s41114-020-00026-9](https://doi.org/10.1007/s41114-020-00026-9).
- [132] LIGO Scientific Collaboration KAGRA Collaboration and VIRGO Collaboration. *Noise curves used for Simulations in the update of the Observing Scenarios Paper*. <https://dcc.ligo.org/LIGO-T2000012/public>. Online; accessed January 2025. 2022.
- [133] ET design team. *ET-D sensitivity curve*. <https://apps.et-gw.eu/tds/?content=3&r=14065>. Online; accessed December 2025. 2018.
- [134] Kuns, Kevin and Fulda, Paul and Barsotti, Lisa and Evans, Matthew. *Cosmic Explorer Document T2000017-v8*. <https://dcc.cosmicexplorer.org/CE-T2000017/public>. Online; accessed December 2025. 2023.
- [135] I. D. Karachentsev and O. G. Kashibadze. “Masses of the local group and of the M81 group estimated from distortions in the local velocity field”. In: *Astrophysics* 49.1 (Jan. 2006), pp. 3–18. DOI: [10.1007/s10511-006-0002-6](https://doi.org/10.1007/s10511-006-0002-6).
- [136] Jade Powell, Bernhard Müller, David R. Aguilera-Dena, and Norbert Langer. “Three dimensional magnetorotational core-collapse supernova explosions of a 39 solar mass progenitor star”. In: *MNRAS* 522.4 (July 2023), pp. 6070–6086. DOI: [10.1093/mnras/stad1292](https://doi.org/10.1093/mnras/stad1292). arXiv: [2212.00200](https://arxiv.org/abs/2212.00200) [[astro-ph.HE](#)].
- [137] C. Kraus and the SNO+ Collaboration. “SNO with liquid scintillator: SNO+”. In: *Progress in Particle and Nuclear Physics* 57.1 (July 2006), pp. 150–152. DOI: [10.1016/j.pnpnp.2005.12.001](https://doi.org/10.1016/j.pnpnp.2005.12.001).
- [138] Amol S. Dighe and Alexei Yu. Smirnov. “Identifying the neutrino mass spectrum from a supernova neutrino burst”. In: *Phys. Rev. D* 62.3, 033007 (Aug. 2000), p. 033007. DOI: [10.1103/PhysRevD.62.033007](https://doi.org/10.1103/PhysRevD.62.033007). arXiv: [hep-ph/9907423](https://arxiv.org/abs/hep-ph/9907423) [[hep-ph](#)].
- [139] Francesco Capozzi, Eleonora Di Valentino, Eligio Lisi, Antonio Marrone, Alessandro Melchiorri, and Antonio Palazzo. “Global constraints on absolute neutrino masses and their ordering”. In: *Phys. Rev. D* 95.9, 096014 (May 2017), p. 096014. DOI: [10.1103/PhysRevD.95.096014](https://doi.org/10.1103/PhysRevD.95.096014). arXiv: [1703.04471](https://arxiv.org/abs/1703.04471) [[hep-ph](#)].
- [140] Amanda L. Baxter et al. “SNEWPY: A Data Pipeline from Supernova Simulations to Neutrino Signals”. In: *ApJ* 925.2, 107 (Feb. 2022), p. 107. DOI: [10.3847/1538-4357/ac350f](https://doi.org/10.3847/1538-4357/ac350f).
- [141] Kate Scholberg, Joshua B. Albert, and Justin Vasel. *SNOwGLOBES: SuperNova Observatories with GLOBES*. Astrophysics Source Code Library, record ascl:2109.019. Sept. 2021. ascl: [2109.019](https://arxiv.org/abs/2109.019).
- [142] Lyla Choi, Adam Burrows, and David Vartanyan. “Predicted neutrino signal features of core-collapse supernovae”. In: *Phys. Rev. D* 111.12, 123038 (June 2025), p. 123038. DOI: [10.1103/ls9r-1861](https://doi.org/10.1103/ls9r-1861). arXiv: [2503.07531](https://arxiv.org/abs/2503.07531) [[astro-ph.HE](#)].

- [143] P. Vogel and J. F. Beacom. “Angular distribution of neutron inverse beta decay,  $\nu^-_e + p \rightarrow e^+ + n$ ”. In: *Phys. Rev. D* 60.5, 053003 (Sept. 1999), p. 053003. DOI: [10.1103/PhysRevD.60.053003](https://doi.org/10.1103/PhysRevD.60.053003). arXiv: [hep-ph/9903554](https://arxiv.org/abs/hep-ph/9903554) [[hep-ph](#)].
- [144] Alessandro Strumia and Francesco Vissani. “Precise quasielastic neutrino/nucleon cross-section”. In: *Physics Letters B* 564.1-2 (July 2003), pp. 42–54. DOI: [10.1016/S0370-2693\(03\)00616-6](https://doi.org/10.1016/S0370-2693(03)00616-6). arXiv: [astro-ph/0302055](https://arxiv.org/abs/astro-ph/0302055) [[astro-ph](#)].
- [145] Tina Lund, Annap Wongwathanarat, Hans-Thomas Janka, Ewald Müller, and Georg Raffelt. “Fast time variations of supernova neutrino signals from 3-dimensional models”. In: *Phys. Rev. D* 86.10, 105031 (Nov. 2012), p. 105031. DOI: [10.1103/PhysRevD.86.105031](https://doi.org/10.1103/PhysRevD.86.105031). arXiv: [1208.0043](https://arxiv.org/abs/1208.0043) [[astro-ph.HE](#)].
- [146] Hiroki Nagakura, Adam Burrows, David Radice, and David Vartanyan. “Towards an understanding of the resolution dependence of Core-Collapse Supernova simulations”. In: *MNRAS* 490.4 (Dec. 2019), pp. 4622–4637. DOI: [10.1093/mnras/stz2730](https://doi.org/10.1093/mnras/stz2730). arXiv: [1905.03786](https://arxiv.org/abs/1905.03786) [[astro-ph.HE](#)].
- [147] Tobias Melson, Daniel Kresse, and Hans-Thomas Janka. “Resolution Study for Three-dimensional Supernova Simulations with the Prometheus-Vertex Code”. In: *ApJ* 891.1, 27 (Mar. 2020), p. 27. DOI: [10.3847/1538-4357/ab72a7](https://doi.org/10.3847/1538-4357/ab72a7). arXiv: [1904.01699](https://arxiv.org/abs/1904.01699) [[astro-ph.HE](#)].
- [148] Vishnu Varma and Bernhard Müller. “Resolution dependence in magnetohydrodynamic simulations of neutrino-driven core-collapse supernovae”. In: *MNRAS* 548.2, stag626 (May 2026), stag626. DOI: [10.1093/mnras/stag626](https://doi.org/10.1093/mnras/stag626). arXiv: [2601.18357](https://arxiv.org/abs/2601.18357) [[astro-ph.HE](#)].